Modeling and optimization of the thermomechanical behavior of metal partsobtained by sintering : Numerical and experimental approach.

Judice Cumbunga

UBFC
UNIVERSITÉ
BOURGOGNE FRANCHE-COMTÉ

utbm
université de technologie
Belfort-Montbéliard

THÈSE DE DOCTORAT DE L'ÉTABLISSEMENT UNIVERSITÉ BOURGOGNE FRANCHE-COMTÉ

PRÉPARÉE À L'UNIVERSITÉ DE TECHNOLOGIE DE BELFORT-MONTBÉLIARD

École doctorale n°37

Sciences Pour l'Ingénieur et Microtechniques

Doctorat de Mécanique

par

Judice Cumbunga

Modeling and optimization of the thermomechanical behavior of metal parts obtained by sintering: Numerical and experimental approach.

Thèse présentée et soutenue à Belfort, le 27 Mars 2024

Composition du Jury :

LANZETTA François	Professeur des universités, Université de Franche-Comté	President
BERGHEAU Jean Michel	Professeur des universités, Université de Lyon	Rapporteur
BAUZIN Jean Gabriel	Maître de conférences HDR, Université Paris Nanterre	Rapporteur
SEBASTIÃO Jone Heitor	Associate Professor, Agostinho Neto University, Angola	Examinateur
BISWAS Sudipta	Maîtresse de recherche, Idaho National Laboratory, USA	Examinatrice
ABBOUDI Said	Professeur des universités, Université de Technologie de Belfort Montbéliard	Directeur
GOMES Samuel	Professeur des universités, Université de Technologie de Belfort Montbéliard	Co-Directeur
CHAMORET Dominique	Maîtresse de conférences HDR, Université de Technologie de Belfort Montbéliard	Co-Encadrante
CALISTE Jean-Pierre	Enseignant-Chercheur Emérite, Université de Technologie de Compiègne	Invité
AUBERT Jean-Michel	Ingénieur TotalEnergies, SA	Invité

N° | X | X | X |

SPIM
école doctorale **sciences pour l'ingénieur et microtechniques**

Title: Modeling and optimization of the thermomechanical behavior of metal parts obtained by sintering: Numerical and experimental approach.

Keywords: Solid-state sintering, metal extrusion additive manufacturing, microstructural evolution, multiphysics coupling, finite element method, stain steel 316L, Taguchi method.

Abstract:

The pressureless solid-state sintering process is a heat treatment applied to improve or adjust the material's properties according to its application, considering its ability to process parts with complex geometry (shape), high dimensional accuracy, small sizes, and suitability for soft and hard materials. However, modeling heat treatments is a challenging task, as an appropriate model must consider several aspects: such as multiscale and multi-physical issues, strong nonlinearity of the material, complex geometry, boundary conditions, etc. In the industry, proper processing parameters are mainly obtained by trial and error. To overcome these limitations, computer simulation is emerging, as it can save costs and provide more valuable references or guidance for actual production compared to actual sintering tests. Various research projects have been developed around computational models, and the approaches are at different levels or scales, such as small-scale (atomic level), mesoscale (particles, grains, and pores level), and continuum scale (component level). The maturity and ability to predict the evolution of microstructure has put the mesoscopic model (particles, grains, and pores level) ahead of the others. So, considering the main research question "Given a green part obtained by MExAM, how to simulate computationally the microstructure evolution (starting from its initial microstructural arrangement) to control the changes in thermomechanical properties during the solid-state sintering process?" Thus, a robust computational model based on a multiphysics approach to predict the evolution of microstructure and thermomechanical properties of the material has been developed, tested, and validated. The numerical techniques based on FEM used to solve this multi-physics (coupling of heat conduction equation, mechanical field, and phase-field equations) and non-linear problem have been explained. The simulation findings suggest that the developed model is capable of accurately forecasting the behavior of the sintering process concerning its microstructural, thermal, and mechanical properties. The strategy to apply the model to simulate and predict the material's behavior for MExAM was presented, as well as how to use the model to optimize the thermomechanical properties of the processed material. Optimization was achieved by coupling the simulation results with the Taguchi method. It should be noted that the results obtained from the material properties analysis reflect the successful application of the model, both, from the perspective of predicting the microstructural and thermomechanical behavior of the material under certain sintering conditions and from, the perspective of optimization.

Titre : Modeling and optimization of the thermomechanical behavior of metal parts obtained by sintering: Numerical and experimental approach.

Mots-clés : Frittage à l'état solide, fabrication additive par extrusion de métal, évolution microstructurale, couplage multiphysique, méthode des éléments finis, acier inoxydable 316L, Méthode Taguchi.

Résumé :

Le processus de frittage à l'état solide sans pression est un traitement thermique appliqué pour améliorer ou ajuster les propriétés du matériau en fonction de son application. Le processus de frittage à l'état solide sans pression est un traitement thermique appliqué pour améliorer ou ajuster les propriétés du matériau en fonction de son application, compte tenu de sa capacité à traiter des pièces de géométrie complexe (forme), de sa grande précision dimensionnelle, de ses petites dimensions et de son aptitude à traiter des matériaux tendres et durs. Cependant, la modélisation des traitements thermiques est une tâche difficile, car un modèle approprié doit prendre en compte plusieurs aspects, tels que les questions multiéchelles et multiphysiques, la forte non-linéarité du matériau, la géométrie complexe, les conditions aux limites, etc. Dans l'industrie, les paramètres de traitement appropriés sont principalement obtenus par essais et erreurs. Dans l'industrie, les paramètres de traitement appropriés sont principalement obtenus par essais et erreurs. Pour surmonter ces limitations, la simulation informatique fait son apparition, car elle permet d'économiser des coûts et fournit des références ou des conseils plus précieux pour la production réelle que les essais de frittage réels. Divers projets de recherche ont été développés autour de modèles informatiques, et les approches se situent à différents niveaux ou échelles, tels que la petite échelle (niveau atomique), la méso-échelle (niveau des particules, des grains et des pores), et l'échelle du continuum (niveau des composants). La maturité et la capacité à prédire l'évolution de la microstructure ont placé le modèle mésoscopique (au niveau des particules, des grains et des pores) devant les autres. Ainsi, compte tenu de la question principale de la recherche "Étant donné une pièce verte obtenue par MExAM, comment simuler informatiquement l'évolution de la microstructure (à partir de son arrangement microstructural initial) pour contrôler les changements dans les propriétés thermomécaniques pendant le processus de frittage à l'état solide ?" Ainsi, un modèle de calcul robuste basé sur une approche multiphysique pour prédire l'évolution de la microstructure et des propriétés thermomécaniques du matériau a été développé, testé et validé. Les techniques numériques basées sur les éléments finis utilisées pour résoudre ce problème multiphysique et non linéaire ont été expliquées. Les résultats de la simulation suggèrent que le modèle développé est capable de prévoir avec précision le comportement du processus de frittage en ce qui concerne ses propriétés microstructurales, thermiques et mécaniques. La stratégie d'application du modèle pour simuler et prévoir le comportement du matériau pour le MExAM a été présentée, ainsi que la manière d'utiliser le modèle pour optimiser les propriétés thermomécaniques du matériau traité. L'optimisation a été réalisée en couplant les résultats de la simulation avec la méthode Taguchi. Il convient de noter que les résultats obtenus à partir de l'analyse des propriétés des matériaux reflètent l'application réussie du modèle, tant du point de vue de la prévision du comportement microstructural et thermomécanique du matériau dans certaines conditions de frittage que du point de vue de l'optimisation.

UBFC UNIVERSITÉ BOURGOGNE FRANCHE-COMTÉ
Université Bourgogne Franche-Comté
32, avenue de l'Observatoire
25000 Besançon, France

Acknowledgements

I believe that the difficult paths that lead us to life-changing experiences are not made alone. Undoubtedly, there are many people without whom this thesis would not have been possible.

I am deeply grateful to my thesis Director Saïd ABBOUDI, who patiently taught me how to be a good researcher, and his teachings made this thesis possible. From our first meeting until today, his trust and support have been unfailing. Thank you for always doing your utmost to ensure that my research was carried out in the best possible conditions. Above all, He gives me the opportunity to learn to be a better person. In other words, as a Professor, you are the best I have ever had, and as a person, you are even better.

My supervisor, Dr. Dominique CHAMORET (HDR), I can't thank her enough for her advice, from whom I learned to have a goal-oriented plan, and that was decisive for the success of this thesis. Thank you for your availability and tireless motivation and push to achieve my goal.

I would also like to thank my thesis co-director, Samuel GOMES. I would particularly like to thank him for all the advice he gave me and all the efforts made to make this thesis possible. It was only possible because of you.

Special thanks to Dr. Lucas DEMBINSKI for his invaluable and deep involvement in this thesis. His help was fundamental to the execution of this project.

I would also like to thank Dr. Sudipta BISWAS from Computational Mechanics and Materials, Idaho National Laboratory (INL) - United States of America, for her valuable advice.

I thank Mr. Jean-Michel Aubert for agreeing to follow this thesis within the policies of TotalEnergies.

I would like to express my gratitude to the staff at the ICB-COMM laboratory, especially my Ph.D. colleagues Kheira, Valentin, Monzer, Romaric, and Hichem. Special thanks to Salima for her friendship and support throughout this thesis and to Sophie LAPRADE for her administrative support.

My thanks also go to Professors Jean Michel BERGHEAU and Jean Gabriel BAUZIN for agreeing to report on my thesis. I would also like to thank the other members of the jury, Professors François LANZETTA and Jone Heitor SEBASTIAO, Dr. Sudipta BISWAS. Special thanks to Jean-Pierre CALISTE for the effort to maintain a good relationship between the institutions involved in this project.

During this project's experimental activities, I could count on the help and support of Christophe MONNOT and Rémy LACHAT from our laboratory. Many thanks to all of you.

Special thanks to TotalEnergies Angola and the French Embassy in Angola for their financial support.

I would like to thank my dear daddy Benjamim CUMBUNGA, my dear mummy Maria BUMBA, and all my brothers for their immeasurable moral support.

Finally, to everyone who made this possible.

Dedication

To my family, wife Doroteia, and children Hélmer and Lusiany.

Acronyms and symbols

3DP	3D printing
AM	Additive Manufacturing
ANOVA	Analysis of Variance
CAD	Computer Aided Design
BC	Boundary Conditions
BDF2	Second-order Backward Differentiation Formula
DEM	Discrete Element Method
DOE	Design of Experiments
FEM	Finite Element Method
GMRES)	Generalized Minimum Residual
JFNK	Jacobian-free Newton-Krylov
KMC	Kinetic Monte Carlo Method
LPS	Liquid-Phase Sintering
MAM	Metal Additive Manufacturing
MC	Monte Carlo Method
MD	Molecular Dynamics
MExAM	Metal Extrusion Additive Manufacturing
MIM	Metal Injection Molding
MOOSE	Multiphysics Object-Oriented Simulation Environment
PBP	Physics-Based Preconditioning
PFM	Phase Field Method
SSS	Solid-State Sintering

Contents

List of Figures

List of Tables

1

Introduction

Contents

1.1/ Metal extrusion additive manufacturing

Manufacturing is a complex process that involves various equipment, machines, tools, labor, and chemical or biological processing to create or produce goods. The production process entails a series of interlinked activities that begin with the acquisition of raw materials and end with the delivery of the final product to the consumer. These activities may vary depending on the nature of the product, the scale of production, and the available resources. The manufacturing process is not limited to any particular method or technology. It encompasses a diverse range of human activities, from traditional handicrafts to cutting-edge technologies, but is most commonly associated with industrial design. The manufacturing process has undergone significant changes over the years, with new technologies and innovations being developed to improve efficiency and quality. During the manufacturing process, raw materials are processed and transformed into the final product. This involves a series of operations, including mixing, cutting, molding, shaping, assembling, and finishing. The quality of the final product depends on the accuracy and effectiveness of these operations. Therefore, the manufacturing process requires skilled labor and advanced machinery to ensure the production of high-quality goods that meet the demands of consumers. Manufacturing plays a crucial role in meeting societal needs, and industries and researchers work tirelessly to enhance, refine, and streamline manufacturing processes. This involves the development of new technologies, the optimization of existing processes, and the adoption of sustainable practices that minimize environmental impact. By continually improving the manufacturing process, industries can produce goods more efficiently, reduce waste, and deliver high-quality products that meet the evolving needs of consumers.

Metal extrusion additive manufacturing (MExAM) is a modern, cutting-edge manufacturing process that builds upon the advancements made in traditional manufacturing

processes such as Material Injection Molding (MIM) and Metal Injection Molding (MIM). MExAM is a process that uses 3D printing technology to create intricate and complex geometries, making it a preferred choice for manufacturing components with challenging shapes and designs. Additive manufacturing (AM) technology has been gaining popularity in recent years due to the benefits it offers in the engineering field. The process involves building up the material layer by layer to create a final product, unlike traditional manufacturing processes that remove material to create a final product [1]. In MExAM, the process involves three main stages: Design, Shaping (Printing), and **Sintering**, see Figure 1.1. The design stage involves creating a 3D model of the component to be manufactured. The shaping stage is where the component is printed using 3D printing technology. Finally, the sintering stage involves heating the printed component until the metal particles bond together, creating a solid metal part. The sintering process is usually preceded by a debinding process, which can be thermal or chemical. The debinding process removes the binder material used in the shaping stage, leaving behind a **porous structure**. The sintering process then bonds the metal particles together, closing the pores and creating a solid metal part. This process results in a product that is strong, precise, and has excellent mechanical properties. In summary, MExAM is a revolutionary manufacturing process that has the potential to change the way we manufacture complex components. Its ability to produce intricate and complex geometries, coupled with its excellent mechanical properties, makes it an attractive choice for various applications in different industries.

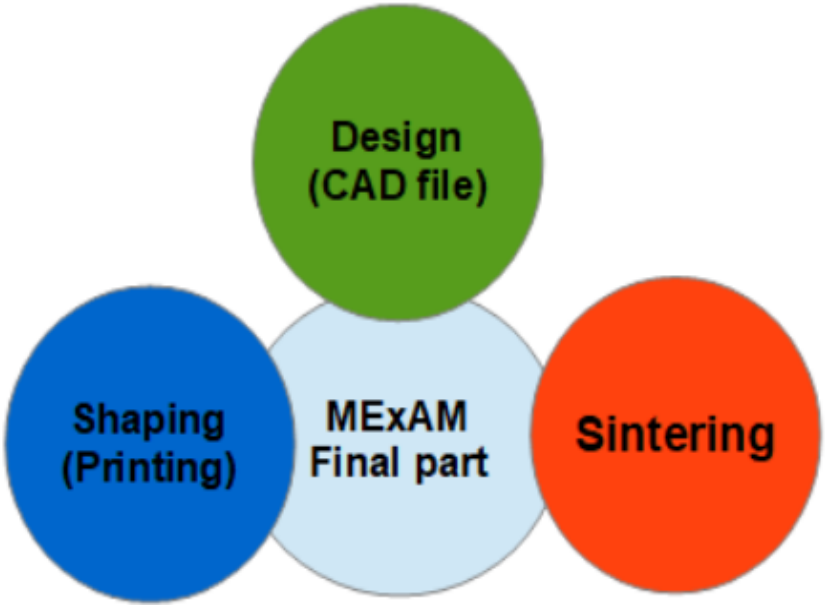

Figure 1.1: Main steps in MExAM.

Various Additive Manufacturing Techniques, such as Powder Bed Fusion (including Selective Laser Melting (SLM), Selective Laser Sintering (SLS), direct metal laser sintering (DMLS), and Electron Beam Melting (EBM)), material/binder jetting, and Direct Metal Deposition (DMD), Shape Metal Deposition (SMD), and Plasma Deposition Manufacturing have been applied to process metallic materials [1, 2]. However, metallic objects produced using these techniques come at a high production cost and are sold at relatively expensive retail prices. Whereas the Additive Manufacturing (AM) process using extrusion solidification, which includes metallic materials, has cheaper equipment costs, lower production costs, a mechanically simple design, and is easy to operate [1]. This technique

involves creating a 3-D object by softening materials and depositing layers using techniques such as Fused Deposition Modelling (FDM).

Although the technique of MExAM is quite useful, it has some limitations. For instance, it results in poor surface finish, dimensional inaccuracy, low resolution, and weak mechanical properties due to defects like high porosity, insufficient compaction, and inadequate adhesion between layers. This means that the final part, before application, requires excellent post-manufacturing treatment to achieve optimal results. So, to achieve the desired properties and characteristics of a material, such as increased strength, durability, and improved functionality, the **sintering process** is utilized. This involves heating the material, typically the **green part**, to a temperature just below its melting point but high enough to cause the particles to bond together, resulting in a denser and stronger structure. The sintering process can also be used to remove any impurities and defects from the material, resulting in a higher-quality end product. In other words, the solid-state sintering process should be applied to improve the material's properties and make it suitable for its application.

1.2/ Solid-state sintering

There are two primary types of sintering, which are pressureless sintering and pressure-assisted sintering. Within the pressureless sintering, we can find the Solid-State Sintering process, which is a thermal treatment technique of compacting and forming a solid material using heat but without melting the material. The sintering process is primarily aimed at reducing porosity and improving material properties such as strength, electrical conductivity, translucency, thermal conductivity, etc. However, in some special cases, sintering is applied to increase the material's strength while preserving porosity (for example, in filters or catalysts, where gas absorption is a priority).

1.2.1/ Applications

Due to its ability to process parts with complex geometry (shape), high dimensional accuracy, small sizes, and suitability for soft and hard materials, sintering has been applied in an emerging way, both in conventional (automotive, aerospace, etc.) and advanced industries. Figure 1.2 depicts some applications of sintering-based MExAM parts.

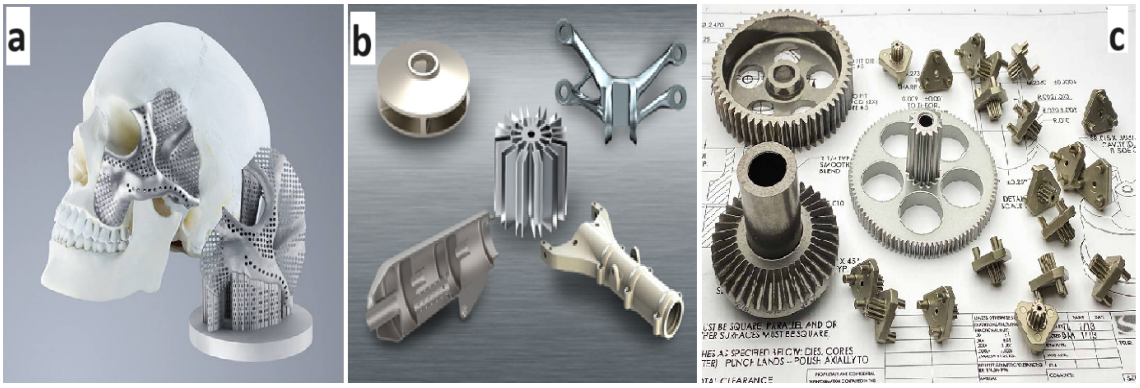

Figure 1.2: Some applications of sintering-based MExAM parts. a) biomedical implants, b) parts with complex geometry, and c) machine parts.

Even though it has been practiced for a long time, sintering has continually found new applications. For example, new energy systems, such as solar cells and nuclear reactors, are critically contingent on sintered structures. The production of porous tissue scaffolds for biomedical implants, and the fabrication of dental crowns and bridges. Recently, there has been considerable interest and effort in pushing forward the sintering of thin printed electronic structures, thermoelectric junctions, and long-lasting oil and gas drilling tools (e.g., bonded sintered diamond and cemented carbides). Finally, sintering is a key step in the development of ceramic-based solid-state electrolytes that are critical for new batteries with improved energy efficiency and safety. Therefore, the development of the sintering process will continue to be extremely important given its wide application and the trend towards future applications.

1.2.2/ Computational Modeling Challenges

Sintering is a multiphysical and multiscale phenomenon. In terms of scale, it can be characterized as small-scale (atomic level), mesoscale (particles, grains, and pores level), and continuum scale (component level). All of these models are discussed in Section 2.4. In the industry, proper processing parameters are mainly obtained by trial and error. Computer simulation can save costs and provide more valuable references or guidance for actual production compared to actual sintering tests.

Modeling of the solid-state sintering process at the small scale has been gaining ground in both research and industry, this type of approach has been applied to avoid coarsening during the sintering process to maintain the nanostructure [3]. To study this phenomenon at this scale, atomic simulation based on the Molecular Dynamics (MD) model has been widely applied [4, 5]. The main advantage of this model is the ability to capture the evolution of thermodynamic and kinetic properties of the material, such as specific interfacial energies, diffusion coefficients, and grain boundary mobility. However, some limitations restrict the wide application of this model, such as the fact that the computational cost is quite high, making it impossible to apply it to more than two particles, and the simulation scale, in the order of nanometers and nanoseconds, making the model irrelevant to any industrial practice, where the processing time is minutes or even hours [3].

The Computational model of the solid-state sintering process at the particle level and applied to the mesostructure level, is the most mature of the three existing levels or scales [6, 7]. The development of this model in order to bring it closer to reality has been one of the main challenges for researchers since sintering is considered to be a microstructural phenomenon. The main advantage of this model is the ability to naturally describe the evolution of arbitrary microstructures (2D and 3D) without explicitly following interface positions or imposing *ad hoc* assumptions about microstructure evolution [3, 8, 9]. However, the main aspect that should be highlighted as a limitation is that the kinetic laws governing the evolution of the microstructure are nonlinear and, therefore, difficult to solve numerically when coupled with other physical phenomena and for a large study domain, which makes it, on the other hand, very expensive computationally [3].

The computational model of the solid-state sintering process at the component level is widely applied to simulate the final component size and shape, density and other materials properties, and defects [10]. The main advantage of this model is the ability to predict the evolution of the shape and size and the deformation of the component, making it a useful and very promising approach for the industry. However, some aspects should be

highlighted as limitations: The model is unsuitable for predicting the evolution of material properties because it considers the microstructure to depend only on two state variables, i.e., relative density and average grain size. This is over-simplistic and may be responsible for the poor predictions of the FE simulation [10, 11]. On the other hand, the current generation of constitutive laws cannot consider some material details such as chemical impurities, particle size distribution, and the sintering atmosphere as input. The other limitation is the difficulty of calibrating its constitutive laws because the material-related constants are obtained through a complex, lengthy, and expensive experimental process.

1.3/ General context and rationales for this thesis

Once MExAM's potential to produce parts with complex geometry (shape), high dimensional accuracy, small dimensions, and suitability for soft and hard materials has been confirmed, it became a promising technology to be applied to different fields, such as industry, health, household appliances, etc. In order to satisfy customer needs and follow the natural process of technological evolution, MExAM has been constantly evolving since its discovery. As Figure 1.1 illustrates, sintering is one of the stages of MExAM, which is applied as a heat treatment primarily aimed at improving the properties of the part in view of its application, without, however, having a negative impact on the geometry (shape), size and dimensions of the part. Therefore, improving the sintering process implies improving MExAM.

Experimental activities based on trial and error are usually expensive and time-consuming, so combining these activities with computer simulation or making these experiments fully computational can reduce cost and time. In this context, computer modeling of the sintering process has become increasingly relevant. Two major challenges dominate the research associated with computer models of sintering:

1. Meso-scale model. Because of its ability to predict the evolution of the microstructure at a scale (domain size), it is possible to capture the material's behavior during the process. Current models have been simplified in terms of the domain under study and the types of phenomena to be considered, with a certain limitation in this respect.

2. Macro-scale model. Because of its ability to predict the evolution of the shape, size, stress, and strain of the part, allowing it to be applied in a more efficient way. However, the equations that govern the behavior of the material at this level are strongly dependent on the constants obtained experimentally, which are difficult to calibrate.

The strategy of crossing and linking both, also known as the multiscale approach, may improve the predictive capacity of computational models to predict the whole solid-state sintering process. Coupling both models to simulate sintering holistically remains a challenge for researchers, not only because of the need to define a precise and adequate coupling channel but also because both models need to be matured. In this context, special attention should be paid to the meso model, not only for its ability to predict the evolution of the microstructure and the behavior of the material's properties but also as a **potential input data** for the macro model, thus enabling meso-macro coupling (a subject for future work).

1.4/ Motivations and objectives

From a social perspective, the physical and tangible aspects associated with the discovery and application of new technologies end up being much more relevant than their essence and how we can use them effectively to improve our lives. However, from a scientific and/or industrial perspective, the secret lies in fully realizing (whenever possible, fully) the true essence, concepts, and laws governing these technologies. While industrialists are more focused on how to apply different scientific approaches to the development of new products (or services), researchers, on the other hand, have the challenge of adjusting, fine-tuning, and increasingly improving these technologies based on scientific aspects and taking into account cost, time, quality and the environment. And, it seems that the sintering process cannot escape this natural trend. As the literature review (Chapter 2) of this thesis will indicate, most of the research is currently oriented towards modeling issues at the component level (macroscopic scale) and experimental issues, which are really important to make the technology more mature and to advance our knowledge of it, but microstructural issues, at the mesoscopic scale, which define and govern the behavior of the sintering process have been very little explored. The full use of the sintering process at an industrial level is dependent on overcoming a series of challenges. Some scientific problems include, but are not limited to:

- **Computational (numerical) model.** Computer modeling of the sintering process is very complex, and the existing microstructural models are very simple and do not take into account the all phenomena that govern this process. Therefore, the proper coupling of all physical phenomena can bring computer models closer to reality.
- **Multi-physic approach.** The holistic modeling of the sintering process at the microstructural level depends greatly on the type of approach adopted to predict the evolution of the microstructure, and how it is coupled with other physical phenomena. In this project, the phase field equations were selected for this purpose and coupled with the thermal and mechanical fields (more details are presented in chapters 2 and 3).
- **Microstructure evolution.** Sintering is a microstructural phenomenon, but most studies have focused on the "two-particle" model. The extension to more than two particles, consideration of the initial microstructural arrangement, and a mesoscopic scale domain are some of the issues that have not been explored much.
- **Application.** The application of sintering considering the specifications of the process that generates the green part and the initial microstructure before sintering is still a challenge. In this study, issues associated with particle size and number, initial porosity size, the temperature profile and sintering time, and the type of material were considered.

1.5/ Thesis structure

The structure of the thesis is divided into two main parts, see Figure 1.3. The first consists of two chapters, namely the introduction (Chapter 1) and the State of Art, Research Question, and Proposal (Chapter 2). The second part is divided into three chapters, namely the Mathematical Formulation of The Solid-State Sintering Process (Chapter 3),

Numerical Framework (Chapter 4), and Numerical Model Applied to MExAM (Chapter 5).

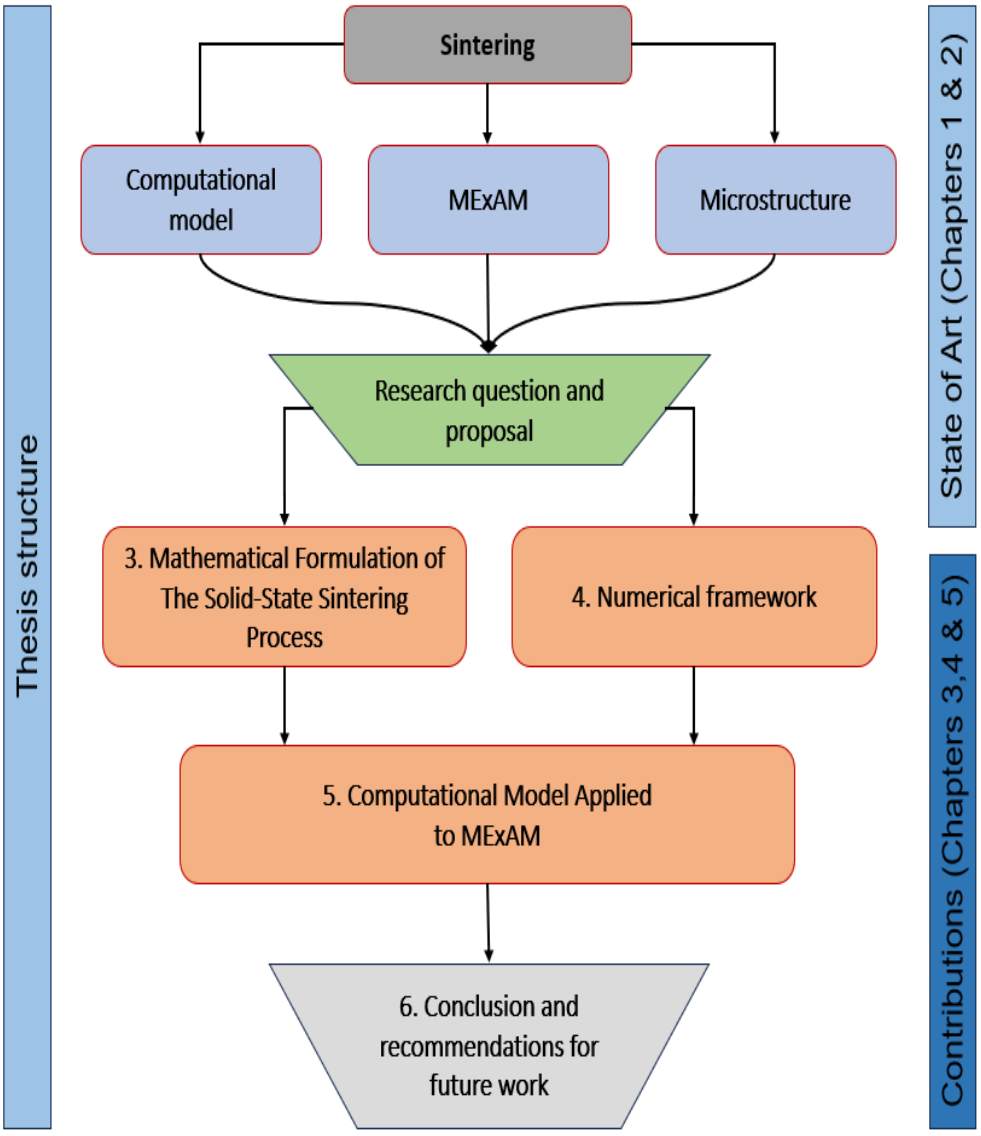

Figure 1.3: Thesis structure.

After this introductory chapter, a literature review will be conducted to gain an in-depth understanding of the concept and also look at it from an application perspective. Then three main contributions will be made to fill the highlighted gaps identified in the literature review (Chapters 3, 4, and 5).

- Chapter 3: Mathematical Formulation of The Solid-State Sintering Process. The aim of this chapter is to present a modeling methodology that takes into account multiphysics phenomena, and how to couple them while respecting their specific constraints.
- Chapter 4: Numerical Framework. This chapter covers the steps used to develop the computational model based on a numerical framework, the model is validated

theoretically by comparing it with cases found in the literature and tested for different scenarios.

- Chapter 5: Numerical Model Applied to MExAM. The aim of this chapter is to apply the computer model to predict and optimize the microstructural and thermo-mechanical behavior of the material, taking into account the MExAM specifications.

Finally, conclusions, perspectives, and future work in this field of research will be presented.

This research work has been done within the ICB (in French: Laboratoire Interdisciplinaire Carnot de Bourgogne) UMR 6303 CNRS laboratory, especially in the COMM (Design, Optimization, and Mechanical Modeling) department, lead by Prof. Saïd ABBOUDI, Prof. Samuel GOMES, and Dr. Dominique CHAMORET. In this department, I was involved in the numerical modeling, simulation, and optimization of the thermomechanical systems team.

2

State of Art, Research Question, and Proposal

Contents

2.1/ Background information

2.1.1/ Sintering concepts

Although there are historical records of artifacts and parts obtained by sintering dating back to around 24,000 BC, the term "sintering" only emerged in the 1800s and became more common in the mid-1900s [12]. Sintering, in its simplest terms, is a heat treatment applied to compact and shaped powder and is one of the most important processes for producing materials [13, 14, 15]. The application of the sintering process began with the processing of clay ceramics and porcelains, and later it was applied to metals such as iron, copper, silver, and others, as well as hard metals like tungsten [12]. Nowadays this process is widely used in the processing of ceramics and almost all types of metals.

Technically, sintering is a processing technique used to produce components and structures with controlled material properties, from metallic or/and ceramic powders by

applying thermal energy with or without external pressure [14, 16]. From a scientific standpoint, sintering is defined as a thermal treatment to bond particles into a coherent, predominantly solid structure through mass transport events that often occur at the atomic scale, which leads to higher strength and lower energy of the system [13, 15, 17].

2.1.2/ Sintering processes

According to Kang [15], sintering is subdivided into two types: Solid-State Sintering (SSS) and Liquid-Phase Sintering (LPS). Solid-state sintering occurs when the compact powder is densified entirely in a solid state at the sintering temperature, while Liquid-Phase Sintering occurs when a liquid phase is present in the compact powder during sintering.

Solid-State Sintering. The material composition and temperature applied are such that no liquid is formed during the process. Densification is achieved by reshaping the powder, which is most commonly accomplished by solid-state diffusion of atoms and is driven by the energy reduction achieved by elimination of the solid-gas interface and replacing it with a solid-solid interface [17, 18].

Liquid-Phase Sintering. The material composition and temperature applied are selected so that some liquid is formed but in a quantity insufficient to fill the residual gas phase solely by viscous flow. Achieving complete densification requires some change in the shape of the solid grains so that the residual gas volume is eventually reduced to the point where the liquid can fill it. A critical advantage of Liquid-Phase Sintering is derived from diffusion in a liquid, which is often hundreds to thousands of times faster than solid-state diffusion [18, 19].

There are typically other types of sintering processes, such as transient liquid phase sintering, and viscous flow sintering [18, 19], However, the different techniques can be distinguished by factors, such as pressure, phases, etc., as illustrated in Figure 2.1.

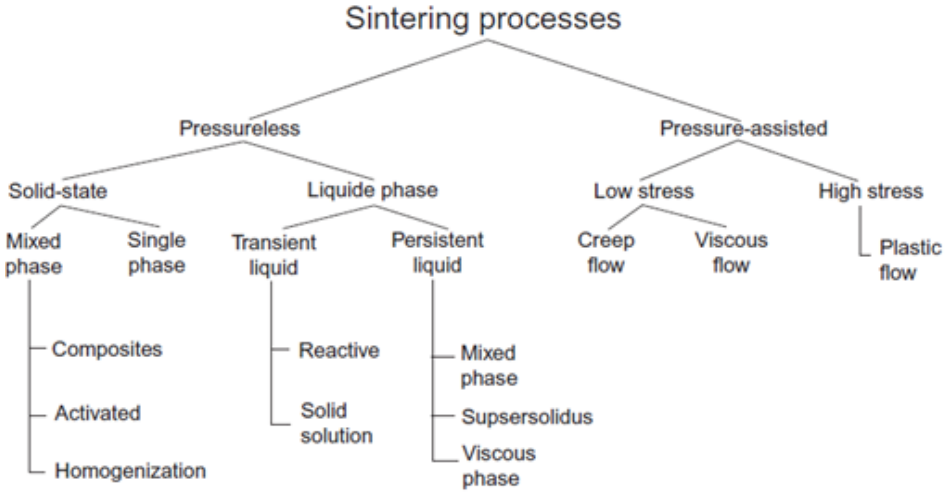

Figure 2.1: Sintering processes (extracted from [13]).

The type of material to be processed, ceramic or metal, and its intended application are the main factors that determine the appropriate sintering process. Generally, Liquid-Phase Sintering is easier to control the microstructure and has lower processing costs compared to Solid-State Sintering. However, it can cause more degradation in certain important properties, such as mechanical properties [15, 19]. Liquid-Phase Sintering is

primarily used to consolidate hard materials, such as TiC-Ni and WC-Co [19].On the other hand, Solid-State Sintering is recommended for processing soft materials, such as metals, allowing the improvement of some material properties, such as density, strength, electrical resistance, and thermal conductivity [20]. Of course, all these properties are also affected by the parameters selected for the material sintering process.

Sintering parameters. The main parameters that determine the sintering process can be divided into two categories [15]:

a. Material parameters related to the raw materials (material variables) include the chemical composition of a powder compact, powder size, shape and distribution, and degree of powder agglomeration.

b. Process parameters related to the sintering environment, such as temperature, time, pressure, heating and cooling rate, and atmospheric conditions.

Studies have revealed that the heating rate, sintering time, sintering temperature, and sintering atmosphere are the key factors in the sintering cycle, independent of the metal manufacturing process to be applied. [21].

2.1.3/ Application of sintering process for metal manufacturing

Two metal manufacturing processes that use sintering as a processing step, are Metal Injection Molding (MIM) [22, 23, 24, 25] and Metal Additive Manufacturing (MAM) [1, 26, 2, 27], both processes can be summarized as shown in figure 2.2. In general, it can be said that the difference between the two manufacturing processes lies in the technique used to shape the part or component, where MIM uses molding, while MAM uses 3D printing.

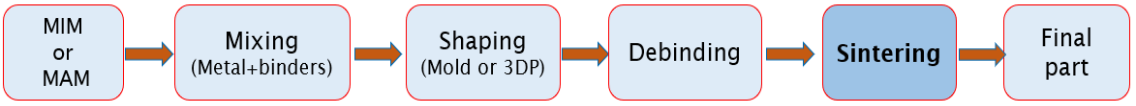

Figure 2.2: General fabrication pattern of sintered parts.

The process of obtaining components or structures by MIM or MAM (considering the material extrusion technology) involves four processing steps [21, 27]:

1. Mixing (material to be processed) – compounding sinterable metal powder with suitable organic binders into feedstock for MIM, or filament or pallet for MAM;

2. Molding – shaping the parts from feedstock with a mould to create the injected part (MIM), or with a 3D Printer to create the printed part (MAM), getting the "green part";

3. Debinding – removing the organic binder in the molded or printed parts through a solvent (optional) and thermal debinding;

4. Sintering – densifying the debound parts to a high final density in a controlled atmosphere.

For both MIM and MAM, sintering is a crucial step, that affects the final density as well as the material properties of the sintered part.

Among the various technologies applied for MAM, material extrusion technology integrates sintering, also known as solid-state sintering, as a processing step [26, 27].

2.2/ Solid-state sintering

Solid-state sintering is the bonding and densification of particles by the application of heat below the melting point of a material [15, 20, 28], and it is the relevant mechanism for crystalline materials. The features of the sintering of crystalline materials include surfaces, grain boundaries, and line defects (including surfaces and boundaries that are the focal points for matter transport) [29].

2.2.1/ Driving force for sintering

At first, the initial configuration of the particles that form the green part is far from the equilibrium state, due to the excess free energy that exists due to the large surface area of the particles and defects (porosity). Therefore, the reduction of free energy is considered to be the driving force of sintering. As sintering proceeds, porosity decreases, leading to a reduction in the solid–vapor interfacial area. The solid–vapor interfaces are replaced by solid–solid interfaces. When grain growth occurs, the solid–solid interfacial area also decreases [29].

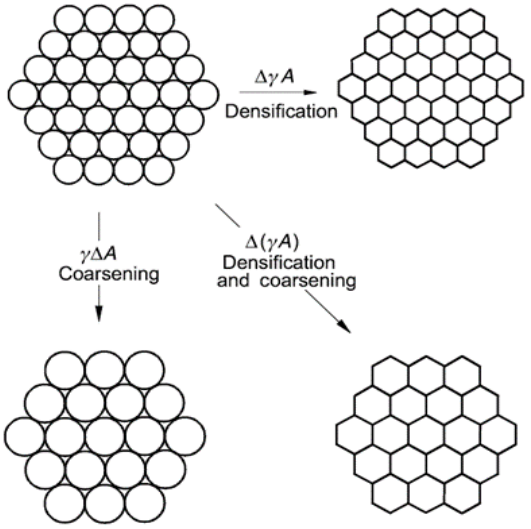

Figure 2.3: Basic phenomena occurring during sintering under the driving force for sintering (extracted from [15]).

The total interfacial energy of a powder compact is expressed as γA, where γ is the specific surface (interface) energy and A the total surface (interface) area of the compact. The reduction of the total energy is [15]:

$$\Delta(\gamma A) = \Delta\gamma A + \gamma\Delta A \tag{2.1}$$

Here, the change in interfacial energy ($\Delta\gamma$) and in the interfacial area (ΔA) are due to *densification* and grain *coarsening* respectively. The combination of these two phenomena (the basic sintering phenomena) lead to the reduction in total interfacial energy (see Figure 2.3) [15, 29, 30].

For solid state sintering, $\Delta\gamma$ is related to the replacement of solid/vapor interfaces (surface) by solid/solid interfaces [15]. In practice, densification and coarsening are con-

current and competing processes since they both reduce the driving force for sintering (excess surface energy) [29].

2.2.2/ Sintering stages

Sintering can be distinguished into three stages that transform the green part into the dense part during the process. As Figure 2.4 indicates, the stages are initial, intermediate, and final.

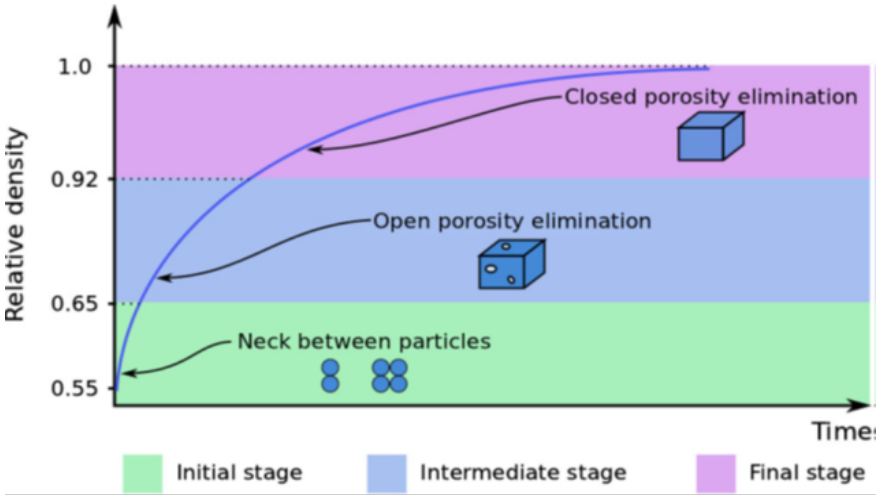

Figure 2.4: Basic phenomena occurring during sintering under the driving force for sintering (extracted from [31]).

Initial stage [20, 29, 31]**.** The neck that bonds the particles together is quickly created and it is still possible to distinguish the system of particles that compose the green part (Figure 2.4). A simple model for the initial stage called *two-sphere model*, was developed to capture all the important features necessary for understanding sintering (Figure 2.5).

Table 2.1: Mass transport mechanism during sintering [3][18].

Transport path	Source of atoms	Sink of atoms	Densification
1. Surface diffusion	Surface	Neck	No
2. Lattice diffusion	Surface	Neck	No
3. Vapor transport	Surface	Neck	No
4. Boundary diffusion	Boundary	Neck	Yes
5. Lattice diffusion	Boundary	Neck	Yes
6. Lattice diffusion	Dislocations	Neck	Yes

This model distinguishes at least six mechanisms (Table 2.1) leading to the necks growing and/or solid densification through various mass transport mechanisms (surfaces and grain boundaries diffusion, bulk lattice diffusion), as well vapor transport (via evaporation and condensation). Matter can be transported to the neck region through the gas phase (by evaporation from the convex surface and condensation on the concave surface), surface diffusion (from convex surface to concave surface), lattice diffusion (from either the convex surface or the grain boundary), or grain boundary diffusion.

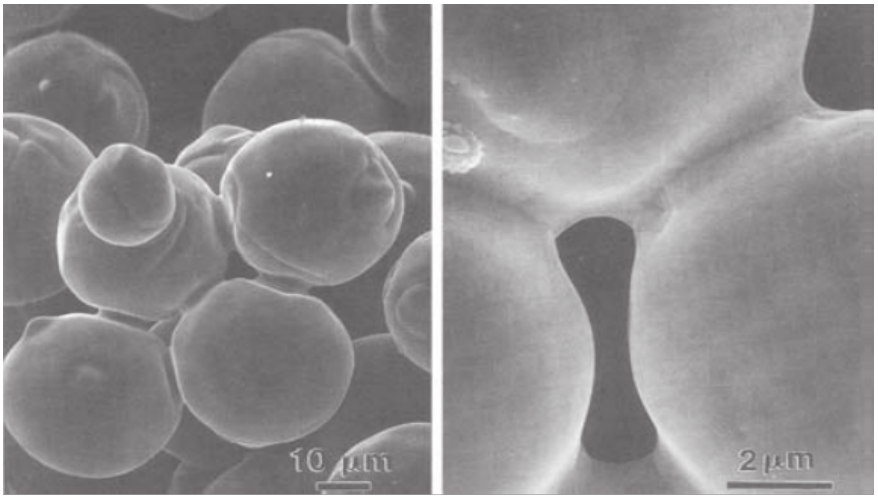

Figure 2.5: Neck created between the particles during sintering (extracted from [20]).

In all matter transport paths as shown in Figure 2.6a, the driving force is the reduction of the total free surface area, which is directly related to the surface free energy of the system [31, 32].

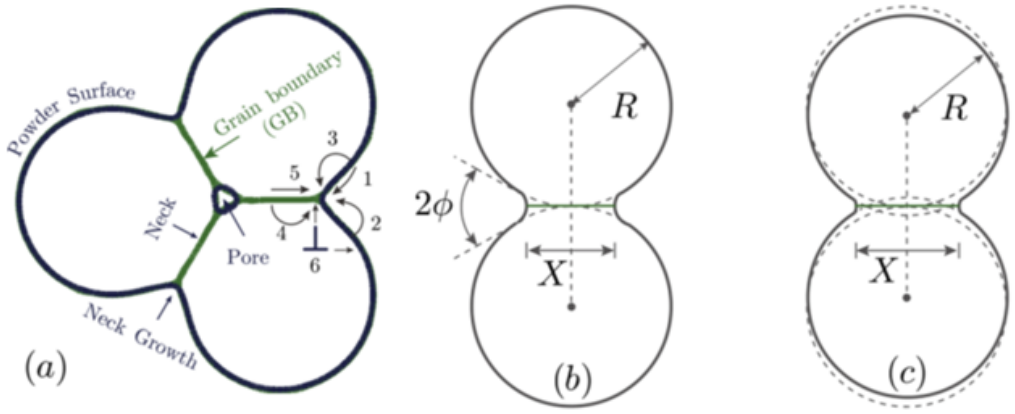

Figure 2.6: (a): Three particles undergoing sintering bonding that involves various mass transport mechanisms. (b): non-densifying and (c): densifying mass transport mechanisms. R is particle radius, X is the neck size, and 2ϕ is the dihedral angle (extracted from [32]).

Intermediate stage [15, 20, 29, 31]**.** The porosity remains open at the beginning of this stage, meaning that the pores are interconnected and roughly cylindrical. As neck growth progresses, there is a transition in the pore structure to a system of tubular pores lying along the particle junctions. The densification rate is controlled by volume and grain boundary diffusions. This stage covers the major part of the sintering process.

Final stage [33, 31]**.** At this stage, the final microstructure of the material is obtained. The pores, which have become isolated and spherical, continue to shrink until they almost completely disappear. Thus, the rate of surface area release and the annihilation of the grain boundary area is slow. Even so, the sintering path follows the lowest energy geometry.

2.2.3/ Microstructure and material properties changes

After sintering, components or structures are durable and strong, but the green part before sintering is relatively weak. Several remarkable changes occur due to sintering, for example, an increase in strength and density. At the same time, the component often undergoes a dimensional change, usually shrinkage. These are bulk property changes, but the science that explains the changes requires attention at the particle level, i.e. at the microstructural level [34].

Microstructure changes. As shown in Figure 2.7 extracted from [35], the microstructure evolution during sintering can be described by the reduction of porosity, whose evolution varies with respect to sintering parameters (grain size, temperature, and time) and induces changes in material properties.

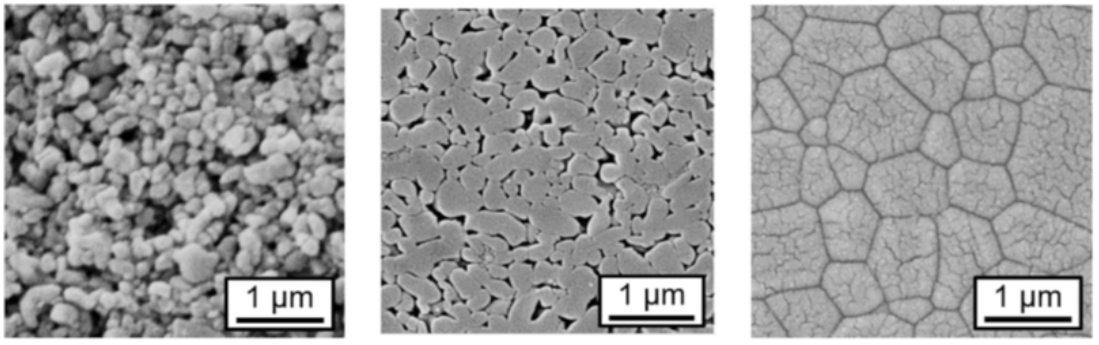

(a) Initial green body (b) After 30 minutes at 1240 °C (c) After 90 minutes at 1240 °C

Figure 2.7: Microstructure evolution during sintering (extracted from [35]).

The sintered microstructure is dominated by its pore and grain structure. Microstructural parameters such as the **neck**, **grain**, and **pore size** are distributed parameters. This implies a characteristic median or mean size with a distribution around that value [34].

Neck size

Necks grow between particles during sintering and their change with time or temperature is the most important aspect of sintering. The neck-size ratio X/D, defined as the neck diameter X divided by the particle diameter D, is the fundamental monitor, as evidenced in Figure 2.8 [34, 36].

This neck measurement is a dimensionless parameter widely used in sintering, known as the neck size ratio X/D. The neck diameter X is measured at the saddle point (see Figure 2.9), which corresponds to the contact at the particle junction. It is characterized by a dihedral angle ϕ that arises at the saddle point. The dihedral angle ϕ reflects the balance of solid-vapor surface energy and grain boundary energy. It is determined by the vertical energy resolution [20, 34, 36], computed as follows:

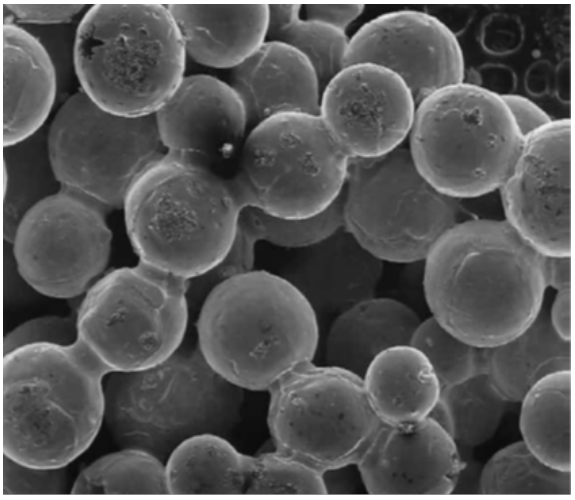

Figure 2.8: Scanning electron micrograph of the sintering neck formed between 26 µm bronze particles after sintering at 800 °C (extracted from [36]).

$$\frac{\gamma_s}{\gamma_{gb}} = 2\cos\left(\frac{\phi}{2}\right) \tag{2.2}$$

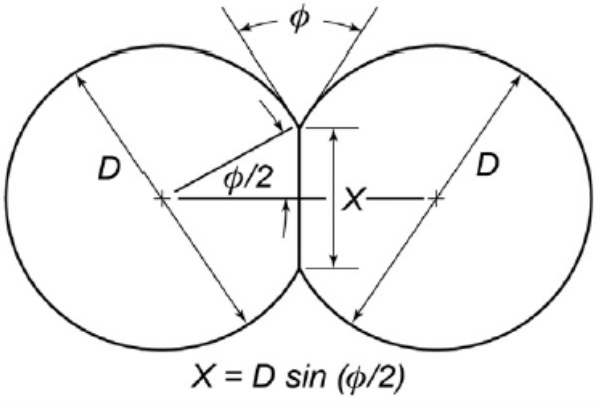

Figure 2.9: The dihedral angle and neck size (extracted from [33]).

Grain size

The initial grain size is one of the parameters that control sintering, and its evolution, usually associated with its growth and changes in shape, describes the microstructure evolution. Grain size is a distributed parameter, meaning the microstructure has a natural distribution. Sintering progresses toward a self-similar grain size distribution, meaning that the distribution is the same shape at long sintering times [34, 36]. The location of the median grain size is the only adjustable parameter. Such behavior is evident in the magnesia data plotted in Figure 2.10. The grain size distribution for sintered materials follows an exponential distribution function (Weibull cumulative distribution). Let $F(G)$ be the cumulative fraction of grains with a size of G, where G_M is the median size, then [34, 36]:

$$F(G) = 1 - \exp\left[\left(\beta \frac{G}{G_M}\right)^M\right] \tag{2.3}$$

here the factor $\beta = -\ln 2$ to ensure that $F(G) = 0.5$ at the median or 50% size when $G = G_M$. The exponent M reflects the dispersion of the distribution. For 2-D data, M tends toward 2, and for 3-D data, M tends to be near 3.

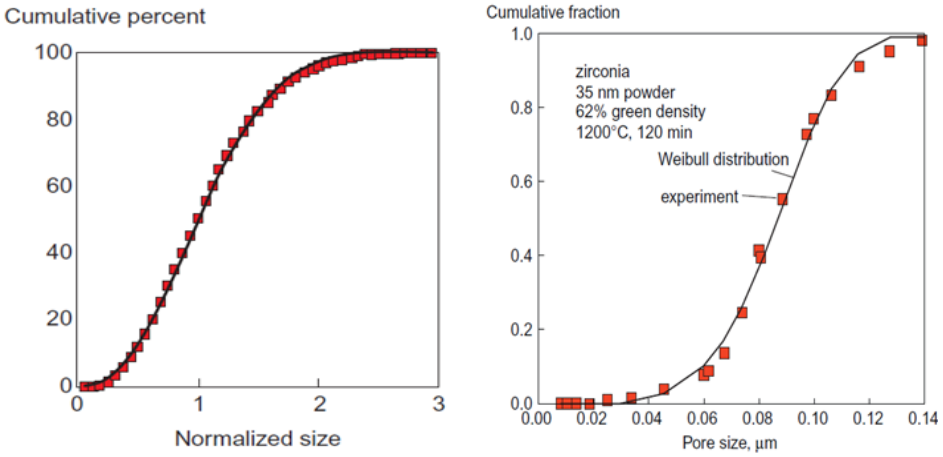

Figure 2.10: The cumulative grain (a) and pore (b) size distribution fit with a Weibull curve, experimental (black continue line), and model (redpoint) (extracted from [34]).

Pore size

Early in sintering the pores are angular, reflecting the gaps between particles. Early in the sintering process, the pores are angular, reflecting the gaps between particles. Sintering works to reduce the curvature gradients, causing the pores to round off and the curvature to tend toward a neutral condition. The microstructure moves from a high level of concavity to a neutral or flat structure. In structures with both large and small pores, the small pores disappear while the large pores remain stable. The pore size distribution transforms to become self-similar, in the same way that the grain size distribution and grain shape are self-similar. The cumulative distribution in pore sizes, d, tends toward a distribution as follows [34]:

$$F(d) = 1 - \exp\left[\left(\beta \frac{d}{d_M}\right)^M\right] \tag{2.4}$$

here the factor $\beta = -\ln 2$ ensures this Weibull cumulative distribution gives a proper fit to the median, that is $F(d) = 0.5$ when $d = d_M$ at the median size. A fit to this distribution is shown in Figure 2.10.

Density, densification, and porosity. The kinetics of densification are typically commonly described in terms of the density or shrinkage of the material as a function of time (isothermal sintering) or temperature (constant heating rate sintering) [37]. The main parameter that characterizes sintering is the relative density f, which can be related to porosity P using the following expression [34, 37]:

$$f = 1 - P \tag{2.5}$$

here $f = \rho/\rho_T$, where ρ is density and ρ_T, is theorical density. It should be noted that during the sintering process, the relative density can reach 0,99 [15, 20, 29, 31, 34], which implies a porosity of about 1%. The relative density is also related to densification, where Ψ indicates the relative change in density normalized to the density change required to achieve full density, which can be computed using equation (2.5):

$$\Psi = \frac{f - f_0}{1 - f_0} \tag{2.6}$$

where f_0 is the initial relative density. At the start of sintering, the densification is zero. If the material is sintered to full density ($f = 1$), then densification is unity. Another parameter related to porosity is shrinkage $\Delta L/L_0$, which is the change in component size divided by the initial size before sintering. In a homogeneous green body, each dimension should exhibit the same shrinkage. The final volume is much smaller than the initial volume, while the mass remains the same, hence a density increase is associated with shrinkage [34].

$$f = \frac{f_0}{\left(1 - \frac{\Delta L}{L}\right)^3} \tag{2.7}$$

Mechanical and thermal properties. The use of components or structures manufactured through the sintering process has become increasingly common, and thus a careful analysis of the interplay between "application and costs" has been crucial in configuring the process. Porosity is detrimental since pores reduce the load-bearing cross-sectional area and act as incipient cracks. Eliminating pores is an obvious requirement for advantageous mechanical properties. Two mechanical properties commonly used to track sintering are strength (fracture resistance) and hardness (penetration resistance) [34].

Thermal properties are important also for applications in computers, electronics, and electric power. For instance, pores negatively affect conductivity. An important consideration during sintering is thermal stresses induced by sudden, non-uniform heating, which can cause distortions that damage the component or structure. To avoid this, heating rates are often limited to 5-25°C/min [15, 20, 29, 31, 34, 36, 37].

2.3/ Sintering-based metal extrusion additive manufacturing

As presented in section 2.1, sintering has become a key step in obtaining metal components or structures through additive manufacturing using material extrusion technology. Manufacturing components or structures with complex geometry and specific functionalities for their application has been a significant challenge for researchers. Additive manufacturing, also known as 3D printing [38, 39, 40] combined with sintering [27, 41, 42], has increasingly emerged as a promising alternative to solving this particular problem for metal components or structures.

The manufacturing process for metal additive manufacturing is divided into four steps: design, printing, debinding, and sintering [27, 40, 41]. Although these parts can be produced with high geometrical accuracy and relatively low cost, they often suffer from

high porosity and poor surface finishes [40]. To address these issues, sintering is often applied. This section presents metal extrusion additive manufacturing (MExAM).

MExAM is an additive manufacturing process classified as a solid-state process based on sintering (see Figure 2.11). This technique takes advantage of the knowledge base of powder metallurgy and sintering technology [26]. This process involves softening a metal and pushing it through a nozzle to deposit the material in layers to build the 3D structure [1, 41].

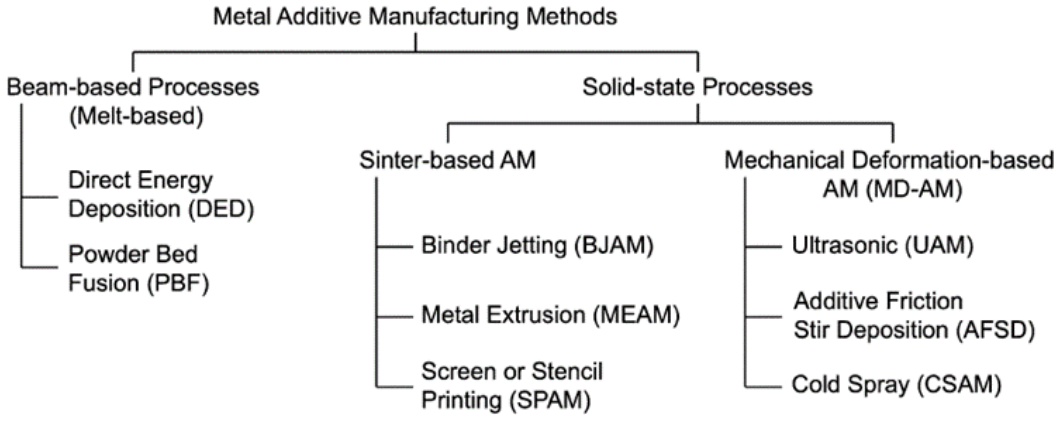

Figure 2.11: Classification of AM processes based on material bonding methods (extracted from [26]).

Depending on the feedstock, the MExAM process can be classified into three types [2, 27, 41], as presented in Figure 2.12, screw-based, plunger-based, and filament-based.

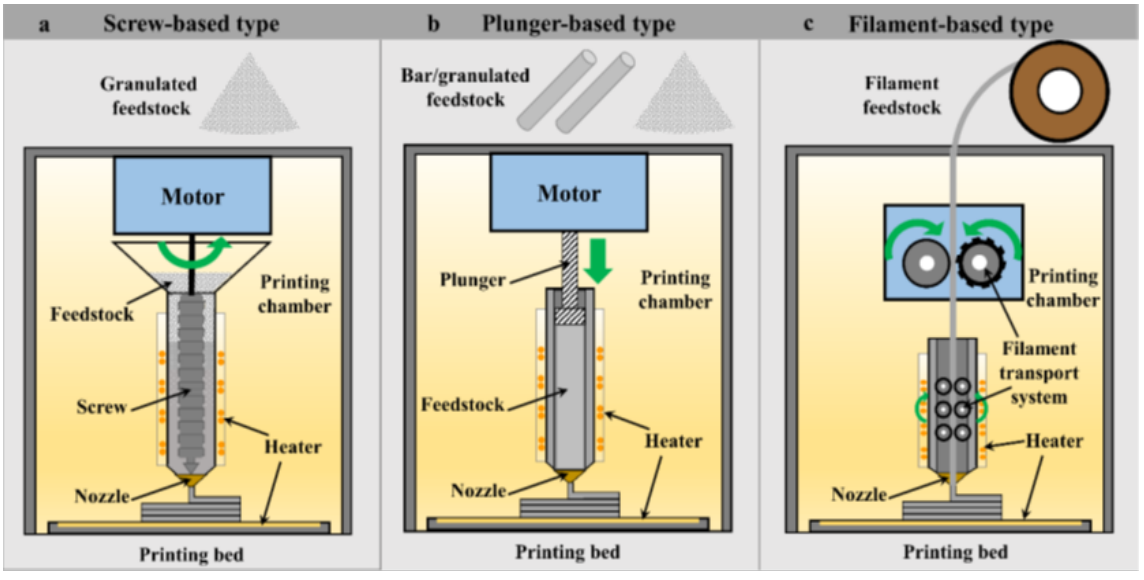

Figure 2.12: Type of MExAM classified by feeding system (a) screw-based, (b) plunger-based, and (c) filament-based (extracted from [27]).

In general, the production of components or structures by MExAM can be summarized in three steps (see Figure 2.13), namely:

1. **Printing** – process that allows the layer-by-layer construction of complex shaped "*green part*" using 3D model data and engineering materials, without the need for conventional manufacturing tools [1, 26, 38, 40, 41].

2. **Debinding** – process to remove the polymer binder (backbone[1] and soluble binder[2]) after printing to create a "*brown part*", forming a skeleton of metal powders ready for sintering. The main debinding techniques are thermal, solvent, and catalytic methods, and they can be applied separately or in combination [1, 27, 41].

3. **Sintering** – process to thermally treat the *brown part* to bond the metal powder so that densified components can be achieved. At this step, conditions for obtaining near-total density (up to 99%) are created using high temperatures, but below the melting point of the metal [1, 27].

As can be seen in Figure 2.13, before the sintering, a set of particles of different sizes, randomly distributed, generate equally randomly distributed pores of different sizes.

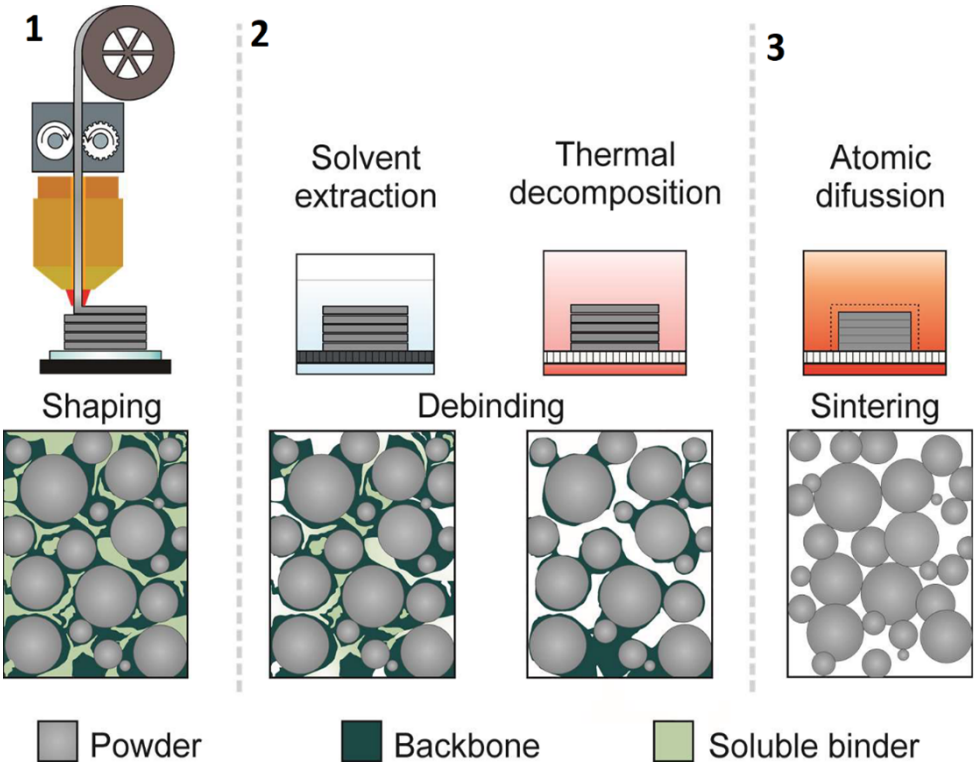

Figure 2.13: Schematic representation of the shaping, debinding, sintering process, and respective morphology of the parts for the fabrication of metal (extracted from [41]).

This significant presence of porosity is the main cause of the defects commonly found before the sintering process, making the material properties (thermal, mechanical, etc.) unsuitable for their intended application. Therefore, improving the material properties for their intended application has been one of the major challenges for sintering researchers.

[1]Backbone - is the component used to hold together the shape of the part while the main binder component is removed during the first debinding stage, thermally removed [41].

[2]Soluble binder - materials that dissolve in water or other solvents, or those that undergo catalytic degradation [41].

2.3.1/ Sintering challenges in the MExAM context

Ease of use, relatively low production cost, and ability to manufacture large and complex components or structures are some of the significant advantages of MExAM that have sparked the interest of companies and researchers to improve this technology. The first papers on MExAM were published between 1996 and 2015, and since then there has been a considerable increase in the number of publications [27]. While the design, printing, and experimental characterization of the material has been the main areas of research, little to no study has been done on computational models to evaluate the behavior of the material obtained by this technology during sintering.

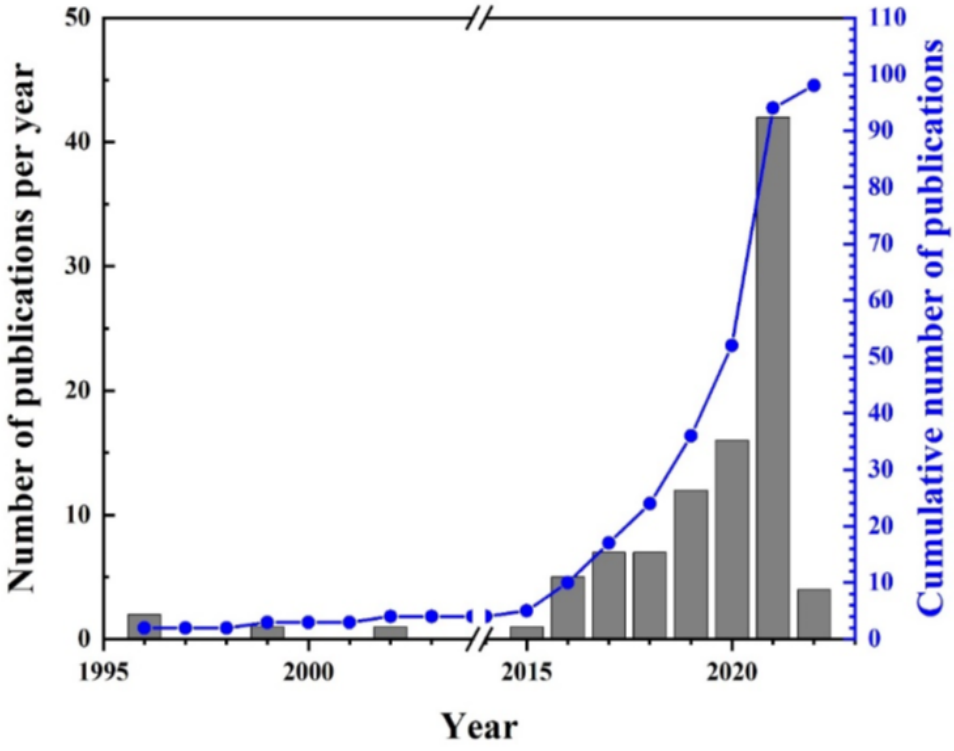

Figure 2.14: Number of publications relating to the MExAM from 1996 to February 2022 (extracted from [27]).

Two approaches should guide research on sintering in the context of MExAM: experimental and computational. Experimental characterization is based on analyzing the geometry and microstructural arrangement of the green part, the material type, and the sintering atmosphere and variables. The data obtained through the experimental characterization should be used as input data and to adjust the computational model, which should predict the material's behavior at the microscopic and/or macroscopic levels.

One of the main causes that limit the application of the component or structure obtained by this technology is associated with poor mechanical properties attributed to porosity [1]. Thus, the main questions and difficulties for researchers are [1, 2, 27, 43]:

1. Control the evolution of the microstructure considering the material and the desired results.

2. Enhance material properties (thermal, mechanical, etc.) for a wider range of applications (medical, aerospace, etc.).

3. Optimize the sintering process, focusing on material, application, and processing.

4. Develop computational models capable of predicting microstructural (grain size and shape, porosity, etc.) and/or macrostructural (final component size, residual stress, etc.) evolution.

2.4/ Computational modeling of sintering

To ensure the optimal performance of components or structures during their use, as well as to develop robust processes and to significantly reduce the rejection rate during production, many works have been carried out to develop computational models capable of predicting the sintering process [3]. From the 1960s to the present day, many models have been developed, starting with the underlying mechanisms during the sintering process and sintering mechanism maps, through models on the atomic and particle level, and models based on full constitutive laws for finite element analysis of sintering [3, 6, 7, 11, 10]. In industries, proper processing parameters are mainly obtained by trial and error. Computer simulation can save costs and provide more valuable references or guidance for actual production compared to actual sintering tests.

The literature indicates that computational models of solid-state sintering are usually framed in a microscopic [8, 10, 11, 31, 44, 45, 46] and macroscopic approach [3, 6, 10, 47, 48, 49, 50], but a multiscale approach has been emerging that results in the combination of the micro-macro scales [3, 4, 6, 51, 52]. Figure 2.15 shows the different computational models that exist for modeling the solid-state sintering process, which will be discussed in this section.

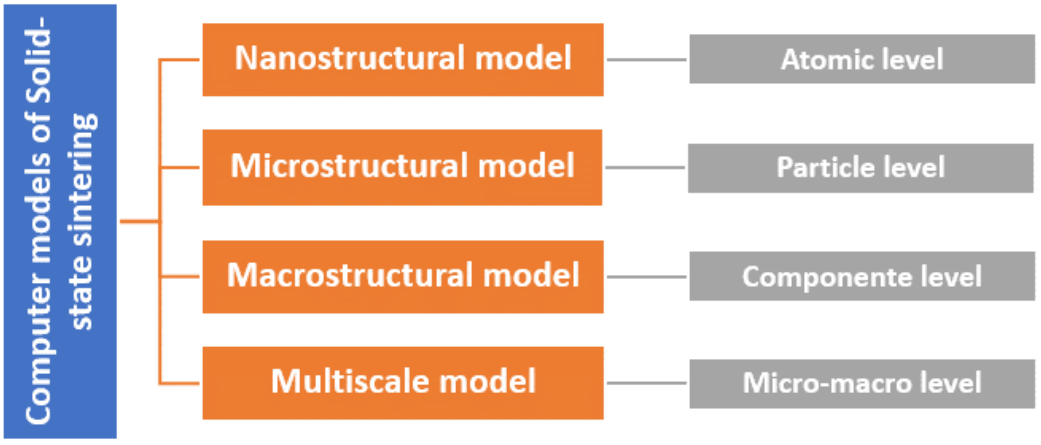

Figure 2.15: Different computational models for modeling the solid-state sintering process.

As shown in Figure 2.15, various computational models are applied to model the solid-state sintering process, ranging from the atomic level to the component level, with each model having its own specifications in terms of input and output data (see Table 2.2). Thus, this section aims to present, in a summarized way, the usefulness and accuracy of each model, as well as its limitations. It also presents the main numerical techniques

used and the current application of each one in the modeling of the solid-state sintering process.

Table 2.2: Summary of input and output data of sintering models at different levels [3], [6], [10].

Level	Input data	Output data
Molecular Dynamics (MD)	1. Interatomic potential and its parameters 2. Crystalline structure with periodical boundary conditions. 3. Temperature.	1. Time evolution of positions and velocities of all the atoms. 2. Specific interfacial energies. 3. Diffusion coefficients and grain boundary mobility.
Particle model	1. Kinetic law for diffusion and grain 2. Specific interfacial energies. 3. Diffusion coefficients. 4. Initial microstructure. 5. Temperature and boundary conditions.	1. Time and spatial evolution of the microstructure (grain boundaries and size, pores, ...). 2. Time history of density.
Component (Continuum finite element)	1. Constitutive and grain growth laws, and their parameters. 2. Initial average particle size, initial density, and geometry. 3. Residual stress fields. 4. Temperature and boundary conditions.	Time history of: 1. Deformation. 2. Stress and strain fields. 2. Density and grain size fields.
Micro-macro (Multiscale)	Combination of particle and component input data	Combination of particle and component output data

2.4.1/ Nanostructure model

Modeling of the solid-state sintering process at the nanoparticle level has been gaining ground in both research and industry, this type of approach has been applied to avoid coarsening during the sintering process to maintain the nanostructure [3]. To study this phenomenon at a very small scale, atomic simulation based on Molecular Dynamics (MD) models has been widely applied [4, 5]. Molecular Dynamics (MD) has been used to study nanoscale sintering in a wide range of materials, such as Al, Au, Si, Ni, Ag, Cu, Fe, and W [44].

Computational model. With MD modeling, it is now possible to simulate the sintering process of a particle cluster at the atomic level. Each particle is modeled as an assembly of a large number of atoms, where the key feature is to assemble a cluster of atoms into spherical particles and set interaction rules between them, where the chemical composition and atomic structure of each particle are explicit in an atomistic simulation. For simulation, two or three atomic clusters are created to represent "particles," (see figure 2.16) where each cluster consists of 10,000 to maybe 50,000 atoms. The material's details, such as interatomic potential and its parameters, crystalline structure, and temperature,

are the input of the simulation. The output is the trajectory of all the atoms from which further results can be obtained, such as the time evolution of positions and velocities of all the atoms, specific interfacial energies, diffusion coefficients, and grain boundary mobility [3, 6, 5, 10, 53].

The computational model is based on the modified embedded atom method, where the total energy F of an atom system depends on the sum of the atomic energies valence [10, 54].

$$F = \sum_i F_i \tag{2.8}$$

The energy of atom i consists of the embedding energy (first term in Eq. (2.9) and the pair potential terms calculated between neighboring i and j atoms (second term):

$$F_i = F_I(\rho) + \frac{1}{2}\sum_i \phi_{ij}(r_{ij}) \tag{2.9}$$

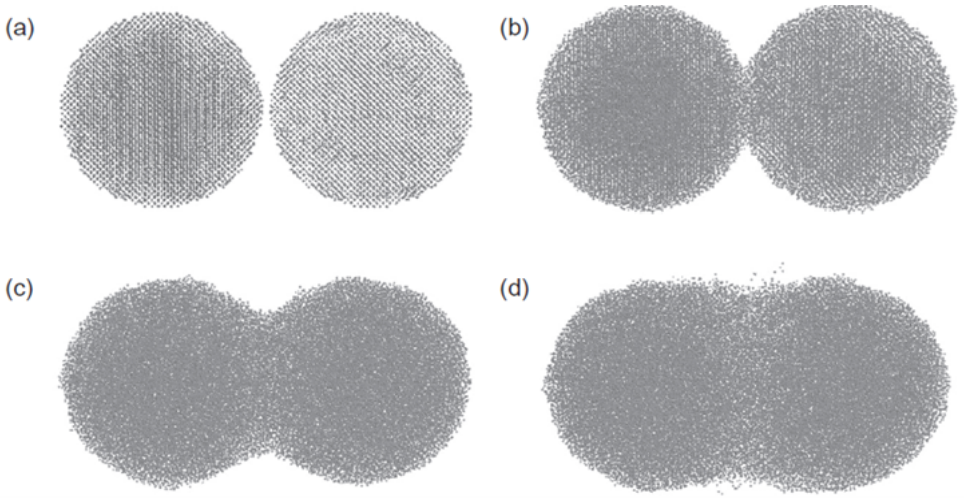

Figure 2.16: A plot of atom positions at three points during computer simulated sintering based on molecular dynamic concepts: a) starting condition just before particle contact, b) after initial stage neck growth, c) about three times longer to a point where particle neck growth is advanced and shrinkage is evident, and d) sintered to the point where the two particles bond to form a single ovoid particle (extracted from [6]).

Pros and Cons. The strength of this model is the ability to capture the evolution of thermodynamic and kinetic properties of the material, such as specific interfacial energies, diffusion coefficients, and grain boundary mobility. In this respect, it is perhaps the most useful among the models [6]. This idea is supported by Sestito et al. [44], who state that the MD model is a suitable approach to investigate at a fundamental level the role of Grain Boundaries (energy, diffusion, and mobility) on the sintering behavior of nanoparticles. However, some limitations constrain the broad application of this model, namely:

1. The interatomic potentials. Whether they can represent the real behavior of the material because it is well known that under certain circumstances the potentials fail

to predict the real behavior and they are accurate only for the range of geometries that is close to the situation for which the potentials were parameterized [6].

2. The computational cost is quite high. For example, more than two-particle and larger particle sizes require more atoms (thousands or millions) and exceed available computational resources [10, 4].

3. To cross the length and time scale. The typical scale of an MD model is nanometers for length and nanoseconds for time, which are much shorter than the characteristic scales of any real sintering process. Thus, these simulations can be considered irrelevant for any industrial practice where the processing time is minutes or even hours [3].

2.4.2/ Microstructure model

The Computational model of the solid-state sintering process at the microstructural level, also known as the particle level and applied to the mesostructure level, is the most mature of the three existing levels or scales [3, 6]. The development of this model to bring it closer to reality has been one of the main challenges for researchers since sintering is considered a microstructural phenomenon.

Computational model. Although there is a wide range of approaches, three approaches predominate, namely the Monte Carlo Method (MC), the Discrete Element Method (DEM), and the Phase Field Method (PFM). In general, the output data of these approaches is related to the temporal and spatial evolution of the microstructure (grain boundaries and size, pores, etc.), which in turn controls the evolution of the material's properties, while the initial microstructure, temperature, kinetic law for diffusion and grain boundary migration, specific interfacial energies and diffusion coefficients are the main input data for the model. Below are some details about the formulations, pros, and cons of each approach [3, 4, 6, 10].

❖ Monte Carlo Method

The Kinetic Monte Carlo method is a probabilistic approach and is a popular technique used to study grain growth and microstructural evolution during solid-state sintering. In this model, the main objective is to ensemble a grid of grain sites that contains the particles and pores in order to populate a square lattice. The grain sites can assume one of Q distinct, degenerate states, where the individual state is designated by the symbol q; $q_{grains} = [1, 2, 3, ..., Q]$ [10, 31, 55, 56].

The driving force for solid-state sintering is the reduction of total free energy but in this model, only the reduction of interfacial free energy is considered. However, the equation of state in the model is calculated as the sum of all neighbor interaction energies of all sites, Eq. (2.10):

$$E = \frac{1}{2}\sum_{i=1}^{N}\sum_{j=1}^{n} J_{ij}\left(1 - \delta(q_i, q_j)\right) \tag{2.10}$$

here i is each site, N is the total number of sites in the system, j is each neighbor of site i, n is the total number of neighbors of each site, J_{ij} is the neighbor interaction

energy between site i and its neighbor j, q_i is the state of the grain or pore at site i and q_j is the state of the nearest neighbor at site j, and the term $\delta(q_i, q_j)$ is the Kronecker delta function such that $\delta(q_i, q_j) = 1$ if $(q_i = q_j)$ and $\delta(q_i, q_j) = 0$ if $(q_i \neq q_j)$. Since only the interfacial energy of the system is defined, only unlike neighbors contribute to this energy. Additionally, all, unlike neighbors, contribute with the same amount of energy. Once the interfacial energy of the system is defined, only unlike neighbors contribute to the energy. Additionally, all unlike neighbors contribute the same amount of energy J_{ij}. The interfacial energy does not depend on the crystallographic orientation of the grains with respect to each other and is isotropic [55, 56]. More details on the kMC application for solid-state sintering simulation can be found here [10, 31, 55, 56, 57].

Pros and Cons. The MC computational model can accurately simulate the 3D geometry of materials and provide valuable information on the evolution of grain shape, size, and density from low to high relative density stages [57]. It is easy to code and extend from 2D to 3D, making it useful for simulating various material evolution processes based on statistical-mechanical principles [56]. However, two limitations should be noted:

1. The kMC method assumes that the interfacial free energy is equal to the total free energy of the system, but in reality, the total free energy is the sum of chemical, interfacial, elastic, and other free energies [55, 56, 57].

2. The kMC method represents microstructural features as a collection of discrete, arbitrary points/quanta of matter, and the stochastic nature of the approach only predicts qualitatively the microstructural evolution, especially because of its limitation in terms of consideration of external loading [58].

❖ Discrete Element Method (DEM)

The DEM model, a particle-based simulation scheme, appears to be a useful tool for analyzing microstructural parameters during solid-state sintering, such as the position, velocity, contact area, and coordination number of each grain [59, 60, 61].In this model, the system's equilibrium is determined by considering mechanical, chemical, capillary, gravity, or other forces between particles [10]. In DEM, each particle is modeled as a sphere (treated as a single element) interacting with its neighbors through appropriate sintering laws. This approach allows the assembly of thousands of particles. See Figure 2.17 [10, 62, 63].

The computational model is based on the Bouvard and McMeeking model, which considers grain boundaries and surface diffusion as the main mass transport mechanisms. Basically, the model combines the normal, and tangential forces, which are a function of grain-boundary $\delta_b D_b$ and surface diffusion $\delta_s D_s$, surface energy γ_s, a contact radius a_s and indentation h, relative velocity at the contact du/dt and dh/dt, and diffusion parameter Δ_b (see Figure 2.18). At each time step, the total contact force on each particle is the result of normal Eq.(2.11), and tangential Eq.(2.12) [62, 63].

$$N_s = \frac{\pi a_s^4}{2\beta\Delta_b}\frac{dh}{dt} - \frac{a}{\beta}\pi R\gamma_s \tag{2.11}$$

The parameters α and β should depend on the ratio of the grain-boundary diffusion $\delta_b D_b$ to the surface diffusion $\delta_s D_s$ [63].

$$T_s = -\eta \frac{\pi a_s^2 R^2}{2\beta \Delta_b} \frac{du}{dt} \tag{2.12}$$

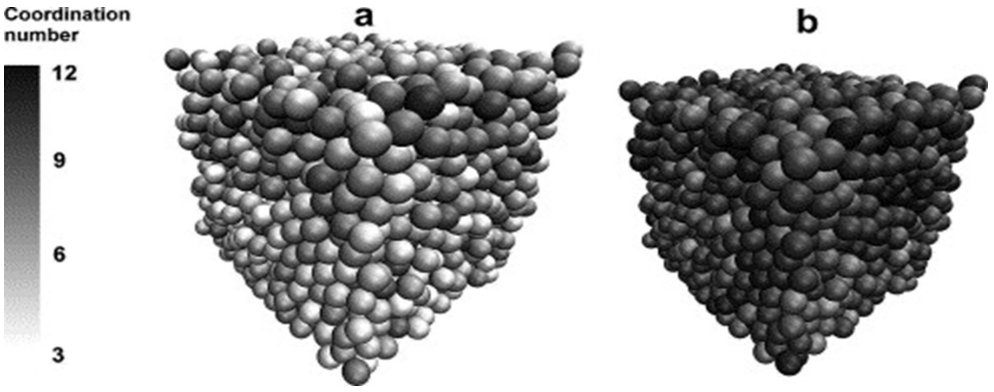

Figure 2.17: (a) Initial state (ρ = 64%) and (b) final state (ρ = 90%) of a typical DEM sintering simulation. About 1800 particles are used in periodic boundary conditions. Each particle is highlighted by its coordination number, which increases during sintering. (extracted from [60]).

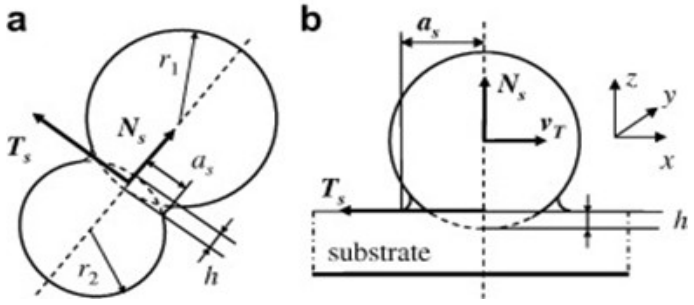

Figure 2.18: The contact geometry between two particles (a), and between a particle and the plane substrate (b) (extracted from [63])

Here η is a dimensionless viscous parameter, and $R = r_1 r_2/(r_1 + r_2)$ as the equivalent radius for two particles of radii r_1 and r_2 [63].

Pros and Cons. The DEM approach is a suitable tool for computing the deformation behavior of microscale components and investigating the effect of particle rearrangements, as it is critically affected by each particle's motion. It's also suitable to simulate a large number of particles (thousands of particles) [59, 60, 64]. Although it is computationally expensive and a quantitative approach, it does not allow obtaining qualitative details about microstructure evolution (temporal and spatial changes in grains, pores, etc.). Other limitations include the fact that it is not a suitable method for high relative density systems due to its simplification of neck size [63].

❖ Phase-Field Method

The PFM has become an important and extremely versatile technique for simulating microstructure evolution at the mesoscale [9] and has been established in the last decades

as a powerful tool to study the microstructure evolution under the influences of various physical phenomena [35, 58]. It has been applied to study different problems, including but not limited to solidification, grain growth, solid-state phase transformations, etc. [9, 65, 66, 67, 68], and it can naturally describe the evolution of arbitrary microstructures without explicitly following interface positions or imposing ad hoc assumptions about microstructure evolution [8].

The first proposal on the PFM application for modeling and simulation of the solid-state sintering process was presented by Wang [36]. Subsequently, several papers based on the same model were presented (see here some examples [35, 69, 70, 71, 72, 73]), Biswas et al. [58] presented a multiphysics approach based on the same model to simulate the solid-state sintering process for two particles (grains).

The PFM is formulated to gain a better understanding of the mass transport (diffusion) and microstructure evolution during solid-state sintering [8, 69, 73]. As a generalized approach to treat multiple ($N > 2$) coexisting phases, the PFM is capable of treating an arbitrary number of individual phases that interact at triple or higher-order junctions [9, 69]. A set of order parameters is used to describe the microstructure, conserved order parameter c, that distinguishes the phases between porous ($c = 0$) and solid ($c = 1$), and non-conserved parameter $\eta(1, 2, ..., p)$, where p is the number of particles/grains, that describe individual grains with different crystal orientations [8, 72]. These parameters are considered continuum field functions (the so-called phase fields), and describe the sizes, shapes, and spatial arrangement of particles of different compositions, lattice symmetries, and crystallographic orientations, i.e., the microstructure evolution during material processing [8].

The reduction of the total free energy through diffusion mechanisms and structural relaxation drives the microstructure evolution. The total free energy of a material is a function of conserved and non-conserved order parameters, that is, the combination of bulk chemical free energy, interfacial energy, elastic energy, visco-plastic energy, and system energy (external energy source) [9, 58], as described in Eq. (2.13).

$$F = F_{chem} + F_{int} + F_{el} + F_{vp} + F_{sys} \tag{2.13}$$

Pros and Cons. In addition to the ability to naturally describe the evolution of arbitrary microstructures (2D and 3D) without explicitly following interface positions or imposing ad hoc assumptions about microstructure evolution [3, 8, 9]. Among other advantages of PFM, we highlight the possibility of coupling it to other physical phenomena, which makes it suitable for modeling the solid state sintering process, as it is a multiphysics process, and the ability to capture all the mass transport mechanisms (diffusion process) that govern the solid-state sintering process, such as surface diffusion, grain boundary diffusion, volume diffusion, vapor transport [8, 58]. However, the main aspect that should be highlighted as a limitation is that the kinetic laws governing the evolution of the microstructure are nonlinear and, therefore, difficult to solve numerically when coupled with other physical phenomena and for a large study domain, which makes it, on the other hand, very expensive computationally [3].

2.4.3/ Macrostructure model

The computational model of the solid-state sintering process at the macrostructural level, also known as the component level, is widely applied to simulate the final component size

and shape, density and other materials properties, and defects [10]. Its formulation is based on a continuum approach, so since the evolution of continuum models goes hand in hand with the use of finite element analysis, therefore the finite element method (FEM) is used to model the solid-state sintering process of a component [3, 6, 43].

Computational model. In such a model, FEM is applied to predict the temporal and spatial density and grain-size fields, which are used to characterize the microstructure, stress, and strain fields and the component's shape, dimension, and deformation. In general, the input data of these approaches is related to constitutive and grain growth laws and their parameters, initial average particle size, initial density and geometry, residual stress fields, and temperature and boundary conditions [3, 10, 48, 50]. The model uses the constitutive law is a linear relationship between the strain and the stresses, as expressed in Eq. (2.14), but if external loads on the component are not too high [48].

$$\dot{\varepsilon} = \frac{\sigma'_{ij}}{2G} + \delta_{ij}\frac{\sigma_m - \sigma_s + \Delta p}{3K} \tag{2.14}$$

Here the prime denotes the deviator, σ_m is mean (or hydrostatic) stress, Δp is a gas overpressure which may develop in closed pores, δ_{ij} is the Kronecker symbol, and σ_s is the sintering stress, which arises from the surface tension forces of the pores.

The constitutive law is completed by a densification rate (Eq. (2.15)) given by the trace of the strain rate tensor, where ρ is the relative density [48].

$$\dot{\rho} = \rho\dot{\varepsilon}_{kk} = \rho\frac{\sigma_m - \sigma_s - \Delta p}{K} \tag{2.15}$$

The constants G and K are shear and bulk viscosity, respectively, and σ_s depends on temperature, density, grain size, total free energy, and other internal variables [3, 48]. For more details about the formulations, see [3, 6, 11, 48, 50, 74, 75].

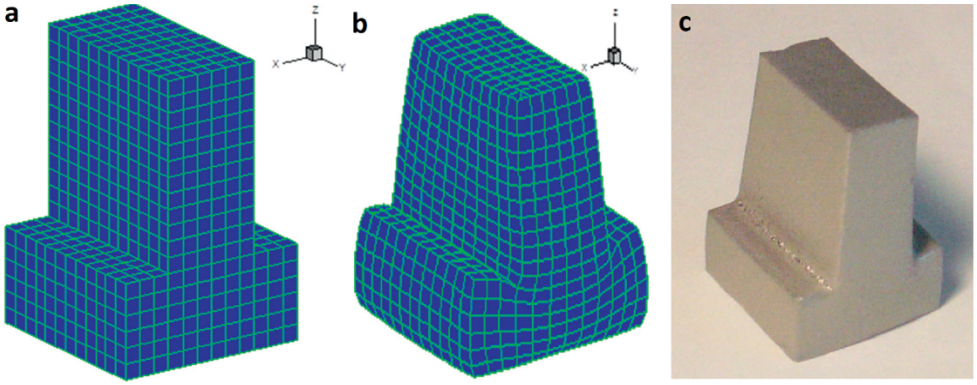

Figure 2.19: An inverted T test geometry before sintering with the finite element mesh: a) gives the initial geometry for the 30 mm high sample, b) gives the predicted shape after sintering where the sample is now 19 mm high, and c) shows the physical sample for comparison (extracted from [33]).

Pros and Cons. The main advantage of the computational model at the component level is the ability to predict the evolution of the shape and size and the deformation of the component, see Figure 2.19, making it a useful and very promising approach for the industry. However, some aspects should be highlighted as limitations:

1. The model is not very suitable for predicting the evolution of material properties because it considers the microstructure to depend only on two state variables, i.e., relative density and average grain size. This is over-simplistic and may be responsible for the poor predictions of the FE simulation [3, 6].

2. Unlike powder compaction, sintering is very sensitive to material details such as chemical impurities, amount and type of doping, particle size distribution, the extent of powder agglomeration, and the sintering atmosphere. The current generation of constitutive laws cannot consider these material details as input. The so-called material constants in the constitutive laws are only constant if all these material details remain unchanged, which is not the case [3, 6].

3. The other aspect emphasized is the difficulty of calibrating its constitutive laws because the material-related constants are obtained through a complex, lengthy, and expensive experimental process.

2.4.4/ Multiscale model

The strategy of crossing and linking models at different scales, also known as the multi-scale approach, in materials modeling to improve the predictive capacity of computational models has begun to impact solid-state sintering modeling [6]. Sintering modeling, as in other areas of materials science, comprises two distinct approaches: microstructural or microstructural models and macroscopic continuum models [55]. Coupling a particle-level model with a component-level model to simulate sintering holistically remains a challenge for researchers, not only because of the need to define a precise and adequate coupling channel but also because both models need to be matured. The main advantage of the multi-scale computational model is the ability to predict the evolution of the microstructure, which in turn controls the evolution of the material properties through the particle-level model, but at the same time predict the evolution of the shape, size, and deformation of the component, through the component-level model. Here are some application examples [3, 52, 55, 76].

2.5/ Research question and proposal

The literature review conducted in this chapter has revealed the existence of a contextual gap associated with two aspects:

1. The computational modeling of the solid-state sintering process applied to metal extrusion additive manufacturing,

2. A robust computational model based on a multiphysics approach to predict the evolution of microstructure and thermomechanical properties of the material.

In this context, the research question of this thesis can, therefore, be stated as the following:

"Given a green part obtained by MExAM, how to simulate computationally the microstructure evolution (starting from its initial microstructural arrangement) to control the changes in thermomechanical properties during the solid-state sintering process?"

Our proposal to solve this question is to develop a numerical model that is, as realistically as possible, capable of simulating the microstructural and thermomechanical behavior during the pressureless solid-state sintering process. To achieve this goal, this Ph.D. project aims to:

- Identify and mathematically formulate the physical phenomena that govern the solid-state sintering process;
- Characterize the initial microstructure before sintering to obtain the microstructural arrangement (shape, size, and position of grains and pores) that will be the main input data for the model;
- Develop a numerical framework based on a multiphysics approach capable of capturing the microstructural evolution and predicting the thermomechanical behavior during the pressureless solid-state sintering process.
- Apply the model to predict and optimize the microstructural and thermomechanical behavior at the mesoscale level during and after the sintering process, and by the design of experiments (DOE) approach, to obtain the optimal combination of sintering parameters, and finally use this data to simulate the model.

3

Mathematical Formulation of the Solid-State Sintering Process

Contents

3.1/ Introduction

Solid-state Sintering is a complex thermal treatment process that presents several challenges for modeling. These challenges include multi-scale and multi-physical processes, nonlinearity of materials, complex geometry, and boundary conditions, among others [77]. In this chapter, the focus is on a computational model at the mesoscopic level, specifically at the particle level. This proposed model employs a multiphysics approach that couples equations for heat transfer (heat conduction), mass transport (diffusion process), and mechanical effects. This innovative model represents a significant advancement over previous models.

Studying the solid-state sintering process at the microstructural level is crucial for two main reasons:

- To gain a comprehensive understanding of the changes that occur in the microstructure throughout the process and to accurately assess their effect on the mechanical properties of the components, it is crucial to conduct a detailed analysis of the microstructural evolution. This involves closely examining the physical changes at the

mesoscopic level during the process and evaluating how these changes impact the final mechanical properties of the finished components. Engineers and researchers can gain valuable insights to inform the development of more effective and high-performing materials and components by taking a more detailed and in-depth approach to analyzing microstructural evolution.

- To fully understand the behavior of a process, it is important to consider its macrostructural and mechanical effects. However, this study only considers the mechanical effect and does not include the aspect of coupling it with the macrostructural effects. By doing so, we cannot obtain a holistic understanding of the process.

3.2/ Physical fields formulation

To accurately model the solid-state sintering process, it is essential to consider various physical fields as depicted in Figure 3.1. The heat conduction equation helps to evaluate the temporal and spatial behavior of temperature, which plays a significant role in activating the diffusion process. The phase field equation is used to evaluate the variables that characterize the temporal and spatial evolution of the microstructure. Finally, the equilibrium equation helps to analyze the influence of mechanical effects on the microstructure evolution. By considering these physical fields, we can gain valuable insights that can help us better understand and optimize the sintering process.

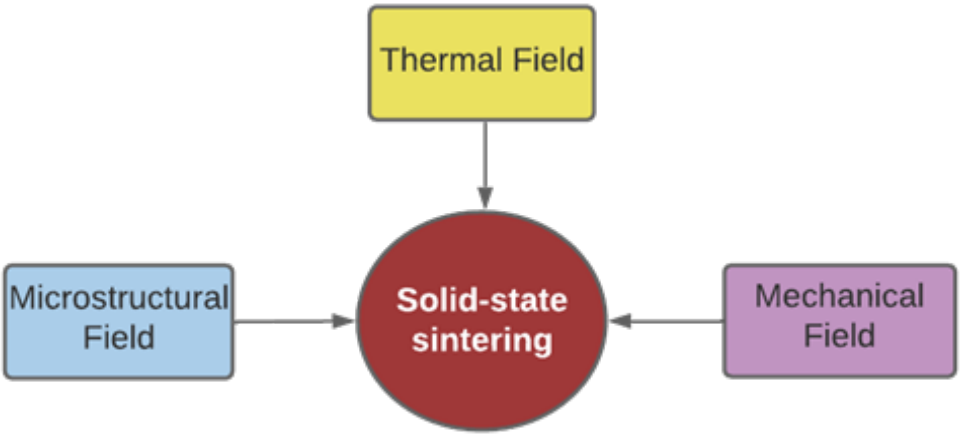

Figure 3.1: Physical phenomena related to solid-state sintering.

3.2.1/ Thermal field formulation

The pressureless solid-state sintering process is a complex mechanism in which thermal loading plays a crucial role. During the sintering process, the thermal loading activates various diffusion mechanisms that are responsible for the morphological changes [8]. These morphological changes can be controlled by adjusting the thermal loading, which makes it an important factor to consider during the sintering process. The diffusion mechanisms activated during sintering depend on the temperature, heating rate, and composition of the sintered materials. Understanding the role of thermal loading in pressureless solid-state sintering is essential to optimize the sintering process and produce high-quality sintered materials.

3.2.1.1/ Governing equation

To obtain the temporal and spatial variations of the temperature during the process, the Fourier law for transient heat conduction in solids [78] is applied, according to Eq. (3.1) below.

$$\rho(T,c)\, c_p(T,c)\, \frac{\partial T}{\partial t} = \nabla \cdot (k(T,c)\, \nabla T) + \dot{q_g} \tag{3.1}$$

This equation is solved by considering that the thermal properties of the material, such as thermal conductivity k and specific heat c_p, including density ρ, vary with temperature and microstructure variables c. On the other hand, it was assumed that the rate of heat generation $\dot{q_g} = \dot{F}$ is caused by the reduction of F, that is, the rate of total free energy per unity of volume and can be calculated from microstructural field [8, 72, 73].

Initial and boundary conditions. The minimum temperature to activate the sintering process depends on the material type and its initial microstructure [79]. In this context, the initial temperature is obtained from the relationship below.

$$T_{ms}(x,y,z,t) = T_0(x,y,z), \qquad (x,y,z) \in \Omega \tag{3.2}$$

Here, the T_{ms} is the minimum sintering temperature, and Ω is the whole domain.

Regarding boundary conditions, the imposed temperature was considered and imposed as described in Eq. (3.3).

$$T = \begin{cases} T_0 + \beta\, T & \text{if } 0 \le t < t_m \\ T_s & \text{if } t_m \le t < t_s \end{cases} \qquad (x,y,z) \in \Gamma \tag{3.3}$$

Where β is the heating rate, t_m is the time to achieve sintering temperature T_s, t_f is the sintering time, and Γ is the total surface of the sintering domain.

3.2.2/ Microstructural field formulation

Based on a thorough evaluation of all the factors discussed in Section 2.4.2, it has been concluded that the Phase Field Method (PFM) is the most effective approach for predicting microstructure evolution. One of the critical strengths of PFM is its ability to accurately capture both qualitative and quantitative microstructure evolution, which makes it a superior choice for this purpose. PFM employs a comprehensive set of order parameters, which includes a conserved order parameter (c) that distinguishes between the porous ($c = 0$) and solid ($c = 1$) phases. Additionally, it utilizes a non-conserved parameter ($\eta = 0$) where p signifies the number of particles or grains that describe individual grains with different crystal orientations, see Figure 3.2 [8, 72]. This feature enables PFM to provide an accurate representation of the microstructure evolution. Another significant advantage of PFM is its ability to be coupled with other physical phenomena, making it a suitable method for modeling the multiphysics process of Solid-State Sintering. This is particularly important because PFM captures all mass transport mechanisms that govern Solid-State Sintering, including surface diffusion, grain boundary diffusion, volume diffusion, and vapor transport. Hence, PFM provides an ideal method for accurately predicting microstructure evolution. Overall, based on the comprehensive analysis of all the

relevant factors, it can be confidently stated that the Phase Field Method (PFM) is the most effective and reliable method for predicting microstructure evolution.

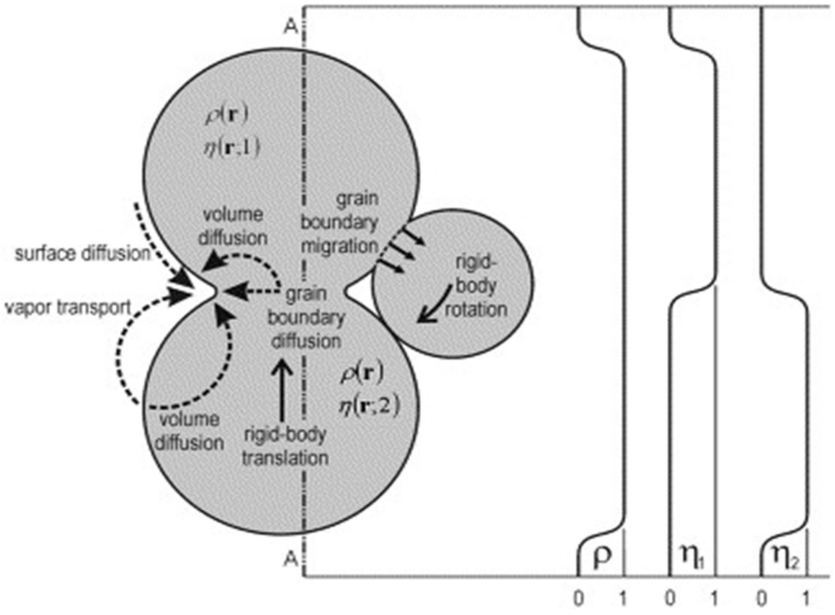

Figure 3.2: Phase-field variables description using the concentration field $c(r) = \rho(r)$ in our formulation, and order parameters ($\eta_i(r) = 0$) for i particles, along the specified cross-section $A - A$ cutting through two particles are plotted (extracted from [2]).

The microstructure evolution is driven by the reduction of the total free energy through diffusion mechanisms and structural relaxation. The total free energy is the sum of the bulk chemical free energy, interfacial energy, elastic energy, visco-plastic energy, and system energy (external energy source), as described in Eq. (2.13) [58, 9]. For the specific process of pressureless solid-state sintering applied to MExAM, the visco-plastic energy and system energy (external energy source) are neglected, and the total free energy is described by Eq. (3.4).

$$F = F_{chem} + F_{int} + F_{el} \tag{3.4}$$

The details of the calculation of the quantities F_{chem}, F_{int}, and F_{el} are presented as follows.

3.2.2.1/ Chemical free energy

The expression of the chemical free energy is derived from [8].

$$F_{chem} = Ac^2(1-c)^2 + B\left[c^2 + 6(1-c)\sum_i {\eta_i}^2 - 4(2-c)\sum_i {\eta_i}^3 + 3\left(\sum_i {\eta_i}^2\right)^2\right] \tag{3.5}$$

Here A and B are bulk energy coefficients, calculated from the grain boundary and surface energy values of the materials (see Eq: (3.6) and Eq. (3.7)) [80].

$$A = \frac{12\gamma_s - 7\gamma_{GB}}{\delta} \tag{3.6}$$

and,

$$B = \frac{\gamma_{GB}}{\delta} \tag{3.7}$$

3.2.2.2/ Interfacial energy

$$F_{int} = \frac{1}{2}k_c|\nabla c|^2 + \sum_i \frac{1}{2}k_\eta|\nabla \eta_i|^2 \tag{3.8}$$

Where γ_s and γ_{GB} are surface and grain boundary energies, respectively, $\delta = \sqrt{\frac{(4k_\eta)}{3B}}$ is the interface width, equal to grain boundary thickness [73, 58].

3.2.2.3/ Elastic energy

$$F_{el} = h(c)f_{el} \tag{3.9}$$

Where $h(c) = 3c^2 - 2c^3$, is the interpolation function, and f_{el} is the elastic energy, computed according to Eq.(3.27).

3.2.2.4/ Governing equations.

Consider that the concentration mass of a component is conserved during the solid-state sintering process. Thus, the equation of continuity in terms of the conservation of mass can be applied to compute the concentration of mass w.r.t position r and time t.

$$\frac{\partial c}{\partial t} + \nabla \cdot (cv) = 0 \tag{3.10}$$

Where ∇ is the gradient operator, and v is the velocity field describing the local instantaneous motion of concentration. If $J = cv$ represents a flux concentration and is a sum of the contributions of diffusion flux J_{dif} and advection flux J_{adv}, as expressed in Eq. (3.11).

$$J = J_{dif} + J_{adv} \tag{3.11}$$

The diffusion flux is computed from Eq. (3.12):

$$J_{dif} = -M\nabla\frac{\delta F}{\delta C} \tag{3.12}$$

Where F is total free energy, Eq. (3.4), and M is Cahn-Hilliard mobility (Eq. (3.23)).

The advection flux describes the mass transport through a motion of a local volume element as a rigid body and can be computed from Eq. (3.13):

$$J_{adv} = cv_{adv} \tag{3.13}$$

The rigid-body motion consists of translation and rotation. Each component of velocity represents each type of motion. The advection velocity v_{adv} is computed from Eq. (3.14):

$$v_{adv} = \sum_i v_{adv_i} = v_{t_i} + v_{r_i} \tag{3.14}$$

Here $v_t = v_t(r, t, i)$ is the velocity field associated with the translation of the i particle,

$$v_{t_i} = \frac{m_t}{Vi} F_i \eta_i \tag{3.15}$$

And $v_r = v_r(r, t, i)$ is the velocity field associated with the rotation of the i particle rotation.

$$v_{r_i} = \frac{m_t}{Vi} T_i \times [r - r_{ci}]\eta_i \tag{3.16}$$

Here, V_i is the volume of the i particle, and m_t and m_r are the translational and rotational mobilities, respectively, r_{ci} is the center of mass of the i particle, and the forces F_i and moments T_i that drive the rigid-body motion are calculated based on the interaction between particles depending on the vacancy diffusion near the GB and are constant over a particle [58], and computed according to Eq. (3.19) and Eq. (3.18) respectively.

$$F_i = \int_V dF_i \tag{3.17}$$

and,

$$T_i = \int_V [r - r_{ci}] \times dF_i \tag{3.18}$$

Where the force density between the particles is the effective local force density acting on the grain boundary of the i particle can be estimated according to Eq. (3.19) [8]:

$$dF_i = \kappa \sum_{j \neq i} (c - c_0)\langle \eta_i \eta_j \rangle [\nabla \eta_i - \nabla \eta_j] d^3 r \tag{3.19}$$

Here κ is a stiffness constant relating the force magnitude to the vacancy oversaturation at grain boundaries, c_0 is a constant that characterizes the equilibrium value of concentration density at grain boundaries, $\nabla \eta_i - \nabla \eta_j$ is the gradient factor for ensuring an action-reaction law between any pair of neighboring particles i and j, and $\langle \eta_i \eta_j \rangle$ which is defined such that:

$$\langle \eta_i \eta_j \rangle = \begin{cases} 1, & \text{if } \langle \eta_i \eta_j \rangle \geq c_{gb} \\ 0, & \text{otherwise} \end{cases} \tag{3.20}$$

where parameter c_{gb} is the threshold concentration value for locating *GBs*.

To make the continuum equations governing the phase field model for solid-state sintering explicit, Eq. (3.11), Eq. (3.12), and Eq. (3.13) were substituted into Eq. (3.10) to obtain equation Eq. (3.21), also called the Cahn–Hilliard equation, which is used to describe the behavior of the conserved phase-field variables and the rigid-body motion was added into the Allen-Cahn equation to obtain Eq. (3.22), which is used to describe the behavior of non-conserved phase-field variables [8].

$$\frac{\partial c}{\partial t} = \nabla \cdot \left(M \nabla \frac{\delta F}{\delta c} - c \sum_i v_{adv_i} \right) \tag{3.21}$$

and,

$$\frac{\partial \eta_i}{\partial t} = -L \frac{\delta F}{\delta \eta_i} - \nabla \cdot [\eta_i v_{adv_i}] \tag{3.22}$$

Where M and L are the mobility coefficients associated with the corresponding order parameters c and η respectively, and are temperature dependent.

The kinetics of the microstructural evolution of the solid-state sintering process is represented by Eq. (3.21 and Eq. (3.22), and their solution predicts the temporal and spatial evolutions of the field variables [8, 72, 58, 69].

Mobility coefficients. M and L are the mobility coefficients associated with Cahn–Hilliard and Allen-Cahn equations, respectively, and are temperature-dependent.

Cahn-Hilliard mobility M [9] is computed from the Eq. (3.23) below:

$$M = \frac{V_m D}{k_B T} \tag{3.23}$$

According to Wang [8], the diffusion coefficients (D), can be calculated as follows:

$$D = D_{vol}\phi(c) + D_{vap}[1 - \phi(c)] + D_{surf}c(1 - c) + D_{gb} \sum_i \sum_{j \neq i} \eta_i \eta_j \tag{3.24}$$

Considering $\phi(c) = c^3(10 - 15c + 6c^2)$, is the interpolation function, $D_i = D_{i0} \exp(-\frac{Q_i}{k_B T})$ are coefficients the atomic diffusion and D_{i0} diffusion pre-factors respectively, the volume diffusion, surface diffusion, vapor diffusion, and grain boundary diffusion. Q_i is the activation energy, k_B is Boltzmann constant, and T is the absolute temperature.

And, Allen-Cahn mobility (L) [73, 58], is computed from the equation below:

$$L = \frac{4}{3} \frac{M_{GB}}{\delta_{GB}} \tag{3.25}$$

Here $M_{GB} = M_{GB0} \exp(-\frac{Q_m}{k_B T})$ is grain boundary (GB) mobility, Q_m is the migration activation energy and δ_{GB} the GB thickness.

Initial and boundary conditions. The initial condition was set up such that within the particles, the value of the phase field variables is one, and everywhere else, they are zero, as expressed below.

$$c, \eta_i = \begin{cases} 1 & \text{inside the particle.} \\ 0 & \text{outside the particle.} \end{cases} \tag{3.26}$$

Two boundary conditions (BC) types can be applied to solve the Phase-Field equation: No-flux BC or Periodic BC. No-flux BC represents an isolated domain without any flow exchange on the boundary from the surroundings. In contrast, periodic BC is applied to ensure the domain's continuity and convert it into an infinite or large domain.

3.2.3/ Mechanical field formulation

For the pressureless solid-state sintering process, the mechanical effect at the microstructural level has been very little studied, which makes it interesting to explore the possible impacts of this field on microstructural evolution. The main mechanical effects that occur during sintering are the elastic and visco-plastic effects. However, for this study, the visco-plastic effect was neglected, and it was considered that all the mechanical transformations in the elastic regime are induced by the gravitational. Kachaturyan proposed the first steps to couple elasticity with PFM [81], then other studies came out using the same approach [9, 82, 83, 84], and recently it has been applied to sintering [58]. To evaluate the impact of the mechanical effect on microstructure evolution, the elastic energy, as a contribution of the mechanical field, has been added to equation 3.4 in the form of free elastic energy, computed according to the equation $F_{el} = h(c)f_{el}$, where f_{el} is the elastic energy expressed according to Eq. (3.27):

$$f_{el} = \frac{1}{2}\int_V C_{ijkl}(\vec{r})\varepsilon_{ij}^{el}\varepsilon_{kl}^{el}d\vec{r} \tag{3.27}$$

Where, $C_{ijkl}(\vec{r})$, are the components of the elastic modulus tensor, that is a function of temperature and Phase-field variables, ε_{ij}^{el} and $\varepsilon_{kl}^{el}$the strains, and i, j, k, l the suffix indices associated with the direction used to identify the components of the stresses and strains.

Governing equation. In the mechanical field, the displacement components are obtained by solving the equilibrium equation (Eq. (3.28)):

$$\nabla \cdot \sigma_{ij} + b_i = 0 \tag{3.28}$$

Here, b_i is the body-force, considered as the gravitational force.

The elastic strain for a linear elastic and isotropic solid during phase transformation is computed from the displacements, expressed as:

$$\varepsilon_{ij}^{el} = \frac{1}{2}\left[\frac{\partial u_i}{\partial x_j} + \frac{\partial u_j}{\partial x_i}\right] \tag{3.29}$$

while the corresponding stresses are computed using Hook's law [85], Eq. (3.30).

$$\sigma_{ij} = C_{ijkl}\varepsilon_{kl}^{el} \tag{3.30}$$

And ε_{kl}^{el} is the elastic strain attributable to mechanical loading (in this study, the gravitational force is considered as mechanical load), and the elastic modulus tensor for isotropic material, C_{ijkl} is expressed as:

$$C_{ijkl} = \frac{E}{2(1+\nu)}\left(\delta_{il}\delta_{jk} + \delta_{ik}\delta_{jl}\right) + \frac{E\nu}{(1+\nu)(1-2\nu)}\delta_{ij}\delta_{kl} \tag{3.31}$$

Here, E and ν are Young's modulus and Poisson's ratio, respectively.

Boundary conditions. The displacement boundary condition was applied to solve the equilibrium equation, as described in Eq. (3.32):

$$u_i = 0 \qquad (x, y, z) \in \Gamma_i \tag{3.32}$$

Where Γ_i is the surface boundary where displacements are zero.

3.3/ Coupling of the physical fields

The modeling of microstructure evolution during the pressureless solid-state sintering process is characterized by multiple physical fields, as referenced in section 3.2, and the evaluation of the effect of these fields on microstructure evolution can be obtained by coupling them. The coupling among thermal, mechanical, and microstructural fields characterizes the physical phenomena of the solid-state sintering process. This coupling is defined by various relationships, such as thermo-mechanical, thermo-phase-field, and mechano-phase-field coupling, as illustrated in Figure 3.3.

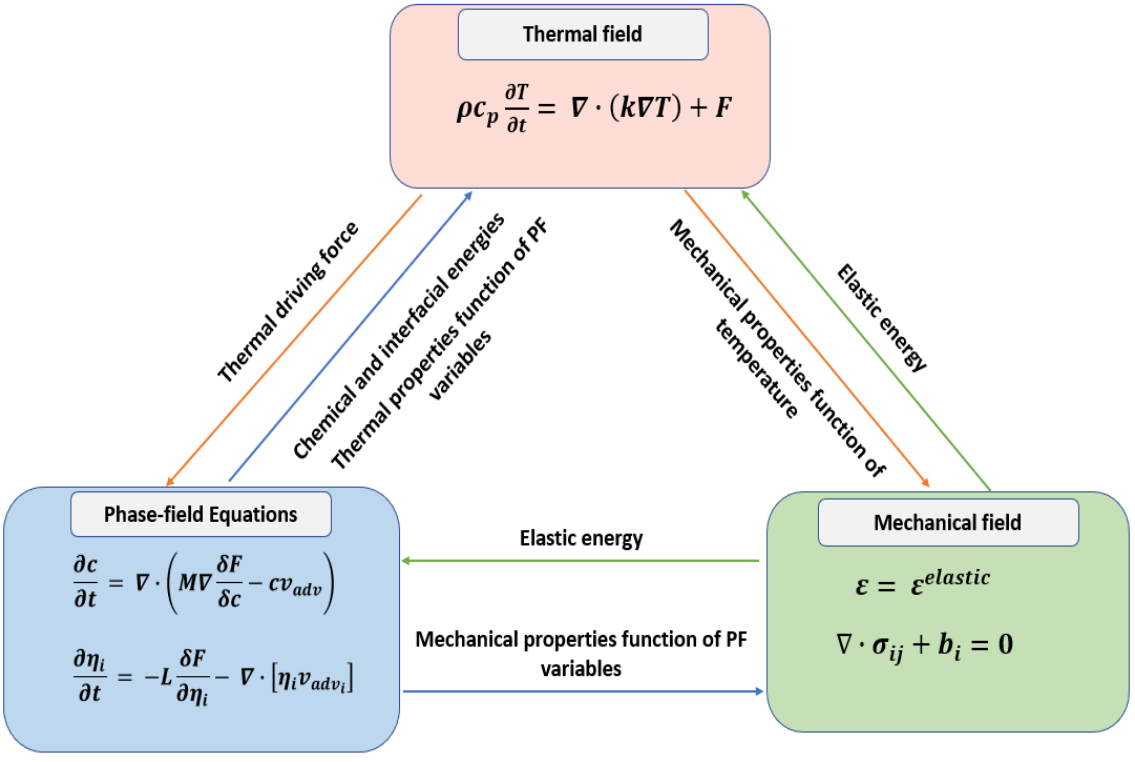

Figure 3.3: Multiphysics couplings among thermal, mechanical, and Phase-field equations.

The behavior of the material can be evaluated by the following expression: $M = h(c)M_{particle} + (1 - h(c)M_{void}$, where $h(c) = 3c^2 - 2c^3$, is the interpolation function, $M_{particle}$ and M_{void} are material properties for particles and voids respectively, and considering that material properties for voids are neglected.

3.3.1/ Thermo-phase-field coupling

The spatial and temporal distribution of temperature leads to the activation of the microstructural field through the mechanisms of mass transport (diffusion process), which are represented by the Cahn-Hilliard (Eq. (3.23)) and Allen-Cahn mobilities Eq. (3.25)). On the other hand, Phase-field variables influence the thermal field in two ways: First, they cause the addition of chemical-free energy and interfacial energy on the thermal field, and second, thermal properties, such as density, thermal conductivity, and specific heat, become dependent on phase field variables.

In this study, the relationships considered between these two fields are as follows:

1. From the thermal field to the Phase-field equations, the temperature distribution is applied to compute the Cahn-Hillard and Allen-Cahn mobility, according to Eq. (3.23) and (3.25).
2. From the microstructural to the thermal field, the influence of the chemical free and interfacial energies on the thermal field was neglected, and only the variation of the thermal properties with respect to the phase field variables was considered, according to Eqs. (3.33), (3.34) and (3.35) [58].

For the thermal field, the following variations of thermal properties are considered:

Density:

$$\rho(T, c) = \rho(T)h(c) \tag{3.33}$$

Specific heat:

$$c_p(T, c) = c_p(T)h(c) \tag{3.34}$$

Thermal conductivity:

$$k(T, c) = k(T)h(c) \tag{3.35}$$

With respect to temperature and conserved parameters.

3.3.2/ Mechano-Phase-field coupling

The microstructure evolution occurs so that the mechanical properties become dependent on the PF variables, while the elastic energy resulting from the mechanical transformations is added to the equations that govern the microstructural field. Mechanical properties, such as:

Young's modulus:

$$E(c) = Eh(c) \tag{3.36}$$

And Poisson's ratio:

$$\nu(c) = \nu h(c) \tag{3.37}$$

Vary with respect to PF variables.

3.3.3/ Thermo-Mechanical coupling

Since the sintering process takes place at high temperatures, this leads to variations in the mechanical properties of the material, in addition to the induction of thermal stresses. On the other hand, the elastic energy generated during the mechanical transformations, in reverse, influences the thermal field.

Thus, for the mechanical field, all mechanical properties:

Young's modulus:

$$E(T, c) = E(T)h(c) \tag{3.38}$$

And Poisson's ratio:

$$\nu(T, c) = \nu(T)h(c) \tag{3.39}$$

Become functions of temperature and conserved parameters.

3.3.4/ Summary of the hypotheses

Modeling of the pressureless solid-state sintering process was done under the following assumptions:

- Except for thermal loads, all other external loads, such as pressure or force, have been neglected;
- The total free energy depends only on the chemical free energy, the interfacial free energy, and the elastic free energy;
- The effect of total free energy on the thermal field was neglected since its value is very low compared to the amount of energy coming from the sintering environment.

3.4/ Conclusion

In this chapter, a detailed mathematical model has been presented for studying pressureless solid-state sintering at the microstructural level. The study involves a multiphysics coupling approach that considers the heat conduction equation, Phase-Field equations, and mechanical equilibrium equation to model the evolution of microstructure during sintering accurately. The model considers several hypotheses for solving the problem. The

chapter also provides a comprehensive description of the mathematical relations that establish the links among the physical fields involved in the sintering process. This includes detailed explanations of the assumptions made for solving the problem. The study provides insights into the complex physical phenomena occurring during the sintering process and can be useful for further research in the field.

To effectively handle the complexity of the mathematical equations obtained, it is crucial to identify and carefully apply the most appropriate numerical techniques that best suit the problem at hand. Therefore, the upcoming chapter has been specifically developed to provide comprehensive insight into this context to ensure that the most efficient and effective numerical techniques are employed to address the mathematical challenges posed.

4

Numerical Framework

Contents

4.1/ Introduction

Applying numerical methods has made it possible to practically and precisely solve many problems in engineering and science. The selection of the appropriate method depends on the type of problem. Finite difference method (FDM) [8, 65, 72, 86], finite element method (FEM) [58, 73, 87, 88, 89], and Discrete element method (DEM) [59, 62, 64] are widely applied as numeric techniques to model the sintering process. However, for this study, we used FEM since this method is more suitable for problems consisting of solving PFM coupled with other multiphysics phenomena, such as thermal and mechanical. Therefore, this chapter presents how the multiphysics coupling equations that govern the pressureless solid-state sintering process can be numerically implemented at the microstructural level

using FEM. Likewise, in this chapter, the implemented numerical framework is validated by comparison with the simple (two-particle) models already published.

Some tests have been carried out to understand and test the capability and robustness of the model to simulate a pressureless solid-state sintering process at the microstructure level. First, the simple (two-particle) model is simulated with and without the effect of the mechanic field to evaluate the impact of this field, and second; different scenarios are created (see Tables 4.3 and 4.4) to assess the impact of particle size and the impact of sintering temperature. The main goal is to determine the impact of these two primary input data on microstructural evolution in terms of grain growth and diffusion, porosity evolution, and time to achieve microstructural equilibrium.

4.2/ Finite element implementation

In the previous chapter, we introduced the equations governing the pressureless solid-state sintering process. These equations are represented by partial differential equations. Additionally, we learned about the corresponding boundary and initial conditions that must be satisfied for the process to occur. Given all this information, the FEM (finite element method) will be implemented as the primary numerical technique to solve this problem. Figure 4.1 provides a detailed illustration of the main general steps involved in implementing the FEM.

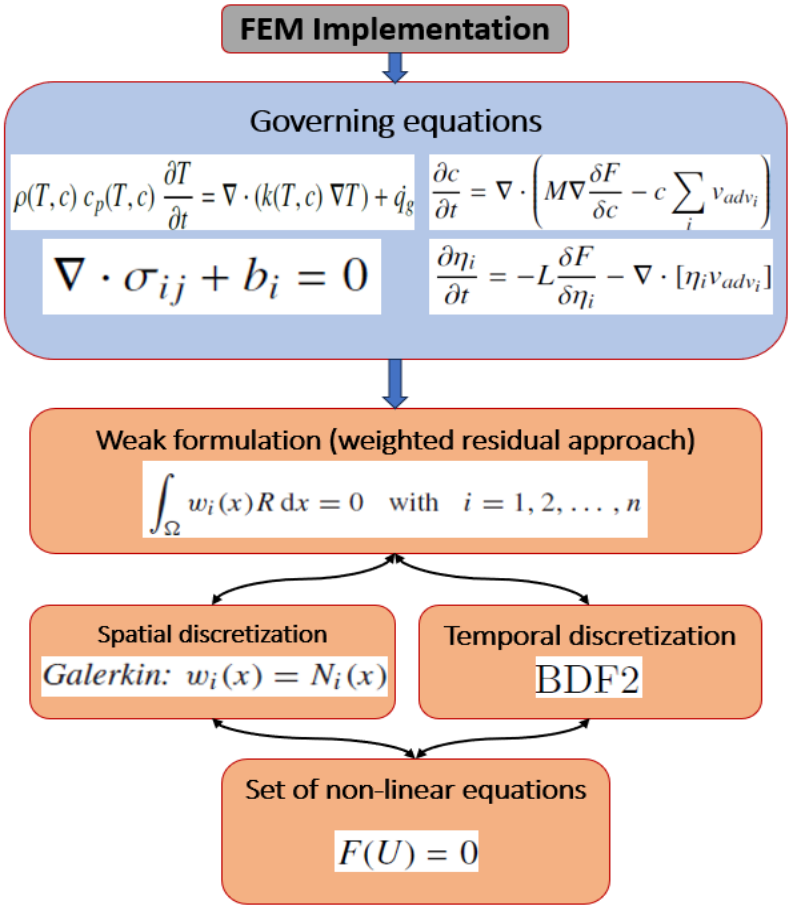

Figure 4.1: FEM implementation flowchart.

4.2.1/ Weak formulation

The FEM implementation requires reformulating the problem by introducing the weak form of the differential equations to obtain accurate approximate solutions. To set up the FEM discretization, the residual equations of governing equations in the weak form are built-up, applying the weighted integral residual approach and using test function ψ, and applying the divergence theorem. Thus, this yields the following equations:

1. Considering Eq. (3.1) and applying BC Eq. (3.3), the weak form of heat conduction is Eq. (4.1):

$$\int_\Omega \rho c_p \frac{\partial T}{\partial t}\psi^T \, d\Omega + \int_\Omega k\nabla T \nabla \psi^T \, d\Omega = \int_\Gamma k\nabla T \psi^T \cdot \vec{n} \, d\Gamma \tag{4.1}$$

2. Considering Eq. (3.28), (3.30), and (3.31) and applying the BC Eq. (3.32), the weak form of the mechanical equation is Eq. (4.2):

$$\int_\Omega C_{ijkl}\nabla u \nabla \psi^u \, d\Omega = \int_\Omega C_{ijkl}\delta_{kl}\alpha \Delta T \nabla \psi^u \, d\Omega + \int_\Omega \psi^u b_i \, d\Omega \tag{4.2}$$

3. The split version of the fourth-order Cahn-Hillard (CH) Eq. (3.21) is applied to get the Eq. (4.3) and Eq. (4.4) [58], [73].

$$\frac{\partial c}{\partial t} = \nabla \cdot \left(M\nabla \mu - c \sum_i v_{adv_i} \right) \tag{4.3}$$

$$\mu = \frac{\delta F}{\delta c} - k_c \nabla^2 c \tag{4.4}$$

So, for Phase-Field equations, the weak form of the Cahn-Hillard equation is Eq. (4.5) and Eq. (4.6)

$$\int_\Omega \frac{\partial c}{\partial t}\psi^c \, d\Omega - \int_\Omega M\nabla\mu\nabla\psi^c \, d\Omega + \int_\Omega \nabla \cdot \left(c \sum_i v_{adv_i} \right) \psi^c \, d\Omega = -\int_\Gamma M\nabla\mu\nabla\psi^c \cdot \vec{n} \, d\Gamma \tag{4.5}$$

and

$$\int_\Omega \mu\psi^\mu \, d\Omega - \int_\Omega \frac{\delta F}{\delta c}\psi^\mu \, d\Omega - \int_\Omega k_c \nabla c \nabla \psi^\mu \, d\Omega = -\int_\Gamma k_c \nabla c \psi^\mu \cdot \vec{n} \, d\Gamma \tag{4.6}$$

4. Considering Eq. (3.22), the weak form of the Allen-Cahn equation is Eq. (4.7):

$$\int_\Omega \frac{\partial \eta}{\partial t}\psi^\eta \, d\Omega + L\int_\Omega \frac{\delta F}{\delta \eta_i}\psi^\eta - L\int_\Omega k_{\eta_i}\nabla\eta_i\nabla\psi^\eta \, d\Omega + \int_\Omega \nabla\cdot\eta_i v_{adv_i}\psi^\eta \, d\Omega = -L\int_\Gamma k_{\eta_i}\nabla\eta_i\psi^\eta \cdot \vec{n} \, d\Gamma \tag{4.7}$$

where ψ^T, ψ^μ, ψ^c, ψ^η, and ψ^u are correspondent test functions associate to field variables T, μ, c, η_i and u respectively, and $\vec{n}$ is the normal vector to the boundary Γ of the domain.

4.2.2/ Spatial and temporal discretization

These equations need to solve two types of discretization: discretization in space and time.

4.2.2.1/ Spatial discretization

The field variables are spatially discretized according to the finite element approach, and applying the following approximation:

$$T = N_T^I T^I, \quad \mu = N_\mu^I \mu^I, \quad c = N_c^I c^I, \quad \eta_i = N_\eta^I \eta_i^I, \quad and \quad u = N_u^I u^I \tag{4.8}$$

here T^I, μ^I, c^I, η_i^I, and u^I are the nodal value of field variables T, μ, c, η_i and u respectively, and N_T^I, N_μ^I, N_c^I, N_η^I, and N_u^I are the correspondent shape functions, while the finite element approximations of the gradient of the field variable are expressed in Eq. (4.9).

$$\nabla T = B_T^I T^I \quad \nabla \mu = B_\mu^I \mu^I, \quad \nabla c = B_c^I c^I, \quad \nabla \eta_i = B_\eta^I \eta_i^I, \quad and \quad \nabla u = B_u^I u^I \tag{4.9}$$

where B^I is the derivative matrix of N^I.

The standard Galerkin approach has been selected as the approximation method for weight residual, as shown in Eq. (4.10).

$$\psi^T = N_T^I, \quad \psi^\mu = N_\mu^I, \quad \psi^c = N_c^I, \quad \psi_i^\eta = N_\eta^I, \quad and \quad \psi^u = N_u^I \tag{4.10}$$

Substituting the Eq. (4.8), Eq. (4.9), and Eq. (4.10) into Eq. (4.1), Eq. (4.2), Eq. (4.5), Eq. (4.6), and Eq. (4.7), applying some algebraic operations and rearranging them gives Eqs. (4.11), (4.12), (4.13), (4.14) and (4.15), representing the discretized nonlinear equations system.

$$F_T(U) = \int_\Omega \rho c_p N_T^I N_T^J \frac{\partial T^I}{\partial t}\, d\Omega + \int_\Omega k B_T^I B_T^J T^I\, d\Omega - \int_\Gamma k B_T^I N_T^J \cdot \vec{n}\, d\Gamma \tag{4.11}$$

$$F_u(U) = \int_\Omega C_{ijkl} B_u^I B_u^J u^I\, d\Omega - \int_\Omega N_u^I b_i\, d\Omega \tag{4.12}$$

$$F_c(U) = \int_\Omega N_c^I N_c^J \frac{\partial c^I}{\partial t}\, d\Omega - \int_\Omega M B_\mu^I B_c^J \mu^I\, d\Omega + \int_\Omega \nabla \cdot \left(N_c^I c^I \sum_i v_{adv_i} \right) N_c^J\, d\Omega \int_\Gamma M B_c^I \mu^I B_c^J \cdot \vec{n}\, d\Gamma \tag{4.13}$$

$$F_\mu(U) = \int_\Omega N_\mu^I \mu^I N_\mu^J\, d\Omega - \int_\Omega \frac{\delta F}{\delta c} N_\mu^I\, d\Omega - \int_\Omega k_c B_c^I c^I B_c^J\, d\Omega \int_\Gamma + k_c B_c^I c^I N_\mu^J \cdot \vec{n}\, d\Gamma \tag{4.14}$$

$$F_\eta(U) = \int_\Omega N_\eta^I N_\eta^J \frac{\partial \eta_i^I}{\partial t}\, d\Omega + L \int_\Omega \frac{\delta F}{\delta \eta_i} N_\eta^I - L \int_\Omega k_{\eta_i} B_\eta^I B_\eta^J \eta_i^I\, d\Omega + \int_\Omega \nabla \cdot \left(N_\eta^I \eta_i^I v_{adv_i} \right) N_\eta^J\, d\Omega + L \int_\Gamma k_{\eta_i} B_\eta^I \eta_i^I N_\eta^J \cdot \vec{n}\, d\Gamma \tag{4.15}$$

where $F = \{F_T, F_u, F_\mu, F_c, F_\eta\}$ is the nonlinear residual function and $U = \{T, u, \mu, c, \eta\}^T$.

4.2.2.2/ Time integration

The second-order backward differentiation formula (BDF2) is applied as the time integration scheme; for instance, given a variable $U(t)$, $\partial U/\partial t$ will be discretized according to Eq. (4.16). However, whenever another scheme is used, it will be mentioned.

$$\frac{\partial U}{\partial t} = \frac{3U^{n+1} - 4U^n + U^{n-1}}{2\Delta t} \tag{4.16}$$

4.3/ Solver techniques

4.3.1/ Non-linear resolution

For solving the nonlinear system of Eqs. (4.11), (4.12), (4.13), (4.14) and (4.15), representing by (Eq. (4.17)), the classical Newton method can be applied to solve it iteratively.

$$F(U) = 0 \tag{4.17}$$

Applying the first-order Taylor expansion about U^k yields a strict Newton method, formed by linear Eq. (4.18),

$$\mathbb{J}(U^k)\delta U^k = -F(U^k) \tag{4.18}$$

and updated by linear Eq. (4.19)

$$U^{k+1} = U^k + \delta U^k, \quad k = 0, 1, ... \tag{4.19}$$

The Jacobian matrix J^k is computed according to Eq. (4.20), where i, j are the elements of the Jacobian matrix for the k^{th} Newton iteration. Eq. (4.18) is solved using a Krylov method [90].

$$\mathbb{J}^k_{i,j} = \frac{\partial F_i(U^k)}{\partial U^k_j} \tag{4.20}$$

However, the classical Newton method may not be the most appropriate method since for multiphysics coupling problems and large systems, it is computationally costly and difficult to form the Jacobian matrix Eq. (4.20) (at each grid point) and invert it, and it is usually ill-conditioned and error-prone [91, 92, 93]. To overcome these constraints, the Jacobian-free Newton-Krylov (JFNK) method was applied.

4.3.2/ Preconditioned Jacobian-free Newton-Krylov method

Despite its fast convergence, Newton's classical method is severely affected by the formation and inversion cost of the Jacobian at each iteration, and the Generalized Minimum Residual (GMRES), a class of Krylov subspace method, is proposed to overcome the high inversion cost issue [94]. Still, a new Jacobian is formed in each iteration, which can be overcome by applying the JFNK method [92, 94], which is used to alleviate the explicit

formation of the Jacobian matrix [95]. Some advantages of the JFNK method over the traditional implementation of Newton methods are [93, 94]:

- Significant reduction in computational operation and storage;
- For a tight convergence tolerance, there is no splitting or linearization error;
- The algorithm provides a clean way to include other nonlinear phenomena;

Since the Krylov method requires the action of the Jacobian only to form the matrix-vector product ($\mathbb{J}v$), the JFNK method takes advantage of this to approximate the matrix-vector product by the finite difference of $F(U)$, according to Eq. (4.21).

$$\mathbb{J}v \approx \frac{F(U + \epsilon v) - F(U)}{\epsilon} \tag{4.21}$$

Here v is a Krylov vector and ϵ is a small perturbation. Thus, the Jacobian formation is avoided, which makes the success of the JFNK method strongly dependent only on the efficiency of GMRES (Krylov method), which can be improved by applying preconditioners [92, 90].

The application of preconditioning on the JFNK method aims to efficiently cluster the eigenvalues of the iteration matrix which consequently reduces the required number of GMRES (Krylov) iterations [93]. In this study, we use the right-preconditioned system, which consists of introducing the matrix $\mathbb{M}$ and $\mathbb{M}^{-1}$ into Eq. (4.18) as expressed in Eq. (4.22).

$$\left(\mathbb{J}\mathbb{M}^{-1}\right)\left(\mathbb{M}\delta U^k\right) = -F(U^k) \tag{4.22}$$

where $\mathbb{M}$ and $\mathbb{M}^{-1}$ represent the preconditioning matrix and its inverse matrix respectively.

In this context, the approximation of the matrix-vector product, which represents the right-preconditioned version of Eq. (4.21) is:

$$\mathbb{J}\mathbb{M}^{-1}v \approx \frac{F\left(U + \epsilon\mathbb{M}^{-1}v\right) - F(U)}{\epsilon} \tag{4.23}$$

Thus, this operation is done in two steps:

1. Preconditioning: Solve (approximately) $y = \mathbb{M}^{-1}v$.
2. Perform matrix-free product $\mathbb{J}\mathbb{M}^{-1}v \approx (F(U + \epsilon y) - F(U))/\epsilon$.

Only the matrix elements required for the action of $\mathbb{M}^{-1}$ are formed, and there are two primary choices to be made by the user of a Jacobian-free Newton–Krylov method, according to [92]:

1. What linearization should be used to form the matrices required in $\mathbb{M}^{-1}$?
2. What linear iterative method should be used for $y = \mathbb{M}^{-1}v$?

Many preconditioning approaches can be applied to overcome these issues, and they are broadly classified into two groups: Matrix-based and Physics-based (PDEs-based) preconditioning [94]. In Matrix-based preconditioning, eigenvalues are clustered to make them easily solvable by multiplying the original system with some suitable factorization matrix such as LU, ILU, SOR, or SSOR. However, a matrix of a real system is usually not well structured, which makes the matrix-based approach less effective since it does not include the physics governing the problem. To overcome these issues, physics-based preconditioning is preferred. In this approach, the preconditioner is developed by considering the nature of PDEs, directly targeting the complex behavior of physics behind the problem [92, 94]. For more details about preconditioning approaches see [92, 96, 97, 98]. In this study, unless mentioned otherwise, we use Physics-based preconditioning (PBP), which generally, is preferred over matrix-based preconditioning for problem-specific cases.

4.3.3/ Physics-based preconditioning (PBP)

An efficient PBP can be obtained by applying the operator splitting approach, which consists of reducing the Jacobian matrix to a lower triangular form by (i) linearization of the nonlinear terms and (ii) decoupling the unknowns inspired by classical operator splitting approaches [98].

From the discretized equations Eqs. (4.11), (4.12), (4.13), (4.14) and (4.15), the Jacobian matrix (Eq. (4.24)) is formed, but it is never explicitly formed in the code.

$$\mathbb{J} = \begin{pmatrix} \mathbb{J}_{T,T} & \mathbb{J}_{T,u} & \mathbb{J}_{T,\mu} & \mathbb{J}_{T,c} & \mathbb{J}_{T,\eta_i} \\ \mathbb{J}_{u,T} & \mathbb{J}_{u,u} & \mathbb{J}_{u,\mu} & \mathbb{J}_{u,c} & \mathbb{J}_{u,\eta_i} \\ \mathbb{J}_{\mu,T} & \mathbb{J}_{\mu,u} & \mathbb{J}_{\mu,\mu} & \mathbb{J}_{\mu,c} & \mathbb{J}_{\mu,\eta_i} \\ \mathbb{J}_{c,T} & \mathbb{J}_{c,u} & \mathbb{J}_{c,\mu} & \mathbb{J}_{c,c} & \mathbb{J}_{c,\eta_i} \\ \mathbb{J}_{\eta_i,T} & \mathbb{J}_{\eta_i,u} & \mathbb{J}_{\eta_i,\mu} & \mathbb{J}_{\eta_i,c} & \mathbb{J}_{\eta_i,\eta_i} \end{pmatrix} \tag{4.24}$$

In the following, the following steps are taken for an efficient formation of the preconditioned matrix M (lower-triangular matrix):

(Step 1) To simplify the Jacobian matrix (Eq. (4.24) by linearization of the material properties. For example, the Jacobian elements for the heat conduction operator in the heat conduction equation, specifically the second term of the right side in Eq. (4.11), is:

$$\mathbb{J}^k_{T_i,T_j} = \frac{\partial F_{T_i}(U^k)}{\partial T^k_j} = \int_\Omega B^I_T B^J_T \frac{\partial k^k}{\partial T^k_j} T^I \, d\Omega + \int_\Omega k^k B^I_T B^J_T \, d\Omega \tag{4.25}$$

Simplifying the Eq. (4.25), we get the preconditioning matrix $\mathbb{M}^k_{T_i,T_j}$, which is:

$$\mathbb{M}^k_{T_i,T_j} = \int_\Omega k^k B^I_T B^J_T \, d\Omega \tag{4.26}$$

We are applying the same approach to get the off-diagonal Jacobian between T and u.

$$\mathbb{J}^k_{T_i,u_j} = \frac{\partial F_{T_i}(U^k)}{\partial u^k_j} = \int_\Omega B^I_T B^J_T \frac{\partial k^k}{\partial u^k_j} T^I \, d\Omega \tag{4.27}$$

From the Eq. (4.27), we get the preconditioning matrix $\mathbb{M}^k_{T_i,u_j}$, which is:

$$\mathbb{M}^k_{T_i,u_j} = \int_\Omega B^I_T B^J_T \frac{\partial k^k}{\partial u^k_j} T^I \, d\Omega \tag{4.28}$$

Applying a similar approach to the linearization of the other material properties, we get the following matrix:

$$\mathbb{M} = \begin{pmatrix} \mathbb{M}_{T,T} & \mathbb{M}_{T,u} & \mathbb{M}_{T,\mu} & \mathbb{M}_{T,c} & \mathbb{M}_{T,\eta_i} \\ \mathbb{M}_{u,T} & \mathbb{M}_{u,u} & \mathbb{M}_{u,\mu} & \mathbb{M}_{u,c} & \mathbb{M}_{u,\eta_i} \\ \mathbb{M}_{\mu,T} & \mathbb{M}_{\mu,u} & \mathbb{M}_{\mu,\mu} & \mathbb{M}_{\mu,c} & \mathbb{M}_{\mu,\eta_i} \\ \mathbb{M}_{c,T} & \mathbb{M}_{c,u} & \mathbb{M}_{c,\mu} & \mathbb{M}_{c,c} & \mathbb{M}_{c,\eta_i} \\ \mathbb{M}_{\eta_i,T} & \mathbb{M}_{\eta_i,u} & \mathbb{M}_{\eta_i,\mu} & \mathbb{M}_{\eta_i,c} & \mathbb{M}_{\eta_i,\eta_i} \end{pmatrix} \tag{4.29}$$

(Step 2) To evaluate the dependence of the material properties on each variable (T, u, μ, c, η_i). For example, thermal conductivity $k(T, c)$, is not function of u, μ, nor of η_i, so all off-diagonal Jacobian between T and each of these variables can be neglected. Applying the same approach to evaluate the material properties of each residual equation w.r.t the other variables, the matrix is:

$$\mathbb{M} = \begin{pmatrix} \mathbb{M}_{T,T} & 0 & 0 & \mathbb{M}_{T,c} & 0 \\ \mathbb{M}_{u,T} & \mathbb{M}_{u,u} & 0 & \mathbb{M}_{u,c} & 0 \\ 0 & 0 & \mathbb{M}_{\mu,\mu} & 0 & 0 \\ \mathbb{M}_{c,T} & 0 & \mathbb{M}_{c,\mu} & \mathbb{M}_{c,c} & \mathbb{M}_{c,\eta_i} \\ \mathbb{M}_{\eta_i,T} & 0 & 0 & 0 & \mathbb{M}_{\eta_i,\eta_i} \end{pmatrix} \tag{4.30}$$

(Step 3) To eliminate specific off-diagonal blocks by evaluating time scale and weaker couplings. For example, the time scales of Temperature T and Displacement u are relatively slow compared to conserved parameter c, so $\mathbb{M}_{T,c}$ and $\mathbb{M}_{u,c}$ can be ignored, and the coupling between c and η_i in the material property matrix operator $\mathbb{M}_{c,\eta_i}$ can be considered weaker, so it can also be ignored. The matrix is:

$$\mathbb{M} = \begin{pmatrix} \mathbb{M}_{T,T} & 0 & 0 & 0 & 0 \\ \mathbb{M}_{u,T} & \mathbb{M}_{u,u} & 0 & 0 & 0 \\ 0 & 0 & \mathbb{M}_{\mu,\mu} & 0 & 0 \\ \mathbb{M}_{c,T} & 0 & \mathbb{M}_{c,\mu} & \mathbb{M}_{c,c} & 0 \\ \mathbb{M}_{\eta_i,T} & 0 & 0 & 0 & \mathbb{M}_{\eta_i,\eta_i} \end{pmatrix} \tag{4.31}$$

Now, the preconditioning of the process, which consists of approximately solving Eq. (4.32) is done by following the steps below:

$$\begin{pmatrix} \mathbb{M}_{T,T} & 0 & 0 & 0 & 0 \\ \mathbb{M}_{u,T} & \mathbb{M}_{u,u} & 0 & 0 & 0 \\ 0 & 0 & \mathbb{M}_{\mu,\mu} & 0 & 0 \\ \mathbb{M}_{c,T} & 0 & \mathbb{M}_{c,\mu} & \mathbb{M}_{c,c} & 0 \\ \mathbb{M}_{\eta_i,T} & 0 & 0 & 0 & \mathbb{M}_{\eta_i,\eta_i} \end{pmatrix} \begin{pmatrix} \delta T \\ \delta u \\ \delta \mu \\ \delta c \\ \delta \eta_i \end{pmatrix} = - \begin{pmatrix} F_T \\ F_u \\ F_\mu \\ F_c \\ F_{\eta_i} \end{pmatrix} \tag{4.32}$$

1. $\mathbb{M}_{T,T}\delta T = -F_T$
2. $\mathbb{M}_{u,u}\delta u = -\mathbb{M}_{u,T} - F_u$

3. $\mathbb{M}_{\mu,\mu}\delta\mu = -F_\mu$

4. $\mathbb{M}_{c,c}\delta c = -\mathbb{M}_{c,T} - \mathbb{M}_{c,\mu} - F_c$

5. $\mathbb{M}_{\eta_i,\eta_i}\delta\eta_i = -\mathbb{M}_{\eta_i,T} - F_\eta$ for $i = 1.2.3...p$ (particles).

And the algorithm 1 summarizes the main steps applied to solve the Eq; (4.32).

Algorithm 1 Numerical implementation algorithm

Require: Initialization of Material properties, ICs, and BCs.
for $i \leftarrow 1, n$ **do**
  for $k \leftarrow 1, m$ **do**
    compute Thermal field Eq. (4.11).
    then compute Mechanical field Eq. (4.11), (4.12), (4.14), (4.13) and (4.15).
    then compute Phase-Field Eqs. (4.14), (4.13) and (4.15) respectively.
  end for
end for
update Material properties (Thermal and mechanical).
Prepare for the next time step iteration.

4.3.4/ Implementing in the MOOSE software

MOOSE (Multiphysics Object-Oriented Simulation Environment) is a powerful open-source software and parallel finite element framework allowing efficient and accurate simulations of complex physical systems. It is designed to handle various applications, including solid and fluid mechanics, electromagnetics, and multiphysics simulations [99]. The decision to use MOOSE as the basis for developing a numerical framework was motivated by several factors. Firstly, its modular and object-oriented design makes it highly flexible and adaptable to different simulation needs. Additionally, MOOSE provides advanced meshing, solution visualization, and post-processing tools, which are crucial for producing reliable and insightful results. Moreover, MOOSE has a large and active user community, which means ample documentation, support, and resources are available. This facilitates the development process and ensures that the resulting framework is robust and reliable. In summary, MOOSE is an ideal platform for developing a numerical framework due to its versatility, advanced features, and robust user community. So, we have decided to develop a numerical framework based on MOOSE software because of its capability and because of the following aspects:

- The pressureless solid-state sintering process, at the microstructural level, is a multi-physical phenomenon, as mentioned in Chapter 3, To simulate and understand the complex multi-physical behavior of sintering, researchers have developed various computational tools. MOOSE (Multi-physics Object-Oriented Simulation Environment) has proven to be a robust and reliable solver for multiphysics problems, as demonstrated in [99].
- Unlike other software, MOOSE has a specific module (`Phase_Field_Module` [88, 100]) for solving Phase-Field problems and can be applied to SSS (with appropriate changes).

- ❖ MOOSE is a powerful parallel computational framework for solving coupled systems of nonlinear equations [101].

Since our model is a thermo-mechano-phase-field model, it is activated the MOOSE `Heat_Conduction_Module`, `Tensor_Mechanics_Module`, and `Phase_Field_Module`. The preparation of an input file in MOOSE depends on the problem and can consist of several parts. Still, for our model, the most relevant parts (block) (not limited to these) that allowed the specific implementation of the model are: `Variables`, `Kernels`, `BCs`, `Materials`, `Executioner` and `Preconditioning`.

In the variables block, special attention should be given to the η variable, which is implemented by activating the PolycrystalVariables object accompanied by the number of particle definition (i = 1.2.3...p). The multiphysics coupling occurs in the kernel's block, in which case all the volume integral terms of Eqs. (4.11), (4.12), (4.13), (4.14) and (4.15) are implemented as objects in this block, while separately the surface integral terms are implemented in the BCs block. Some aspects must be considered such as the activation of the RigidBodyMultiKernel object, the action for applying Eq. (4.15) and SingleGrainRigidBodyMotion to grains, the MultiGrainRigidBodyMotion object, which adds rigid body motion to grains for Eq. (4.13), and the PolycrystalElasticDrivingForce object, the action that adds the elastic driving force (mechanical field) for each order parameter (η).

The implementation of blocks `Executioner` and `Preconditioning` is extremely important, as it allows the Eq. (4.32) to be solved by selecting the appropriate numerical techniques for the problem.

4.4/ Theoretical validation

The theoretical validation of the model was carried out by performing two tests with data taken from the literature based on the classical **two-particle model**. In the first test, particles of equal diameters were used, and the results were compared with the findings reported in Biswas et al. [58]. The second test was conducted with particles of unequal diameters, and the results were compared with the findings reported in Chockalingam et al. [73]. The obtained results were then illustrated in the figures below, which show that they correspond to the results that they have reported. These findings provide a comprehensive validation of the model and confirm its accuracy.

4.4.1/ Test I - Equal size

In this simulation test, the study focused on two particles of equal diameter, measuring 15 µm each. These particles were embedded in a 2D simulation domain with a total dimension of 40 x 20 µm. The simulation setup included an initial minimum contact point between the particles. The simulation's red zone represents the particles' solid part, while the blue zone represents the voids. The interface between two adjacent particles was called the neck or GB in this simulation. The neck, or GB, is where the two particles come into contact. The interface between the particle's solid part and the void, also known as porosity, represents the interface between the phases. The simulation conditions and the input data[1] for the test were adopted as set out in [58].

[1] Non-dimensionalized data taken from Table 2 in [58].

The test was carried out for three scenarios (Case I, II, and III), which aimed to assess the impact of Chemical Free Energy on neck size by changing the gradient energy coefficients (A (Eq. 3.6) and B (Eq.3.7)). It should be noted that the reduction of Chemical, Interfacial, and Elastic free energies is considered the driving force behind the microstructure evolution. Case I represents the reference case and is illustrated in Figure 4.2, which indicates the non-conserved phase-field variable η evolution of two particles.

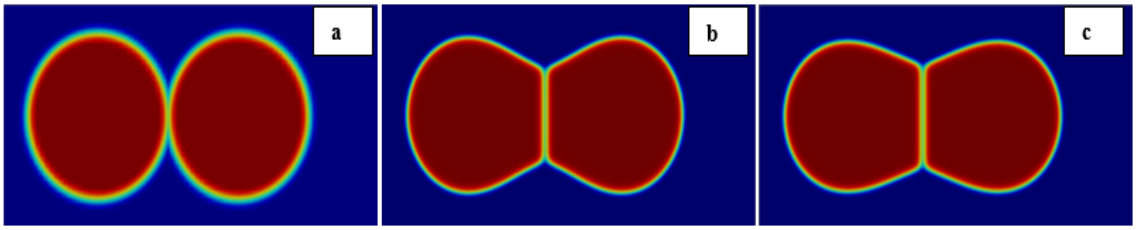

Figure 4.2: The evolution of non-conserved phase-field variable η of two particles. For equal size, case I (a:t = 0, b:t = 50 s and c:t = 100 s)

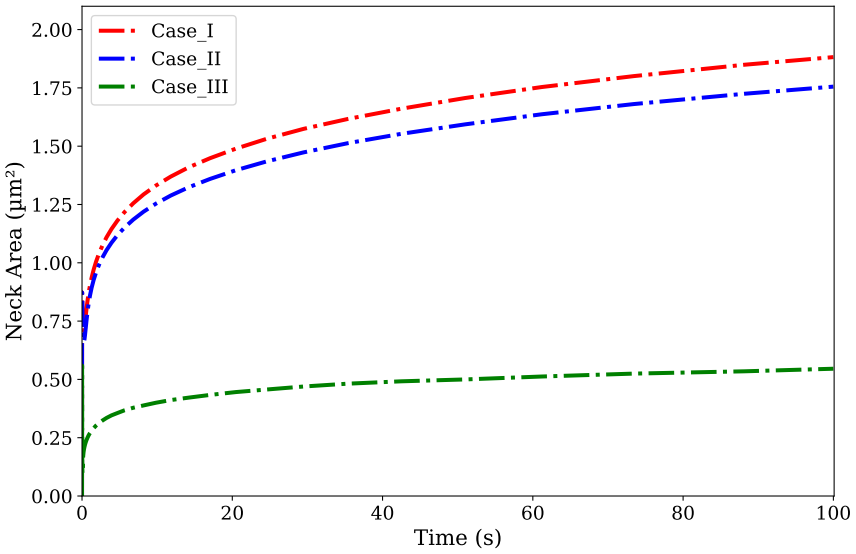

Figure 4.3: The impact of Chemical Free Energy on neck size over time.

As the coefficient B increases, the influence of non-conserved order parameters (η) on the Chemical Free Energy and microstructure evolution process becomes more prominent, in comparison to the concentration variable (c). This means that the chemical composition of a system is more likely to be affected by changes in non-conserved order parameters with an increase in coefficient B. To illustrate the impact of coefficients A and B on the evolution of Chemical Free Energy over time, Figure 4.4 showcases that an increase in coefficient B leads to a more significant change in the Chemical Free Energy over time, compared to an increase in coefficient A. This suggests that the impact of non-conserved order parameters on the Chemical Free Energy is heightened as coefficient B increases. At the same time, the effect of concentration variables on the chemical-free energy remains relatively unchanged. Moreover, Figure 4.3 indicates that an increase in coefficient B reduces the neck growth rate. On the other hand, a decrease in coefficients A and B increases the neck growth rate.

This implies that non-conserved order parameters play a crucial role in determining the neck growth rate, especially when the value of coefficient B is high.

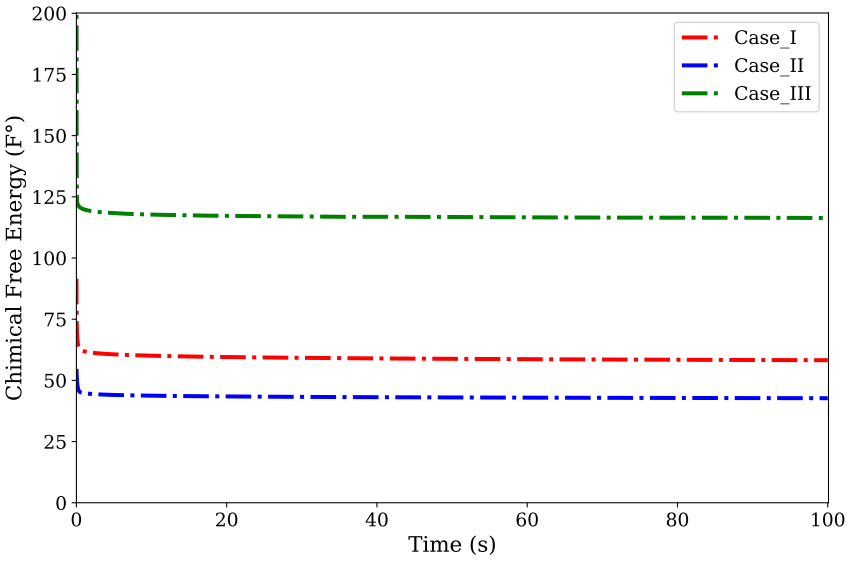

Figure 4.4: The evolution of Chemical Free Energy over time for different cases.

Thus, these results are consistent with the observations of the model under comparison. More details on this test can be seen in [58].

4.4.2/ Test II - Unequal size

In this test, the classical baseline problem of sintering two particles of unequal size is considered, and the diameter of the largest particle is twice the diameter of the smallest (15 nm and 30 nm); they are embedded in the simulation domain (2D - 55 X 40)nm with an initial minimum contact point, the red zone represents the particles (solid part), while the blue zone represents voids. The interface between two adjacent particles is called the neck or GB, and the interface between the particle (solid) and the void (porosity) represents the interface between the phases. The simulation conditions and the input data[2] for the test were adopted as set out in [73]. To complete the simulation data, we have set $B = 0.5$ and $k_\eta = 1.5$, and appropriate length, energy, and time scale have been applied.

[2]Data taken from Test Case in [73].

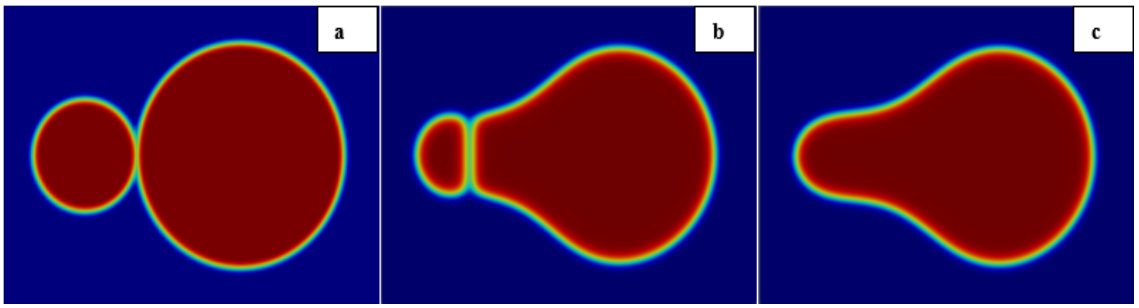

Figure 4.5: The evolution of non-conserved phase-field variable η of two particles. For unequal size, case II (a:t = 0, b:t = 0.75 s and c:t = 1.0, relative time).

The temporal evolution of both particles during sintering is illustrated in Figure 4.5, the relative neck growth rate between the particles and grain area evolution of the smaller particle are plotted w.r.t relative time in Figure 4.6.

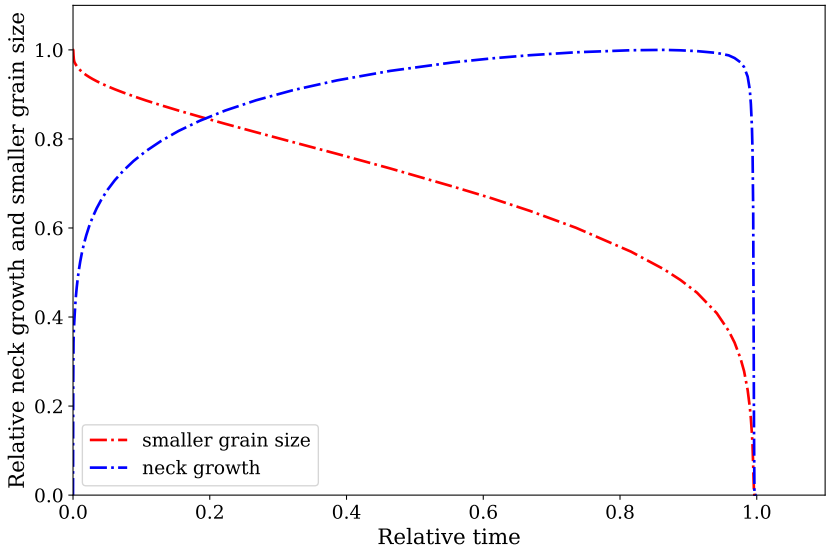

Figure 4.6: Relative neck growth and grain area as a function of relative time.

The model being compared is in alignment with these findings. In-depth information on the test results can be found in [73].

4.5/ Model simulations

4.5.1/ Setting up the model

In Section 4.3, we provide information on the methods for numerically solving the Solid-State Sintering phenomenon. In the previous section (Section 4.4), we qualitatively validated the model by conducting two tests, the results of which were consistent with the existing literature. This section focuses on applying the model to quantitatively and qualitatively study the Pressureless Solid-State Sintering process of Stainless Steel-316L (SS-316L) particles. As the model is multiphysics, we first simulated the coupling be-

tween the thermal field and the phase field to evaluate the effect of the thermal field. We then added the mechanical field to obtain the full model (Phase-field + Thermal field + Mechanical field, Figure 4.7), enabling us to evaluate the effect of the mechanical load similarly.

Table 4.1: Thermal and mechanical SS-316L parameters.

Property	Value	Units	Ref.
Thermal Conductivity, $\mathbf{k}$	$9.248 + 1.571 \cdot 10^{-2}T$	$w/(m.k)$	[102]
Density, ρ	$469.75 + 13.49 \cdot 10^{-2}T$	Kg/m^3	[102]
Specific heat, c_p	$8084.2 - 0.42086T - 3.8942 \cdot 10^{-5}T^2$	$J/(Kg.k)$	[102]
Young modulus, $\mathbf{E}$	200	GPa	
Passion ratio, ν	0.3	-	

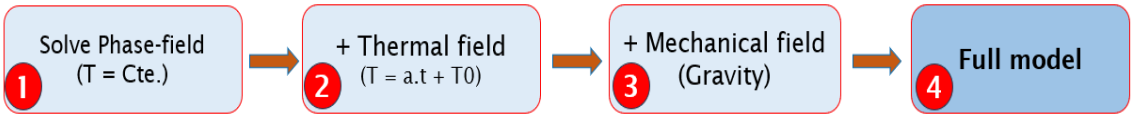

Figure 4.7: All the coupled steps to get full model

The classical two-particle model was used for unequal sizes to test the model. This was done to showcase the effects of all physical phenomena of the Pressureless Solid-State Sintering process, including rigid body motion and thermal and mechanical phenomena. In addition, the model was applied to the sintering of more than two particles to demonstrate the impact of the sintering temperature profile, sintering time, and particle size on microstructure evolution. The material properties used for all simulations are tabulated in Table 4.1 and 4.2 and are assumed to be isotropic.

Table 4.2: Microstructure (Phase-Field) SS-316L parameters.

Property	Value	Units	Ref.
Volume molar, V_m	7.012	m^3/mol	[103]
Surface energy, γ_s	2.41	J/m^2	[104]
Grain boundary energy, γ_{GB}	1.06	J/m^2	[104]
Volume diffusion pre-factor, D_{0V}	2.0	cm^2/s	[104]
Surface diffusion pre-factor, D_{0S}	$4.0 \cdot 10^3$	cm^2/s	[104]
Grain boundary diffusion pre-factor, D_{0B}	0.127	cm^2/s	[104]
Volume activation energy, Q_V	2.6	eV	[104]
Surface activation energy, Q_S	2.21	eV	[104]
Grain boundary activation energy, Q_{gb}	0.58	eV	[104]
Migration activation energy, Q_m	0.171	eV	[104]
Grain boundary mobility, M_{GB0}	$5.53 \cdot 10^{-8}$	$m^4/(s.Pa)$	[104]

In order for the model to work properly and achieve accurate convergence, the different physical parameters need to be consistent with each other, and the residual values of the physical equations should also be of a similar order for numerical convergence [58]. To achieve this, it is necessary to use appropriate scales that can convert the modeling parameters into dimensionless numbers. The chosen length, energy, and time scale is basically a trial-and-error approach. As simulations were carried out on a microstructural

level the length scale of $10^{-6}m$, and for energy and time scales, we selected $10^{21}J$ and $0.01s$, respectively, unless mentioned otherwise.

4.5.2/ Case I - Evaluating the Phase-field

A simplified model was simulated using only a Phase Field with constant temperature. The effect of rigid body motion was then incorporated to ensure the Phase Field model was complete and ready to be coupled with thermal and mechanical fields.

Simulations were performed in a 2D domain using a system with the spatial step size $\Delta x = \Delta y = l_0 = 0.3\mu m$ unless mentioned otherwise. The particles were enclosed within the simulation domain with a minimum contact point during the initial step, and the initial microstructure with unequal sizes ($d_1 = 4\mu m$ and $d_2 = 2\mu m$) was set up to showcase the impact of rigid body motion. The initial mesh was discretized to match or be smaller than the width of the GB interface (δ_{GB}). To enhance the quality of phase-field solutions, in subsequent time steps, adaptive meshing was utilized to ensure at least four elements at the GB interface (as depicted in Figure 4.8), minimizing error in the FE solution for Phase-Field equations [73], to do so and to know the appropriate the number of elements in the interfacial region, we have run a test keeping the same width ($\delta_{GB} = 0.6\mu m$) but for different mesh adaptive levels (h-levels 1, 2 and 3). Figure 4.9 shows how the refinement (h-level) level affects free chemical energy reduction over time. It is interesting to note that both h-levels 2 and 3 exhibit almost the same energy reduction behavior. It is important to keep in mind that sintering occurs as the energy decreases. In order to achieve a high level of accuracy in the finite element (FE) solution for phase field equations, we conducted all simulations using h-level 2. This approach not only improves accuracy but also reduces the computational cost by generating fewer elements compared to h-level 3 (see Figure 4.8).

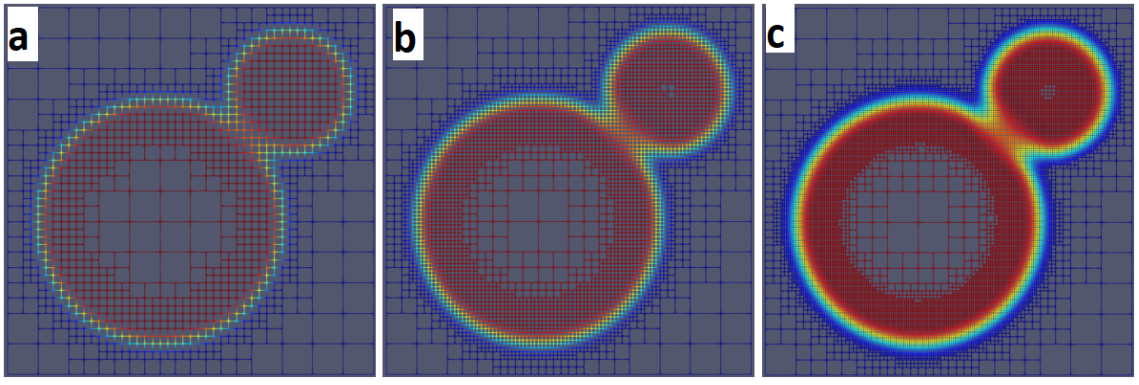

Figure 4.8: Adaptive meshing with an initial unadapted mesh size of 0.3 µm × 0.3 µm and an interface width of 0.6 µm: (a) h-level 1, (b) h-level 2, and (b) h-level 3.

Following the approach presented in Figure 4.7, a simplified model was simulated using only a phase field with constant temperature (1600 K). Then, the effect of rigid body motion was incorporated to ensure the phase field model was complete and ready to be coupled with thermal and mechanical fields. The role of grain boundaries as atom sources or vacancy diffusion generates the driving force for rigid-body motion in the sintering process, and through GB diffusion, each particle must move as a rigid body to facilitate densifying mass transport. Particle size, position, and void percentage influence

the translational and rotational velocity responsible for the rigid-body motion, ultimately determining the microstructure.

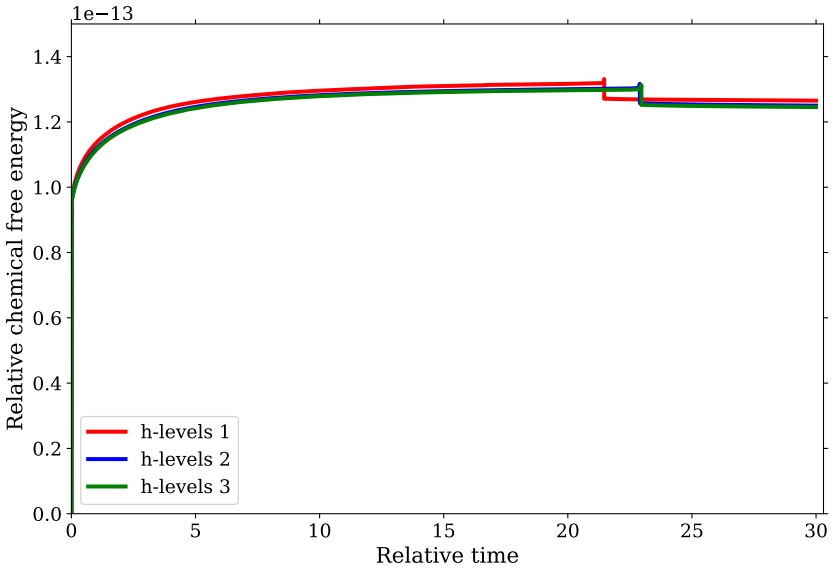

Figure 4.9: Relative chemical free for different h-level 1, h-level 2, and h-level 3.

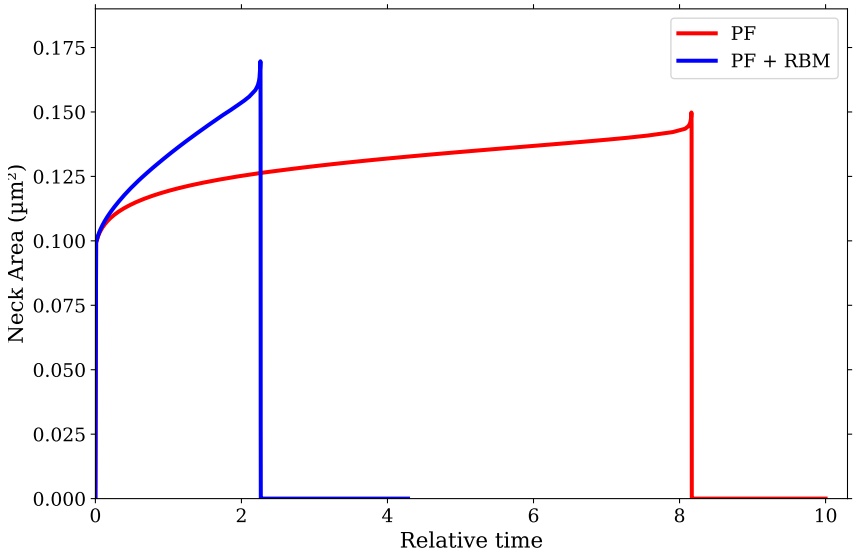

Figure 4.10: The evolution of neck growth over time for PF and PF+RBM model.

Figures 4.10 and 4.12 show the role of rigid-body motion in the case of two unequal particle sizes, which are positioned to observe the influence of RBM (translational and rotational velocity) during sintering. The phase field model from Figure 4.11 was modified to include rigid-body motion components. The stiffness constant k is 0.01, the constant c_0 is 0.9816, the mobility constants of the particle translational and rotational motion m_t and m_r are 5.0 and 1.0 respectively, the threshold for distinguishing grain boundaries (c_{gb}) is 0.14. The threshold value for identifying grains by the "GrainTracker" is 0.1.

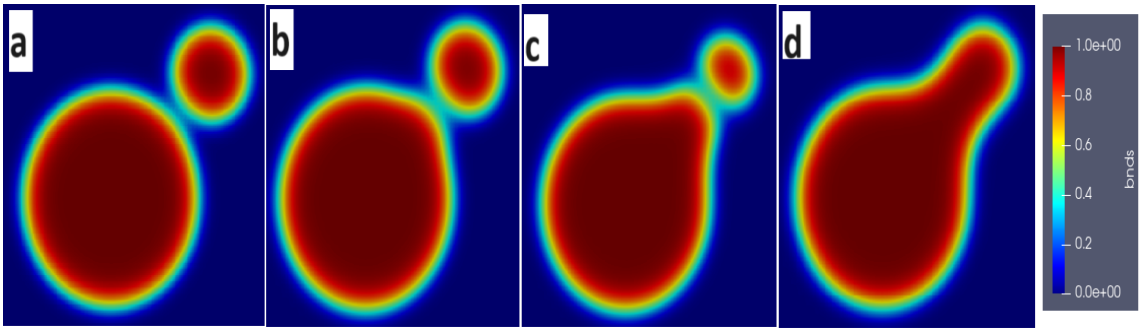

Figure 4.11: Grain morphology during sintering at simulation time a) t = 0, b) t = 2, c) t = 8,d) t = 10 for a constant temperature of 1600 K.

As observed in Figure 4.10, the rigid-body motion of particles causes faster neck formation and grain growth, while 4.12 shows that smaller particle experiences higher advection velocity than larger one, which makes it easier for the small particle to get closer to the large particle, not only because of its size but also because of the position of its center coordinate. On the other hand, you can see in the same figure that the velocity field varies during the sintering process, reaching its highest value and lowest at the beginning and end of the process.

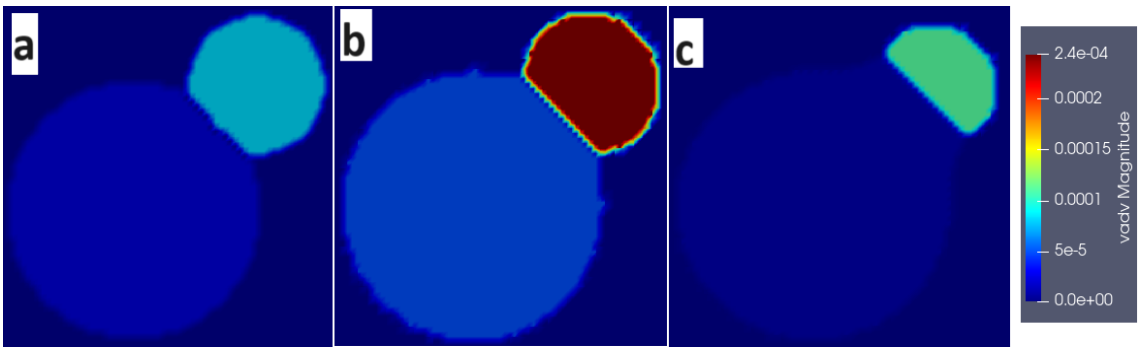

Figure 4.12: The evolution of advection velocity of each particle during sintering at simulation time a) t = 0.01, b) t = 1.74, c) t = 2.26.

By analyzing Figure 4.13, we can observe how rigid-body motion affects the evolution of grain size. Specifically, smaller grains tend to disappear more quickly due to this effect. This observation can help us better understand the process of grain size changes and their underlying causes.

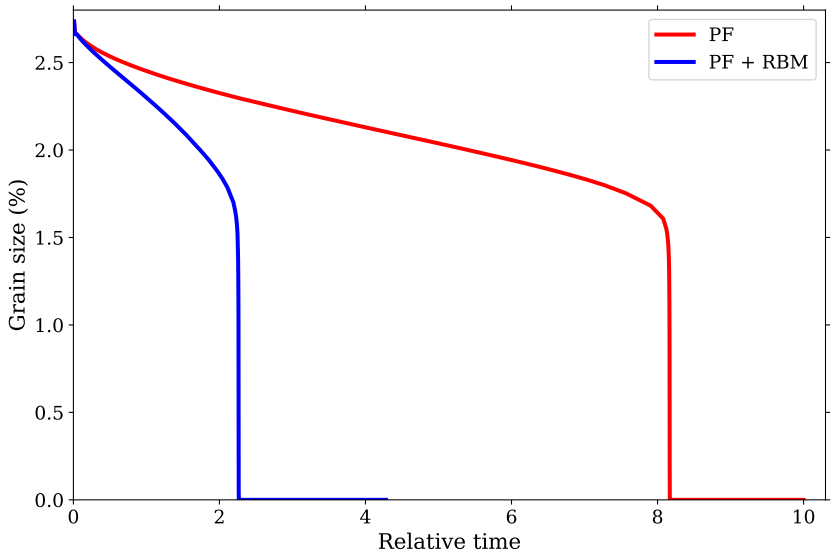

Figure 4.13: The evolution of grain size of the smaller particle over time for PF and PF+RBM model.

4.5.3/ Case II - Adding the thermal field

Once the PF model, including RBM, was complete, the thermal field was added by coupling it to the heat conduction equation. This step aims to evaluate the influence of varying the thermal field and the sintering temperature profile (temperature as a function of time) on the evolution of the microstructure. By coupling it with the heat conduction equation, we can confidently evaluate how the evolution of PF variables affects the thermal properties of materials, including density, thermal conductivity, and specific heat. For sintering, a heat source could provide the necessary temperature profile. The chosen temperature profile had an initial temperature of 1073 K and gradually increased to 1600 K, with a heating rate of 573/3. This temperature profile is depicted in Figure 3, represented by the blue line. Finally, this temperature profile was imposed as the thermal boundary condition to ensure proper sintering.

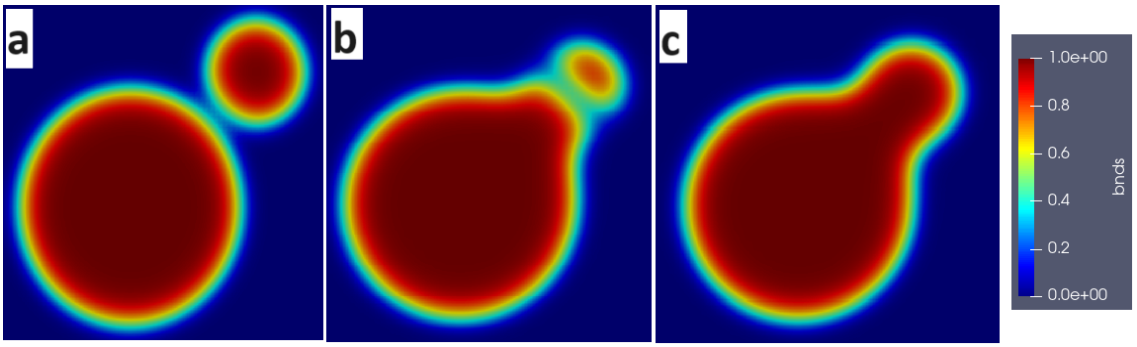

Figure 4.14: Grain morphology during sintering at simulation time a) t = 0.11, b) t = 2.74, c) t = 2.80 for sintering temperature profile $T = (527/3)t + 1073$,K.

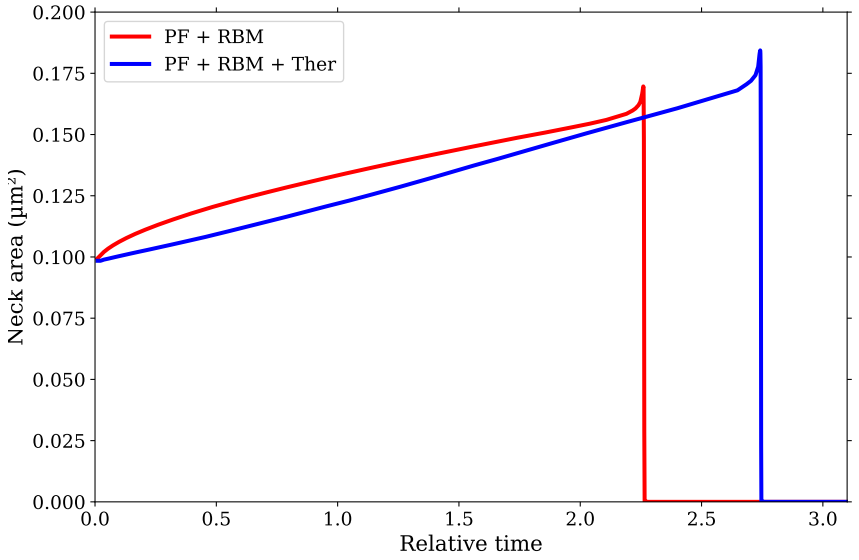

Figure 4.15: The Effect of thermal field coupling on the evolution of neck growth over time for PF+RBM and PF+RBM+Thermal model.

In Figure 4.14, it can be observed that the smaller grain is absorbed by the larger one at a relative sintering time of approximately 2.80. However, this time is longer when compared to the PF+RBM model at a temperature of 1600 K, as shown in Figure 4.15. It indicates that a longer sintering time is needed at a lower temperature. Moreover, keeping the sintering time under 3 ensures the temperature stays below 1600 K, as depicted in Figure 3.

In Figure 4.15, an interesting observation can be made regarding the consolidation of the material. It has been observed that combining two factors, namely low temperature and longer time, leads to greater neck growth, which enhances the consolidation of the material. This observation is significant as it provides insight into the factors that contribute to the consolidation of the material. The next sections will delve deeper into this aspect.

4.5.4/ Case III - Adding the mechanical field

In order to further refine the model, we incorporated the elastic effect into the previous version (PF+RBM+Thermal model) by linking it with the mechanical field generated by gravity. Our objective was to examine how gravity influences the microstructure evolution by way of the elastic effect. By coupling it with the mechanical equation, we can confidently evaluate how the evolution of PF variables affects the mechanical properties of materials, including the Young Modulus, and Poisson ratio. The model obtained after this incorporation is considered to be the complete model (PF+RBM+Thermal+Mechanical).

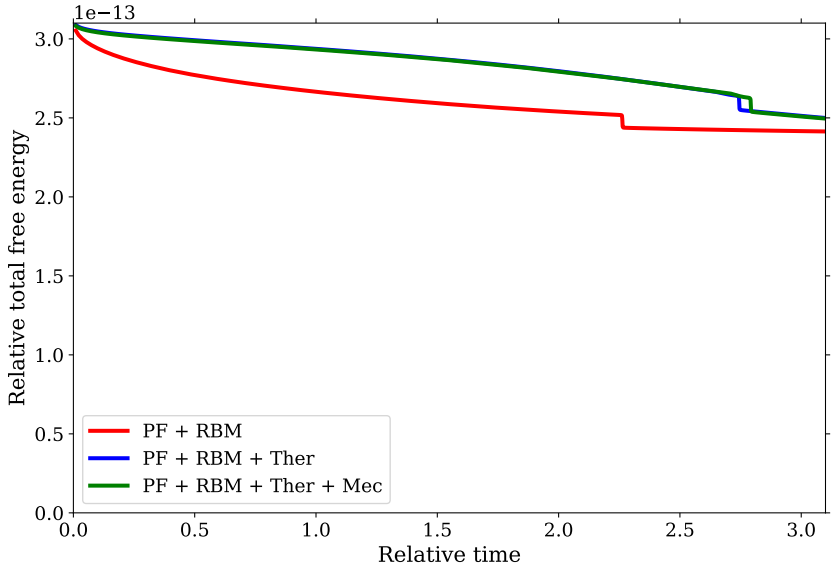

Figure 4.16: The comparison of Total free energy.

The elastic effect is obtained by adding the elastic energy to the total free energy (see Eq. 3.4). As can be seen in Figure 4.16, this coupling causes a slight reduction in the total free energy when compared to the total free energy of the model without the elastic effect. This shows that the elastic effect induced by gravity has a very small influence.

The same can be seen when looking at Figure 4.17, which shows that the growth of the neck considering the elastic effect is practically the same when compared to the model without the elastic effect. But this conclusion may differ in the case of a larger domain under study, or with a considerable number of particles.

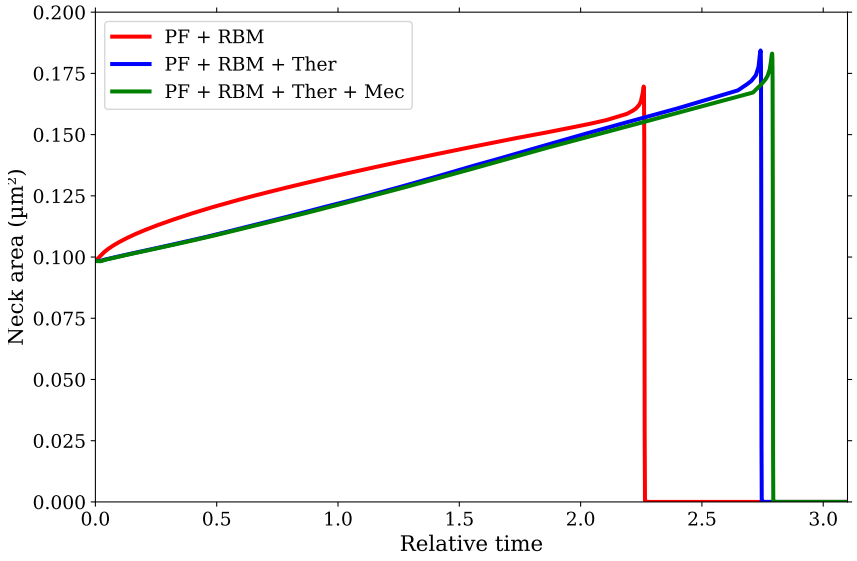

Figure 4.17: The Effect of mechanical field coupling on the evolution of neck growth over time for the full model.

4.5.5/ Case IV - Effect of thermal boundary conditions

In order to evaluate the influence of thermal boundary conditions, three cases were simulated (Case I, Case II, and Case III), with the same number and size of particles, but with different sintering temperature profiles, see Table 4.3. The main objective of this simulation is to evaluate the evolution of porosity (and microstructure) for different temperature profiles and sintering times, considering the full model. To this end, the three particles were arranged in such a way as to create porosity, see Figure 4.18 **a**.

The effect of temperature, first, changes the CH and AC mobilities, and thus, affects the evolution of microstructure, because the diffusion paths and GB mobility vary with temperature (see Eq. 3.24 and 3.25). Therefore, a small change in temperature can generally lead to a significant change in the evolution of the microstructure.

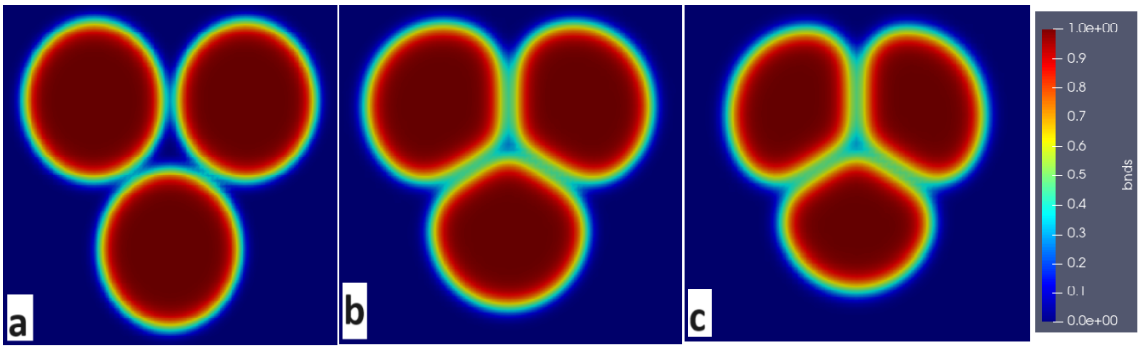

Figure 4.18: The microstructure evolution during sintering at simulation time a) t = 0.0, b) t = 3.93, c) t = 10, for Case I.

Figure 4.18 shows the evolution of the microstructure during the sintering process, indicating that as time increases there is a reduction in porosity and the microstructure tends to reach equilibrium. While Figure 4.19 shows the evolution of the thermal field during the sintering process, induced by the sintering temperature profile, it can be seen that there are temperature gradients, especially at the grain boundaries. However, the temperature distribution inside the particles seems to remain the same at all points, showing that (for small domains) the evolution of the thermal field during the sintering process behaves similarly to the temperature profile imposed as a BC, see Figure 4.20.

Table 4.3: Simulation parameters used to study the role of thermal BC.

Cases	**n.**	**Temp. profile (K)**	d_1**(µm)**	d_2**(µm)**	d_3**(µm)**
Case I	3	$(527/3).t + 1073$	4	4	4
Case II	3	$(427/3).t + 1073$	4	4	4
Case III	3	$(327/3).t + 1073$	4	4	4

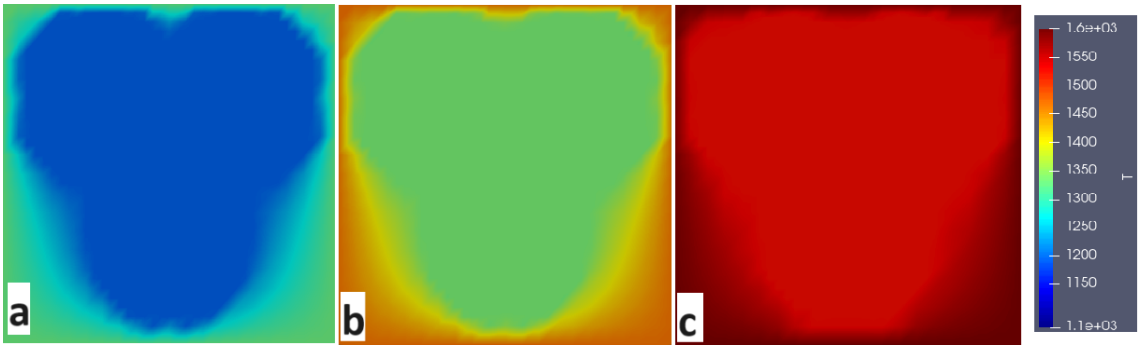

Figure 4.19: The evolution of thermal field during sintering at simulation time a) t = 1.31, b) t = 2.25, c) t = 3.13, for Case I.

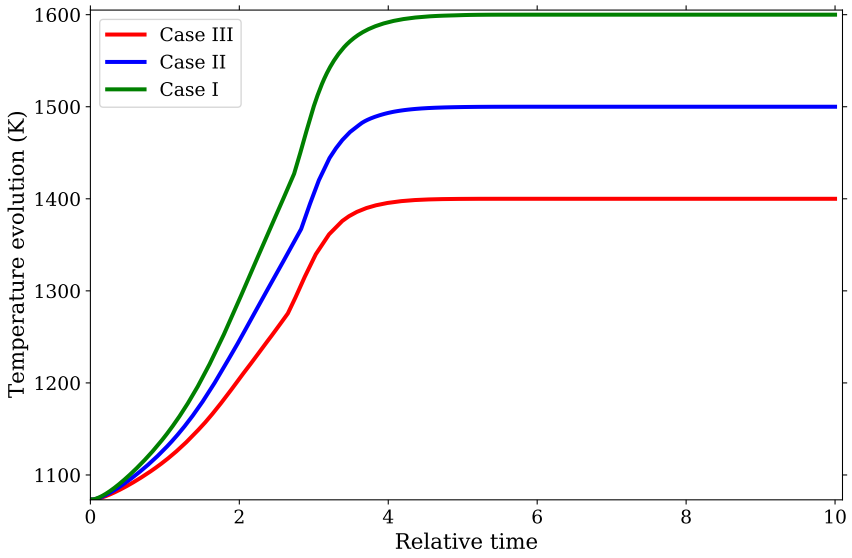

Figure 4.20: Evolution of the average temperature during the sintering process for different sintering profiles.

On the other hand, the position of each particle in relation to the other, as well as their size (equal size), makes the velocity of all particles equal at the same moment in time, as shown in Figure 4.21, it is also observed, as indicated in subsection 4.5.2, that the velocity field reaches its maximum during the sintering process, and tends to zero as the microstructure tends to reach equilibrium.

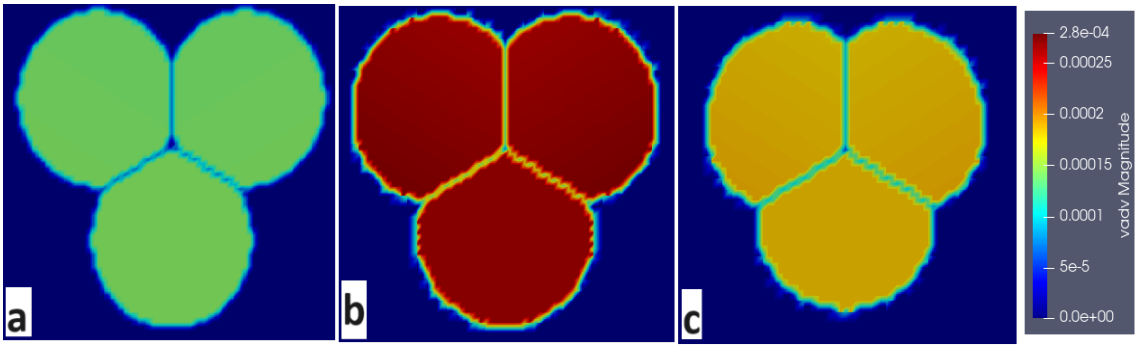

Figure 4.21: The evolution of advection velocity field of each particle during sintering at simulation time a) t = 0.0, b) t = 3.93, c) t = 10, for Case I.

The impact of the sintering temperature profile on the evolution of porosity, represented by the blue zone at the center of the domain formed by the three particles, is evaluated in Figure 4.18. In Case I, the porosity evolution is shown in Figure 4.23. However, the evolution of porosity can be divided into two parts, before and after t = 3, as shown in Figure 4.22. Before t = 3, the behavior of porosity is consistent because of the low temperature and high heating rate, which causes a sudden increase in temperature, as seen in Figure 4.20. After t = 3, with the constant temperature process (Case I: 1600 K, Case II: 1500 K, and Case III: 1400 K), a trend emerges where low temperatures lead to a slightly greater reduction in porosity.

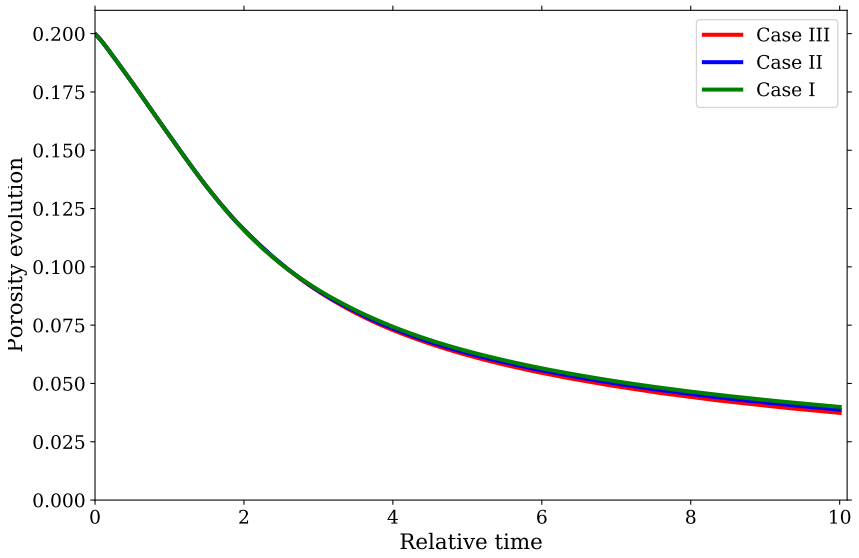

Figure 4.22: The Effect of thermal BC on the evolution of porosity over time.

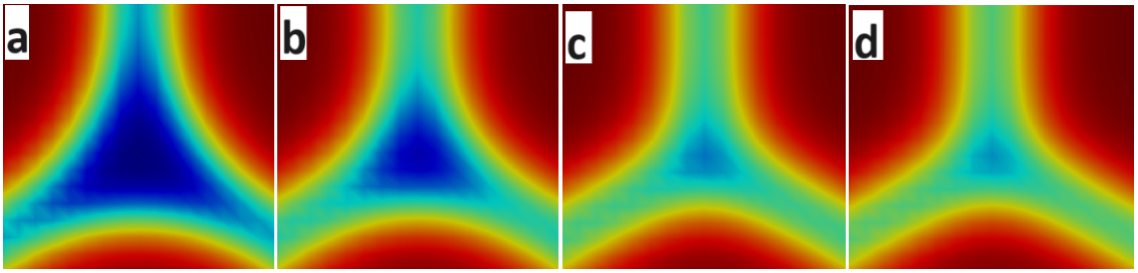

Figure 4.23: The evolution of porosity during sintering at simulation time a) t = 0.0, b) t = 2.02, c) t = 5.01, d) t = 10, for Case I.

4.5.6/ Case V - Effect of different particle sizes

To assess the impact of particle size on porosity and microstructure evolution, three simulations were conducted: Case I, Case II, and Case III. Each case featured the same number of particles and sintering temperature profile $((527/3).t + 1073, K)$, but with varying particle sizes outlined in Table 4.4. These simulations aimed to analyze the impact of different particle sizes on porosity and microstructure evolution using the full model. All three cases were designed to create porosity by arranging the three particles in a specific configuration, as demonstrated in Figure 4.24 **a**.

Table 4.4: Simulation parameters used to study the role of particle size.

Cases	**n.**	**Temp. profile (K)**	d_1**(µm)**	d_2**(µm)**	d_3**(µm)**
Case I	3	$(527/3).t + 1073$	4.0	4.0	4.0
Case II	3	$(527/3).t + 1073$	4.0	4.0	3.0
Case III	3	$(527/3).t + 1073$	4.0	3.6	3.0

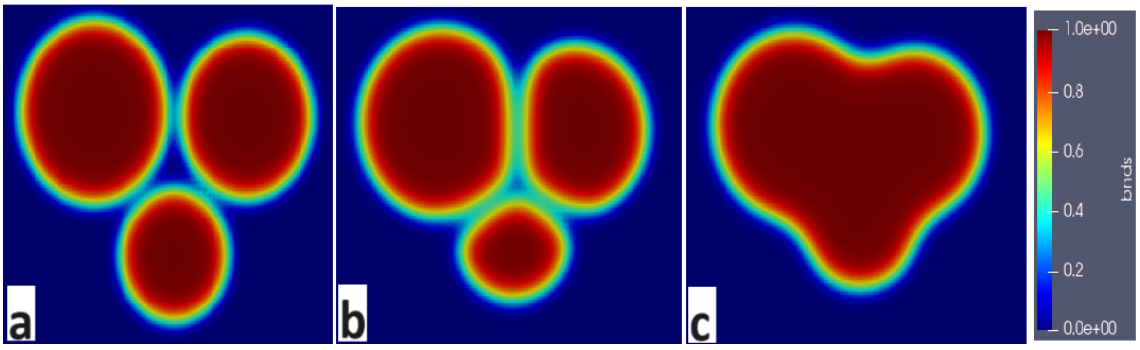

Figure 4.24: The microstructure evolution during sintering at simulation time a) t = 0.0, b) t = 3.93, c) t = 10, for Case III.

Figure 4.25 showcases how particle size affects pore size. It is evident that smaller particles generate smaller pores, as evident from case III (i, j, k, and l), which exhibits the lowest porosity compared to cases I (a, b, c, and d) and II (e, f, g, and h). Additionally, the graph highlights that the reduction in porosity is more rapid in case III than in cases I and II. Upon examining Figure 4.26 (Case II and III), it becomes apparent that even small adjustments to the pore size can slightly reduce the time required to eliminate them.

Additionally, this Figure demonstrates that the process of densification can be achieved swiftly.

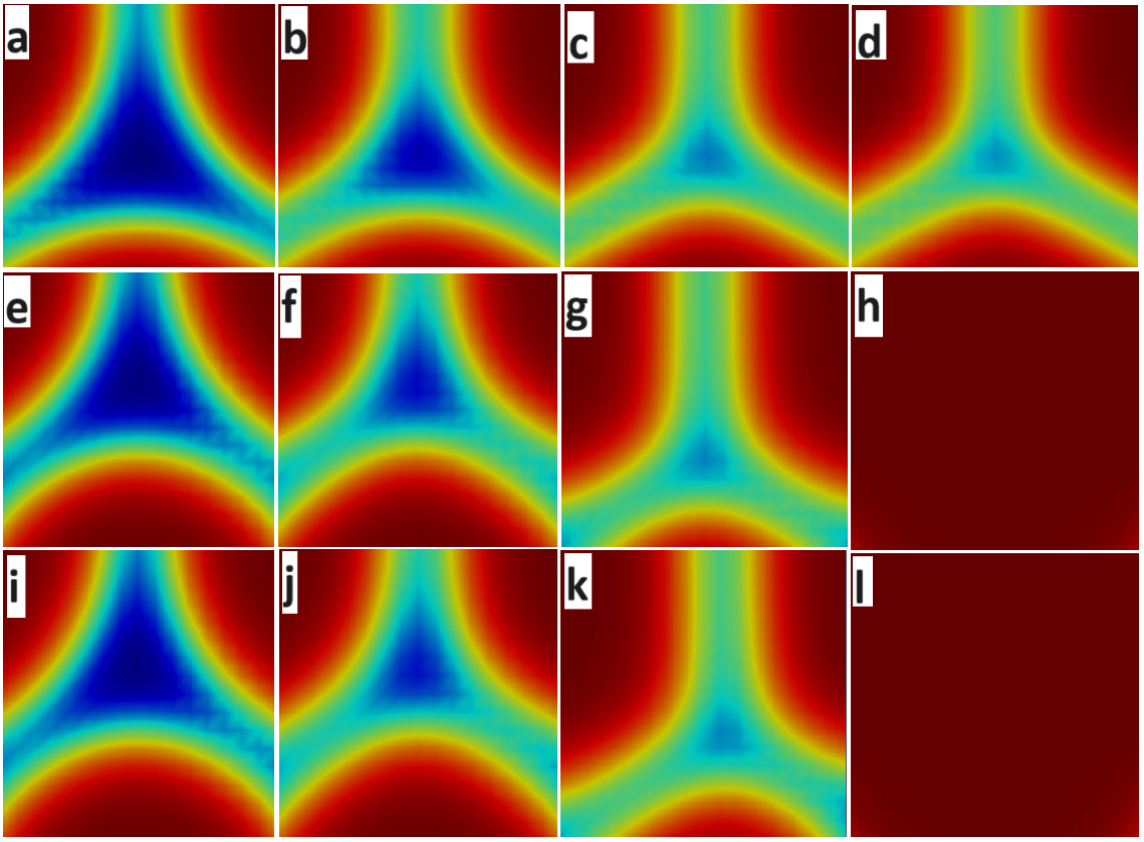

Figure 4.25: The evolution of porosity during sintering at simulation time a) t = 0.0, b) t = 2.02, c) t = 5.01, d) t = 10, for Case I (a, b, c and d), II (e, f g and h), and III (i, j k and l).

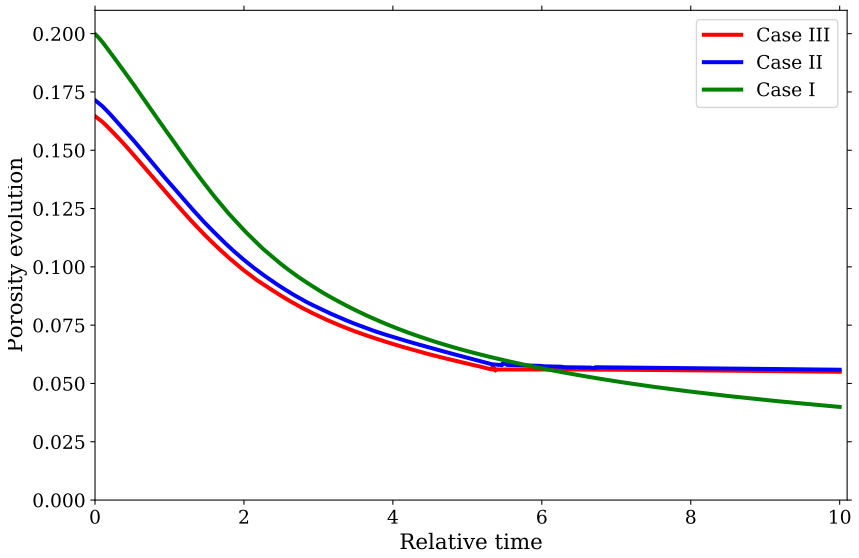

Figure 4.26: The Effect of particle sizes on the porosity evolution over time.

In order to gain a deeper understanding of this scenario, we can analyze the evolution of grain neck size over time. Based on the data presented in Figure 4.27, it is evident that the total neck size is smaller in Case III, resulting in a more rapid achievement of microstructural equilibrium. Moreover, Figure 4.28 provides valuable insight into the behavior of particle 2 across all cases, highlighting the impact of neighboring particle size.

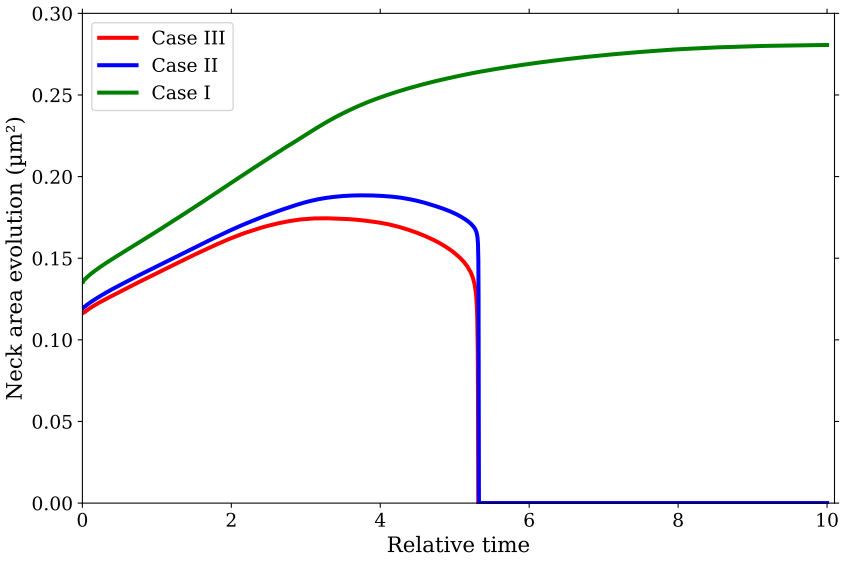

Figure 4.27: The evolution of neck area for Case I, Case II and Case III.

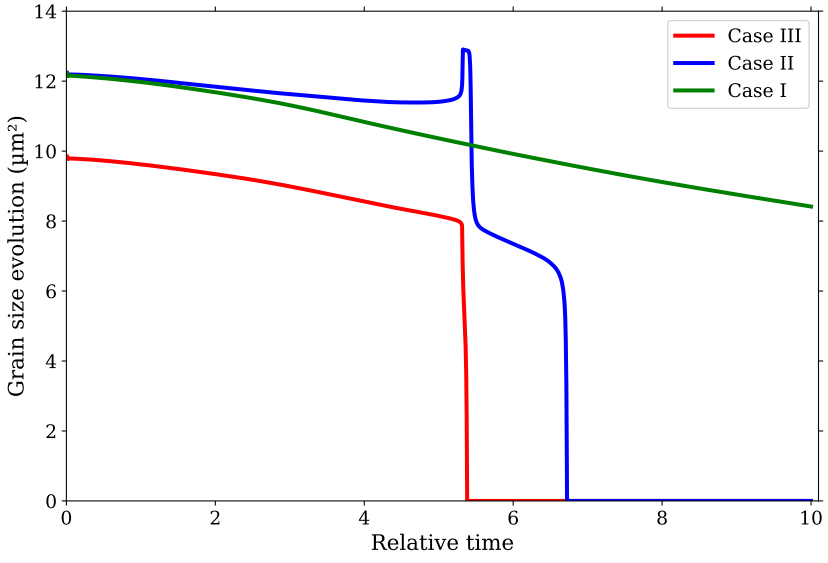

Figure 4.28: The evolution of grain size of the second particle for Case I, Case II and Case III.

It is important to acknowledge that the velocity field's behavior is significantly impacted by particle size, as depicted in Figure 3. The graph reveals that smaller particles tend to move faster, and their development is intricately intertwined with grain growth. The figure provides a precise illustration that particles reach peak velocities during the

process, but as they approach microstructural equilibrium, they gradually decelerate until they reach a complete standstill.

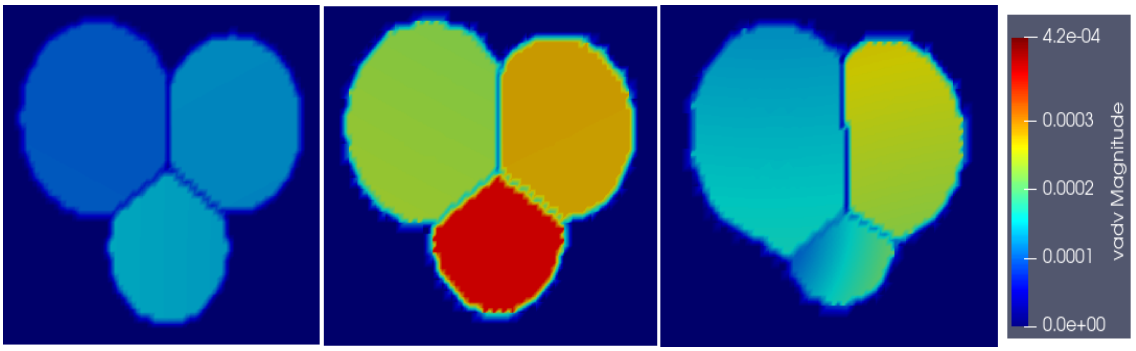

Figure 4.29: The evolution of advection velocity field of each particle during sintering at simulation time a) t = 0.0, b) t = 2.93, c) t = 5.29, for Case III.

4.6/ Conclusion

This chapter presents a contribution to modeling and simulating pressureless Solid-state Sintering (SSS) using numerical techniques. A finite element framework based on phase field equations coupled with thermal and mechanical fields has been developed, tested, and validated. The numerical techniques used to solve this multi-physics and non-linear problem have been explained. The model was theoretically validated using data from the literature, and the results were found to be consistent with those reported by the authors. Furthermore, the model was simulated to evaluate its behavior, first considering the phase field with RBM incorporation and then considering the influence of thermal and mechanical fields, the latter induced by gravity. The numerical techniques used to solve this complex problem have been described in detail, making it a valuable contribution to the field of solid-state sintering.

The simulation findings suggest that the developed model is capable of accurately forecasting the behavior of the sintering process concerning its microstructural, thermal, and mechanical properties. This means that the model can be utilized in MExAM, a similar process, for predicting and analyzing these properties. This could aid in enhancing the efficiency and precision of the sintering process and the MExAM technique, leading to better quality materials and improved manufacturing processes.

5

Numerical Model Applied to MExAM

Contents

5.1/ Introduction

Materials research is a field that seeks to enhance the properties of materials to make structures and components more efficient. The optimization of one or more properties, such as strength, density, and conductivity, is the primary goal of this research. By studying the behavior of materials, researchers can develop new materials or modify existing ones to improve their desired properties. The research can involve testing materials under various conditions, such as temperature, pressure, and humidity, to determine their behavior and potential applications. The ultimate aim is to create materials tailored to specific applications that can withstand the rigors of their intended environment. The sintering process is an essential area of research that aims to understand the behavior of materials under various sintering conditions. These conditions include sintering temperature, heating rate, sintering time, sintering atmosphere, and the type of material being used. By examining the effects of these factors on the sintering process, researchers can better understand how to optimize the sintering process for different materials, leading to improved performance and properties.

The process of evaluating properties and characteristics of materials has long relied on experimental testing, either through destructive or non-destructive methods. Unfortunately, this approach can be expensive and time-consuming, particularly when several experiments are required, and different properties must be investigated. As a result, new techniques and technologies are constantly being developed to offer more efficient and cost-effective alternatives to experimental testing. Computer simulations provide a range of advantages when it comes to testing materials and optimizing their properties for efficient application. These simulations can provide valuable insight into how materials behave in different conditions by simulating real-world scenarios, allowing researchers to fine-tune their properties for optimal performance. This can be particularly useful in experimental tests, where the behavior of materials can be difficult to predict without a comprehensive understanding of their underlying properties. Computer simulations are a powerful tool for advancing materials science and driving innovation in various industries. Therefore, in this chapter, we will use the simulation model developed in the previous chapter 4 to conduct an in-depth analysis of the pressureless solid-state sintering process. To achieve this, we will employ the design of simulation (DOS) methodology (similar to the design of experiments - DOE), enabling us to comprehensively evaluate the impact of various sintering parameters on the material's microstructural, thermal, and mechanical characteristics. Our main objective is to identify the critical process parameter that significantly affects the material's properties and determine the optimal combination of parameters that will enhance its properties. Through this investigation, we hope to gain a deeper understanding of the underlying mechanisms of the sintering process and generate insights that will be useful in the design and development of advanced materials. Section 2.3 of this document contains a wealth of information about the MExAM process that readers may find helpful. This section details the various steps involved in the process and provides a more comprehensive understanding of how the process works. Additionally, Figure 2.13 provides a visual summary of these steps, which can help provide an at-a-glance overview of the MExAM process.

5.2/ Simulation design

To predict and optimize microstructural and thermomechanical behavior at a microstructural level, it was crucial first to develop, test, and validate a computer model for simulating the sintering process (Chapter 4). This involves creating a virtual representation of the sintering process, utilizing real-world data and scientific principles, and then subjecting the model to a series of tests to ensure that it accurately reflects the behavior of the actual system. Once the model has been validated, it can simulate a wide range of conditions and scenarios for MExAM, allowing us to explore the effects of different variables on the sintering process's behavior and identify the optimal conditions for achieving specific outcomes. This can be invaluable in various fields, including metal extrusion additive manufacturing, where predicting and controlling microstructural behavior is crucial to achieving optimal performance and efficiency.

To ensure the correct application of the model in MExAM, it is crucial to follow the three fundamental components, as elaborated in Figure 5.1. The first component entails problem identification and input data import (Pre-processing). The second component involves the simulation to direct the study (Processing). The third component encompasses result analysis (Post-processing). All the steps are outlined below:

1. **Pre-processing - Input data:** The following steps must be taken at this stage:
    1. Select the type of material to be processed and enter the parameters associated with the selected material as input data.
    2. Define the initial microstructural arrangement as the starting condition for the simulation.
    3. Define the processing parameters, such as sintering temperature, sintering time, and heating rate, as sintering conditions.
2. **Processing - Simulation:** The following steps must be taken at this stage:
    1. Conduct simulations under the defined conditions.
    2. Monitor simulations for adjustments or corrections, if necessary.
3. **Post-processing - Output data:** The following steps must be taken at this stage:
    1. Analyze the outputs to understand the processed material's behavior.
    2. Define the combination capable of optimizing the material's properties and test and validate it.
    3. Conclude and report the results.

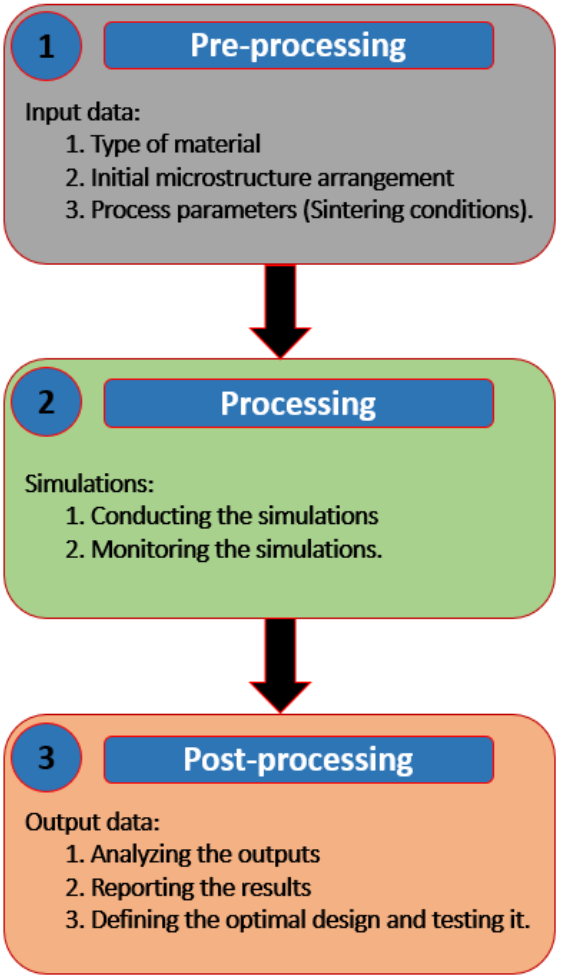

Figure 5.1: Main steps to apply the model to simulate the sintering process.

To use the model on MExAM, you can follow the steps outlined in Figure 5.1. The upcoming sections will provide a comprehensive guide to accomplishing this task. It is essential to follow the steps carefully to ensure that the model is applied correctly and that you achieve accurate results.

It's important to note that in the context of our work and this chapter, we have focused on studying a single material. However, the strategy implemented is entirely usable and applicable to other materials. In the following, our study will focus specifically on 316L steel.

5.2.1/ Input Data

The material we will be simulating is stainless steel-316L, a type of steel known for its excellent corrosion resistance properties. To accurately simulate this material, we will need to consider its microstructural (phase-field), thermal, and mechanical parameters as input data, which are all detailed in Tables 4.1 and 4.2. Other relevant information taken as input is the initial microstructural arrangement, which will be described in section 5.2.3.

Establishing the sintering parameters according to the specific material to be processed is crucial to achieve the desired outcome. The present study aimed to investigate the impact of different sintering parameters, namely sintering temperature, time, and heating rate, on the material's properties. The model simulations were conducted by varying the values of each parameter, which are specified in Table 5.1. The table comprehensively describes the different parameter values used in the simulations. This approach enabled a thorough exploration of the parameter space better to understand each parameter's impact on the model outcomes. It should be noted that the scales presented in section 4.5.1 were also used to convert the sintering parameters into dimensionless numbers. The purpose of these simulations was to evaluate the sensitivity of the sintering process to variations in each parameter, providing valuable insights into how each parameter affects the material's properties. By examining the findings of this research, it is possible to determine the most effective sintering parameters for the desired material properties.

Table 5.1: Processing parameters (sintering conditions) used to simulate the model.

Sintering temperature (°C)	**Heating rate**	**Sintering time**
1200	5	30
1250	10	60
1300	20	90

Sintering is a process used to form solid materials by heating them to a temperature below their melting point. The sintering process is activated at a minimum temperature that varies depending on the type of material used. For instance, it has been reported by German and cited by [42] that the sintering of 316L material commences at a temperature above 800°C. The peak sintering temperature is determined based on the material and the type of manufacturing technology applied to obtain the "*green part*". [26] recommends that for parts made from 316L and obtained by MExAM technology, the sintering temperature must be higher than 0.75 of the melting temperature. This is because the sintering process of 316L material requires a relatively high temperature to achieve full densification and avoid defects.

A recommendation has been made that various temperature combinations should be

utilized to create different sintering temperature profiles. This approach requires careful selection, as the sintering temperature profile significantly impacts the final properties and microstructure of the material. Therefore, it is essential to consider the final product's desired characteristics and choose the appropriate temperature combinations to achieve the desired outcome. By doing so, the quality of the final product can be greatly improved, ensuring that it meets the required standards.

5.2.2/ Output data

To achieve the goal of predicting the thermomechanical and microstructural behavior of the Solid-state sintering process and optimizing the processing conditions, we have identified the following as the primary outputs: a comprehensive analysis of the microstructure evolution during the sintering process that consists of a detailed characterization of the resulting microstructure, and a thorough assessment of the mechanical properties of the sintered material. These outputs, mentioned below, are essential for understanding the sintering process and developing strategies to enhance its efficiency and effectiveness.

- **Microstructural characteristics**
  - Microstructural evolution under different sintering conditions;
  - Porosity evolution and the growth of grains (particles), and;
  - The behavior of the conserved parameter of the phase field for different scenarios.
- **Thermomechanical properties**
  - Density;
  - Thermal conductivity and specific heat, and;
  - Modulus of elasticity.

5.2.3/ Initial microstructure arrangement

In the study, the evolution of the microstructure and phase field variables are essential factors to consider, as they depend on the size and position of the particles. Section 4.5.6 delves deeper into this topic, highlighting the importance of the initial microstructural arrangement, which is defined by the size and initial position of the particles. This arrangement represents the initial condition of the simulation, making it a crucial factor in the study. To obtain accurate data, this study conducted an experimental characterization of the microstructure of the green part using microscopic analysis by SEM (Figure 5.2) and particle size distribution through diffraction granulometry analysis (Figure 5.3), and the result agrees with Figure 2.10. The size and position of the particles were analyzed and studied to determine the initial arrangement of the microstructure.

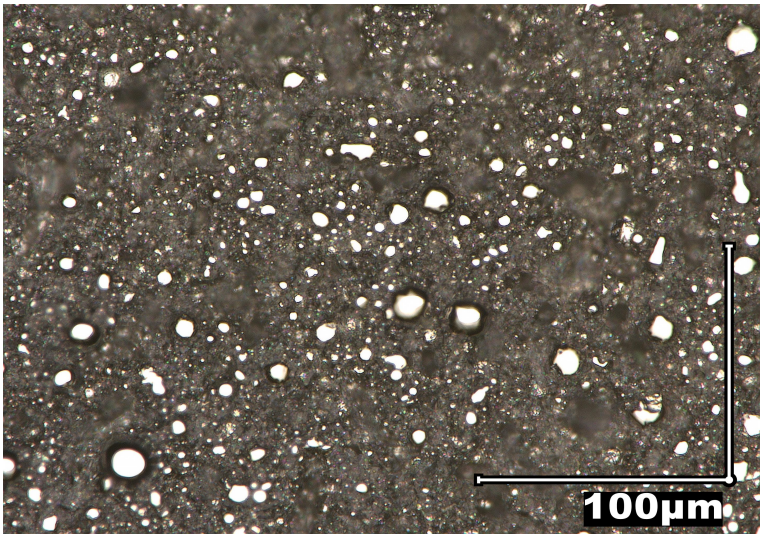

Figure 5.2: SEM image of the green part before sintering.

Thus, the positions of particles were generated randomly. In contrast, their sizes were generated using the Weibull cumulative distribution (according to equation 2.3), and the shape was considered circular, as shown in figure 5.2. The number of particles used in the simulation was carefully selected to ensure that the domain of the study was large enough to yield meaningful results. Each particle was assigned a size value determined using the Weibull distribution. For more information about the sizes of the particles used in the simulation, please refer to Table 5.2, which provides detailed information on the size distribution of the particles.

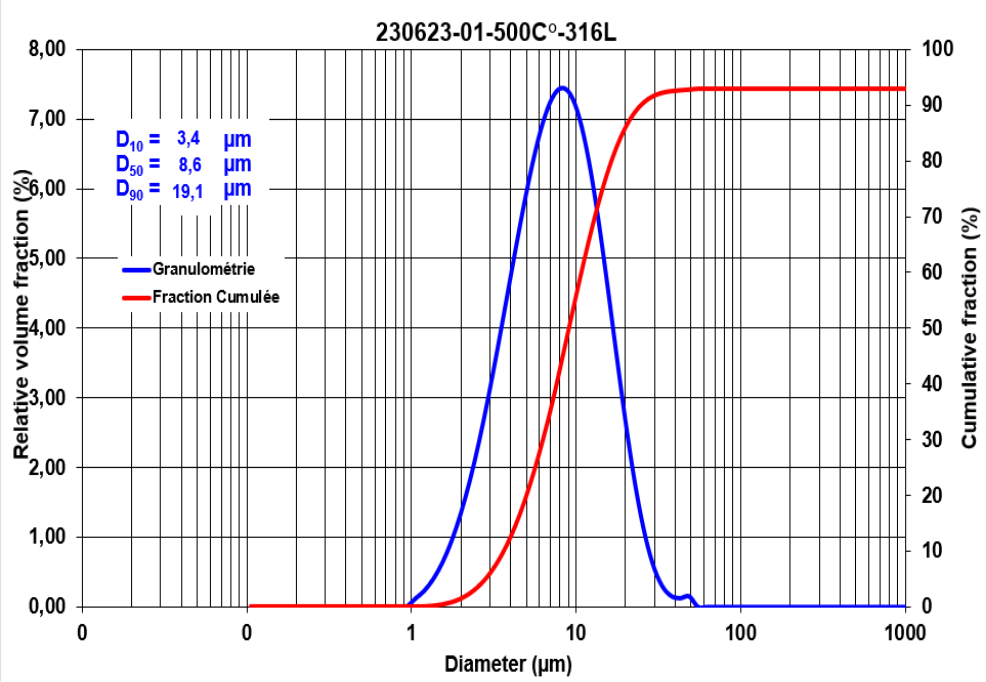

Figure 5.3: Result of the particle size distribution obtained by diffraction granulometry analysis of the powder, which was obtained after thermal debinding of the green part at 500 °C.

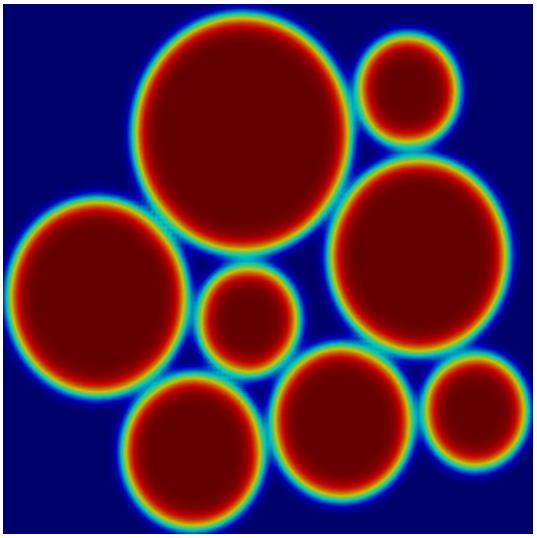

Figure 5.4: Initial microstructure arrangement used as the initial condition for simulations.

In this context, the domain representing the initial arrangement of the microstructure was generated considering stability and numerical convergence. This domain was then used as the initial condition for the simulation. Figure 5.4 illustrates the visualization of the domain. However, for the study of microstructural evolution and thermomechanical behavior, a representative subdomain was selected (see Figure 5.5, right side), allowing for a detailed analysis of the microstructure's behavior and material properties evolution during the simulation.

Table 5.2: Particle sizes used to create the initial microstructural arrangement.

n.	d_1**(µm)**	d_2**(µm)**	d_3**(µm)**	d_1**(µm)**	d_2**(µm)**	d_3**(µm)**	d_2**(µm)**	d_3**(µm)**
8	5.0	3.0	4.0	6.0	4.0	5.0	3.06	3.0

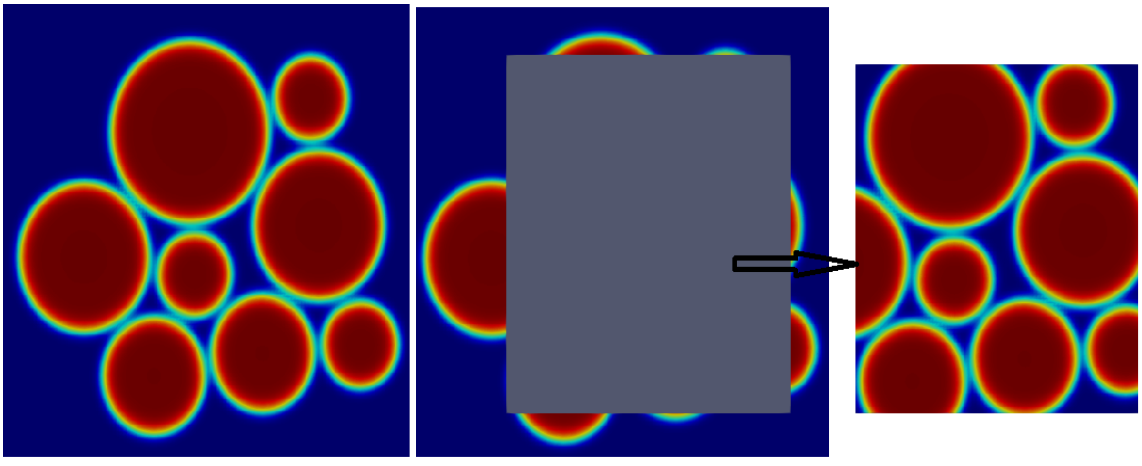

Figure 5.5: Specification of the domain under study.

5.3/ Simulation-based design of experiments

Design of experiments (DOE) is a statistical methodology that enables researchers and scientists to understand how different process parameters impact response variables such as processability, physical properties, or performance. It is a powerful mathematical tool that helps to design and conduct experiments, collect data, and analyze results to optimize the process performance and maximize the product properties. The primary objective of DOE is to identify the critical factors that impact the process or product performance and determine how to control them to achieve the desired results. Using statistical models and analysis methods, researchers can simultaneously evaluate the effects of multiple factors and predict the outcome of the experiments under different process conditions. DOE methodology involves several steps, including experimental design, data collection, statistical analysis, and interpretation of results. During the experimental design phase, researchers identify the factors that affect the performance and determine the levels at which the experiments will be conducted. They also select a statistical design that enables them to evaluate the effects of multiple factors simultaneously and minimize the number of experiments required [105, 106, 107, 108]. Instead of using experimental tests, this study will replace them with computational tests (final results of simulations). Thus, the purpose is to couple computer simulations with the design of experiments approach to study the sintering process.

5.3.1/ Taguchi approach

The Taguchi method is an experimental design technique based on the traditional one-variable-at-a-time DOE (Design of Experiments) approach. However, unlike the traditional approach, the Taguchi method aims to reduce the combination of selected parameters to obtain the best possible results. It is a refined method widely used in various fields, especially engineering, to design high-quality systems with optimal performance and minimal cost. The Taguchi method is a powerful tool that introduces an integrated, simple, and systemic approach to designing experiments. This approach helps identify the best design set for quality, performance, and computational cost. The method involves three steps [21, 109, 110]:

1. **Design of Experiments (DOE):** This step involves selecting the appropriate factors and levels to be tested in the experiment. The Taguchi method uses an orthogonal array to design the experiment, which helps to reduce the number of experiments required.

2. **Signal-to-Noise (S/N) Ratio Analysis:** This step involves determining the degree of variation in the output data and identifying the sources of variability. The S/N ratio is calculated using a specific formula that takes into account both the signal (the desired output) and the noise (the unwanted variation).

3. **Optimization:** This step involves identifying the best combination of factors and levels to achieve the desired output. The Taguchi method uses a statistical approach called the Analysis of Variance (ANOVA) to identify the significant factors and their optimal levels.

5.3.2/ Process parameters optimization

This project's experiments (simulations) aimed to determine the effects of sintering parameters (factors) on the final material properties and identify the optimal set of factors to optimize the final material properties. Based on the simulations conducted, three sintering factors were selected: sintering temperature (A, 1200–1300°C), heating rate (B, 5–20), and sintering time (C, 30–90) because the influence of these factors on the result may vary non-linearly, each factor is designed with three levels, as shown in Table 5.3.

Table 5.3: Factors and levels for the sintering simulations.

Process parameter	**Factor**	**Level 1**	**Level 2**	**Level 3**
Sintering temperature (°C)	A	1200	1250	1300
Heating rate	B	5	10	20
Sintering time	C	30	60	90

For our study, we opted for the Taguchi L_9 (3^3) orthogonal array (OA) design. This particular design granted us the necessary degrees of freedom to thoroughly explore the experiment while also enabling us to examine how different parameters impact the process performance. Additionally, it facilitated the acquisition of an optimal and well-performing process. You can refer to Table 5.4 for a visual representation of the L_9 (3^3) (OA) design, which arranges the parameters and their correlated levels in the way most likely to affect the process. Our trials resulted in optimal parameters unaffected by environmental changes and other noise sources.

Table 5.4: Simulations layout and factors distribution of L_9 (3^3) (OA).

Simulations n.	**A**	**B**	**C**	**Sint. temperature (°C)**	**Heating rate**	**Sint. time**
1	1	1	1	1200	5	30
2	1	2	2	1200	10	60
3	1	3	3	1200	20	90
4	2	1	2	1250	5	60
5	2	2	3	1250	10	90
6	2	3	1	1250	20	30
7	3	1	3	1300	5	90
8	3	2	1	1300	10	30
9	3	3	2	1300	20	60

The final material properties of the simulated material, denoted by y_1, y_2, y_3,..., y_9, as listed in Table 5.5, were obtained by computing the property at the end of each simulation based on the final microstructural arrangement. The analysis of variance (ANOVA) technique was used to establish the relative significance of the factors that affect the final properties of the material. ANOVA is a table of information that displays the relative influences of factors and interactions assigned to an Orthogonal Array (OA) column. The effects of sintering factors on the final properties were determined from the ANOVA table. The three sintering factors, namely, temperature, time, and heating rate, were found to affect the properties at the 0.99 significance level significantly. Thus, this study provides valuable insights into the effect of sintering parameters on the final properties of the material, which can help optimize the sintering process to obtain the desired properties.

Table 5.5: Final material properties at the end of each simulation.

Simulations n.	**Sint. temperature (°C)**	**Heating rate**	**Sint. time**	**Final property**
1	1200	5	30	y_1
2	1200	10	60	y_2
3	1200	20	90	y_3
4	1250	5	60	y_4
5	1250	10	90	y_5
6	1250	20	30	y_6
7	1300	5	90	y_7
8	1300	10	30	y_8
9	1300	20	60	y_9

In Table 5.5, the variable y denotes each material property identified as outputs in subsection 5.2.2. This table presents the final values obtained for those properties after the simulations. It is important to note that these values are based on the input data and assumptions made during the simulation process. To provide a comprehensive overview of the research outcomes, all the findings have been thoroughly discussed in the section named 'Results and Discussion' (which can be found in Section 5.4). This section outlines the key observations and discoveries made during the study and provides a detailed analysis of the data collected. The insights presented in this section are critical for understanding the research outcomes and drawing meaningful conclusions.

5.4/ Results and discussion

5.4.1/ Microstructural behavior

The evolution of the material's properties is always a response to how the microstructure evolves, so controlling the process, i.e., processing the material under the desired conditions, is essential to adapt the material's behavior to the application. Figure 5.6 illustrates the final microstructure arrangement, porosity, and the growth of grains (particles) under different sintering conditions.

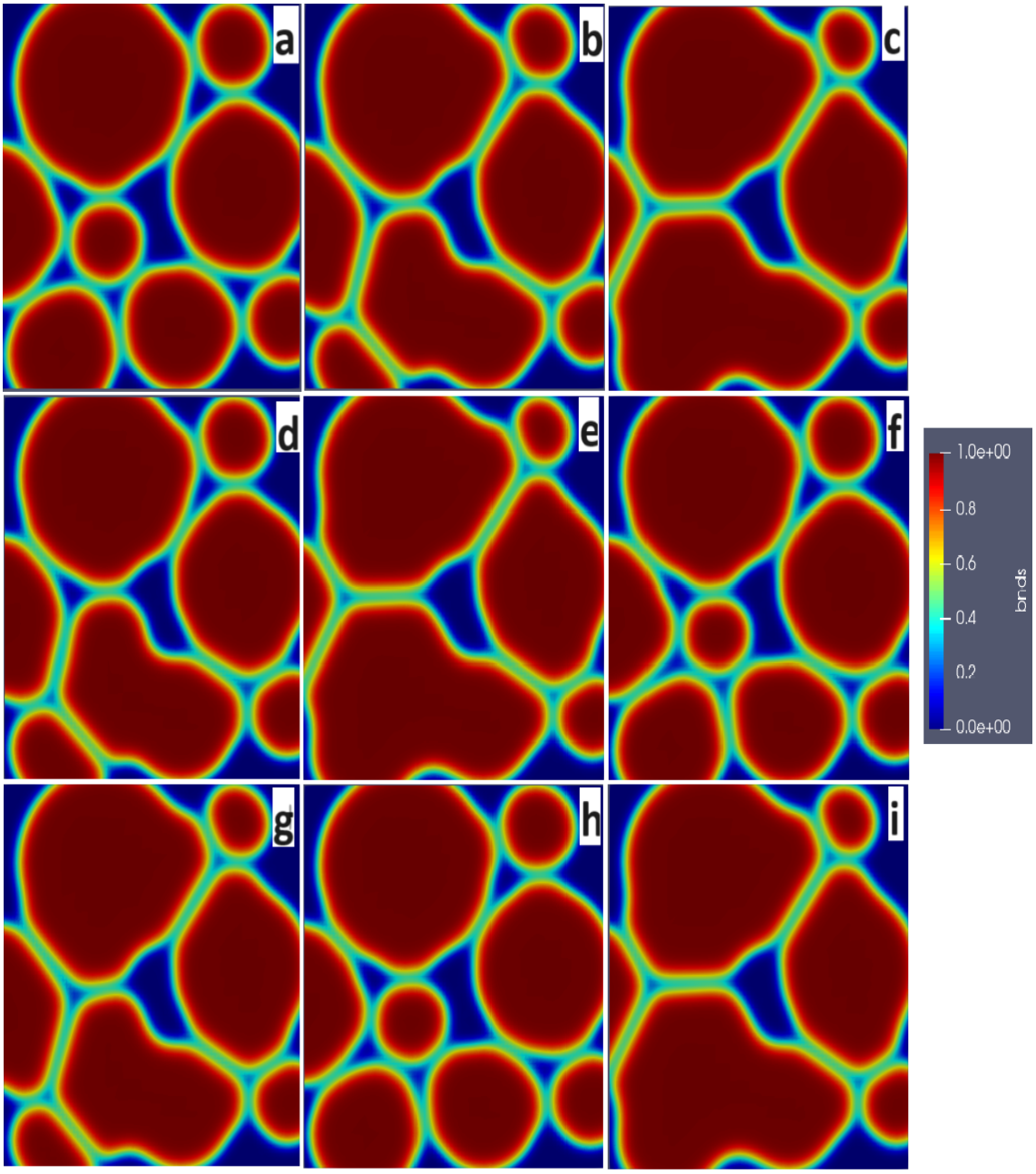

Figure 5.6: Final microstructure at the end of each simulation under different sintering conditions. **a)** 1200, 5, 30; **b)** 1200, 10, 60, **c)** 1200, 20, 90; **d)** 1250, 5, 60; **e)** 1250, 10, 90; **f)** 1250, 20, 30; **g)** 1300, 5, 90; **h)** 1300; 10; 30; **i)** 1300, 20, 60.

The interaction between pores and grain boundaries can have three different forms during the sintering process: i) the pores can retard grain growth, ii) the moving grain boundaries can drag the pores during grain growth, or iii) the grain boundaries can break away from the pores, leaving them isolated in the grain interior [21]. The evolution of porosity can qualitatively evaluate the evolution of the microstructure under different sintering conditions. Since this variable can be measured from the relative density, as shown in Eq. 2.5, an increase in relative density leads to a decrease in porosity. Therefore, the Taguchi experiment (see Table 5.6) was applied to predict the optimum combination

that increases the relative density considering the simulation conditions.

Table 5.6: Taguchi design for final relative density at the end of each simulation.

Simulations n.	Sint. temperature (°C)	Heating rate	Sint. time	Relative density
1	1200	5	30	0,840392
2	1200	10	60	0,839705
3	1200	20	90	0,841171
4	1250	5	60	0,840355
5	1250	10	90	0,841349
6	1250	20	30	0,839813
7	1300	5	90	0,840248
8	1300	10	30	0,840355
9	1300	20	60	0,840607

To maximize relative density, the optimum condition **"larger is better"** was selected, and the levels of the factors that contribute to the highest values were determined. Based on the response graphs illustrated in Figure 5.7, the highest relative density yield can be obtained with the combined of $A2$, $B3$, and $C3$, i.e., the sintering temperature of 1250°C, heating rate of 20, and sintering time of 90. It was possible to observe that this combination was not tested in the experiment, which demonstrates the ability of the orthogonal Taguchi experiment to identify the ideal factors in the multidimensional factor space.

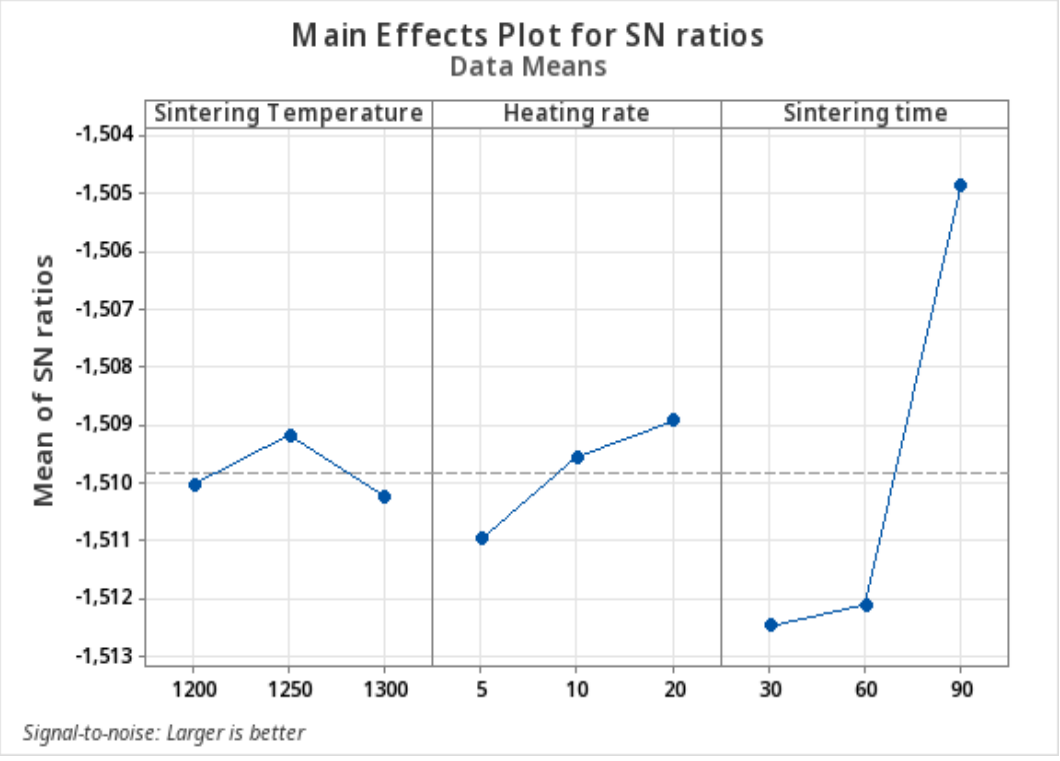

Figure 5.7: The optimal combination based on signal/noise ratio to maximize the relative density.

The effects of sintering factors on the final density were determined from the ANOVA

table (Table 5.7). All three sintering factors significantly affect the density at the 99% significance level. Compared with the other two sintering factors, the sintering time yields the most significant effect on the relative density, as shown by the much higher F ratio.

Table 5.7: ANOVA for relative density.

Source	DF	Adj SS	Adj MS	F-value	P-value
Sintering Temperature	2	0,000000	0,000000	0,01	0,986
Heating rate	2	0,000000	0,000000	0,05	0,953
Sintering time	2	0,000001	0,000001	0,82	0,550
Error	2	0,000001	0,000001		
Total	8	0,000002			

5.4.1.1/ Effects of sintering conditions on the microstructure

Compared to the time and heating rate factors, the temperature has a minor influence on the relative density, as shown in Figure 5.8. However, its influence is also significant, as demonstrated in Table 5.7. As the temperature increases, the rate of grain boundary movement rises. From Figure 5.8, it is possible to see that the densification is slightly faster at the sintering temperature of 1250°C than at the sintering temperature of 1300°C due to the isolation of the pores. Eliminating isolated pores is difficult, as the vacancies must diffuse to distant grain boundaries, which is a prolonged process. Maybe because the diffusion of vacancies from small to large pores occurs in the very late sintering stage. The results align with the observations reported by [21, 111, 112, 113].

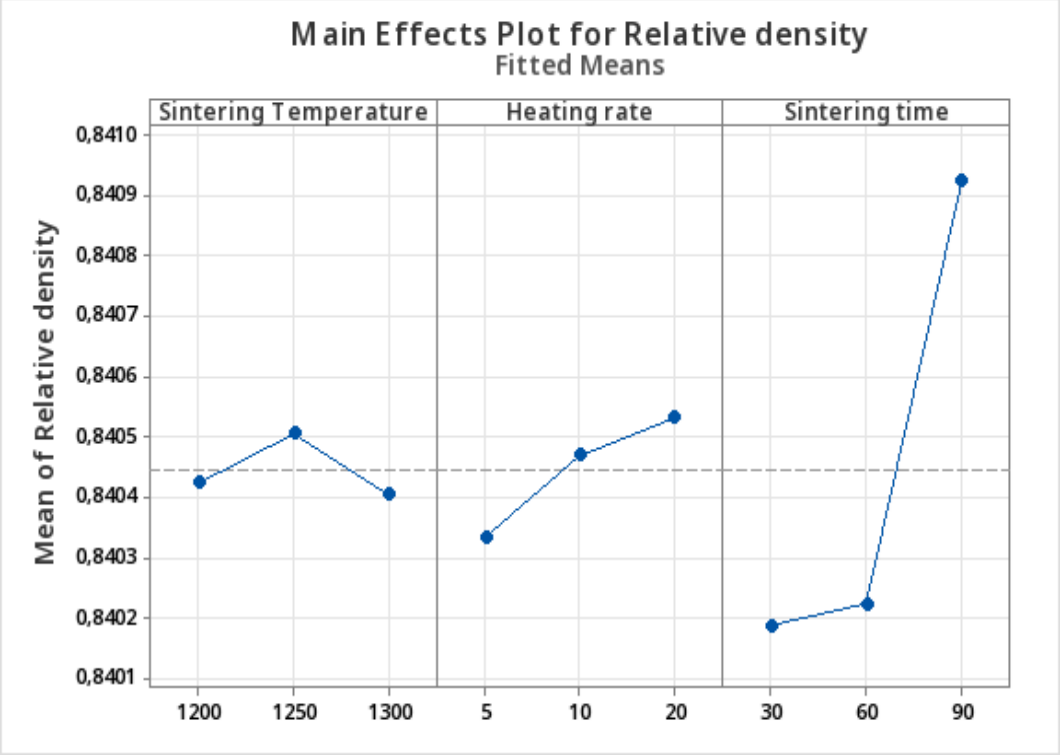

Figure 5.8: The main effects of each parameter on final relative density

As demonstrated in Figure 5.8, the heating rate factor strongly affects the final relative density but is shorter when compared to the time. It can also be seen that an increase in the heating rate causes an increase in density, leading to a decrease in porosity. However, very high heating rates can lead to thermal stresses due to thermal strain, so this parameter must be carefully selected to avoid this phenomenon. So, to avoid this, heating rates for 316L are often limited to 5-25°C/min [15, 20, 29, 31, 34, 36, 37].

Under the sintering conditions defined for the process simulation, the sintering time represents the most influential and significant factor (see Figure 5.8 and Table 5.7). It can also be seen that increasing the sintering time causes an increase in relative density, concluding that the longer the time, the greater the density. However, as discussed in the previous section, time loses its action once the microstructure reaches equilibrium.

5.4.2/ Thermal behavior

5.4.2.1/ Thermal conductivity

Thermal conductivity is defined as the rate at which heat is transferred by conduction through a unit cross-sectional area of a material when a temperature gradient runs perpendicular to the area, i.e., it measures the ability of a material to transmit heat through it [114]. Knowing the behavior of thermal conductivity allows for more efficient design. The material can be processed as a heat conductor or insulator, depending on its application. To be applied as an insulator, the Taguchi technique (see Table 5.8) is used to determine the best combination of sintering parameters that minimize thermal conductivity.

Table 5.8: Taguchi design (L9) for thermal conductivity at the end of each simulation.

Simulations n.	**Sint. temperature (°C)**	**Heating rate**	**Sint. time**	**Ther. conduct.**
1	1200	5	30	23,6311
2	1200	10	60	28,2018
3	1200	20	90	28,2391
4	1250	5	60	26,1195
5	1250	10	90	28,9390
6	1250	20	30	28,0067
7	1300	5	90	28,7745
8	1300	10	30	24,8704
9	1300	20	60	29,6485

To minimize thermal conductivity, the optimum condition **"smaller is better"** was selected, and the levels of the factors that contribute to the lowest values were determined. Based on the response graphs illustrated in Figure 5.9, the lowest thermal conductivity value can be achieved with a combination of $A1$, $B1$, and $C1$, i.e., a sintering temperature of 1200°C, a heating rate of 5 and a sintering time of 30. It was possible to observe that this combination was tested in experiment 1 (simulation 1 - Table 5.8).

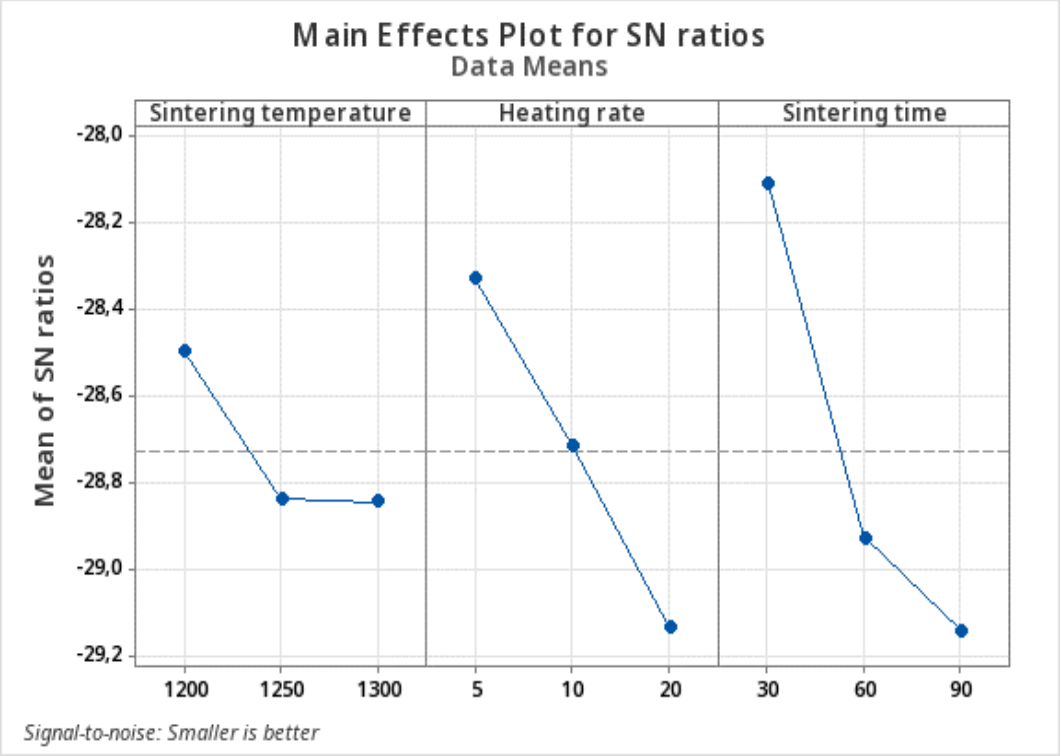

Figure 5.9: The optimal combination based on signal/noise ratio to minimize the final thermal conductivity.

The effects of sintering factors to minimize the final thermal conductivity were determined from the ANOVA table (Table 5.9). All three sintering factors significantly affect the thermal conductivity at the 99% significance level. Compared with the other two sintering factors, the sintering time has the most significant influence on the thermal conductivity, as demonstrated by the much higher F ratio.

Table 5.9: ANOVA for thermal conductivity.

Source	**DF**	**Adj SS**	**Adj MS**	**F-value**	**P-value**
Sintering Temperature	2	2,154	1,077	0,39	0,719
Heating rate	2	9,06	4,53	1,64	0,379
Sintering time	2	16,534	8,267	2,99	0,25
Error	2	5,521	2,76		
Total	8	33,269			

5.4.2.2/ Effects of sintering conditions on the thermal conductivity

The sintering temperature is the factor with the most minor influence on the minimization of thermal conductivity, as shown in Figure 5.10. However, its influence is also significant, as demonstrated in Table 5.9. From Figure 5.10, it is possible to see that the thermal conductivity is lower at the sintering temperature of 1200°C than at the sintering temperature of 1250°C and 1300°C due to the presence of the pores. Figure 5.6 (simulations a, b, and c) can help to understand this issue, as it shows that at a temperature of 1200°C, the presence of porosity is high, so heat conduction is low.

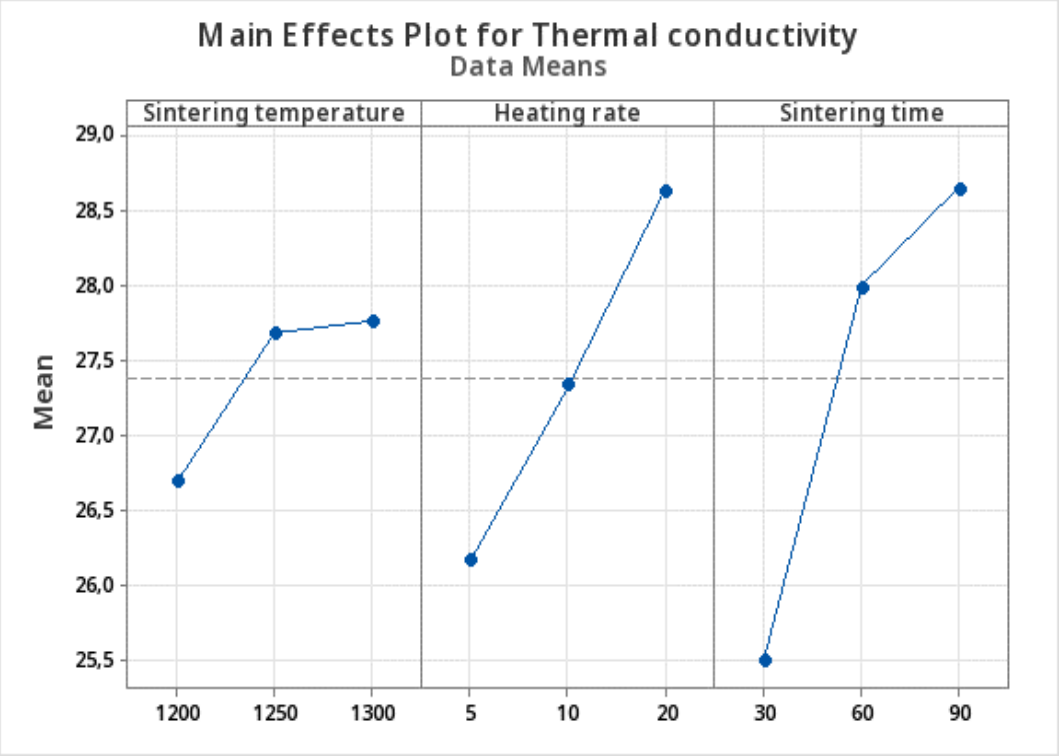

Figure 5.10: The main effects of each parameter on the final thermal conductivity

Under the sintering conditions defined for the process simulation, the heating rate has a strong effect on the minimization of final thermal conductivity but is less when compared to the sintering time. As demonstrated in Figure 5.10, a decrease in the heating rate leads to a decrease in the thermal conductivity value.

Compared to other factors, the sintering time represents the most influential and significant factor (see Figure 5.10 and Table 5.9) on the minimization of thermal conductivity. As Figure 5.6 illustrates, in simulations a, f, and h, it can be seen that whenever the sintering time is 30, the porosity level is high, which causes poor heat conduction. However, it can be said that short sintering times minimize thermal conductivity.

5.4.2.3/ Specific heat

Specific heat is a crucial thermodynamic property of a material which entails the amount of heat required per unit mass to raise the temperature of one degree Celsius. It directly deciphers the thermal characteristics and performance of any material e.g., materials having higher specific heat capacity elucidates its capability of storing a supreme amount of energy. Whereas, materials having lower specific heat capacity tends to hold lesser amount of energy [115]. In order to maximize its heat storage capacity, the Taguchi technique (see Table 5.10) is applied to determine the best combination of sintering parameters.

Table 5.10: Taguchi design (L9) for specific heat at the end of each simulation.

Simulations n.	Sint. temperature (°C)	Heating rate	Sint. time	Spec. heat
1	1200	5	30	539,702
2	1200	10	60	582,038
3	1200	20	90	582,813
4	1250	5	60	563,332
5	1250	10	90	589,000
6	1250	20	30	578,337
7	1300	5	90	587,303
8	1300	10	30	550,648
9	1300	20	60	595,372

Since the aim is to maximize the specific heat, the optimum condition **"larger is better"** was selected, and with the Taguchi approach was determined the levels of the factors that contribute to the highest values. Based on the response graphs of the Signal/Noise ratio, illustrated in Figure 5.11, the highest specific heat value can be achieved with a combination of $A3$, $B3$, and $C3$, i.e. a sintering temperature of 1300°C, a heating rate of 20 and a sintering time of 90. From Table 5.10 is possible to observe that this simulation with these conditions was not tested.

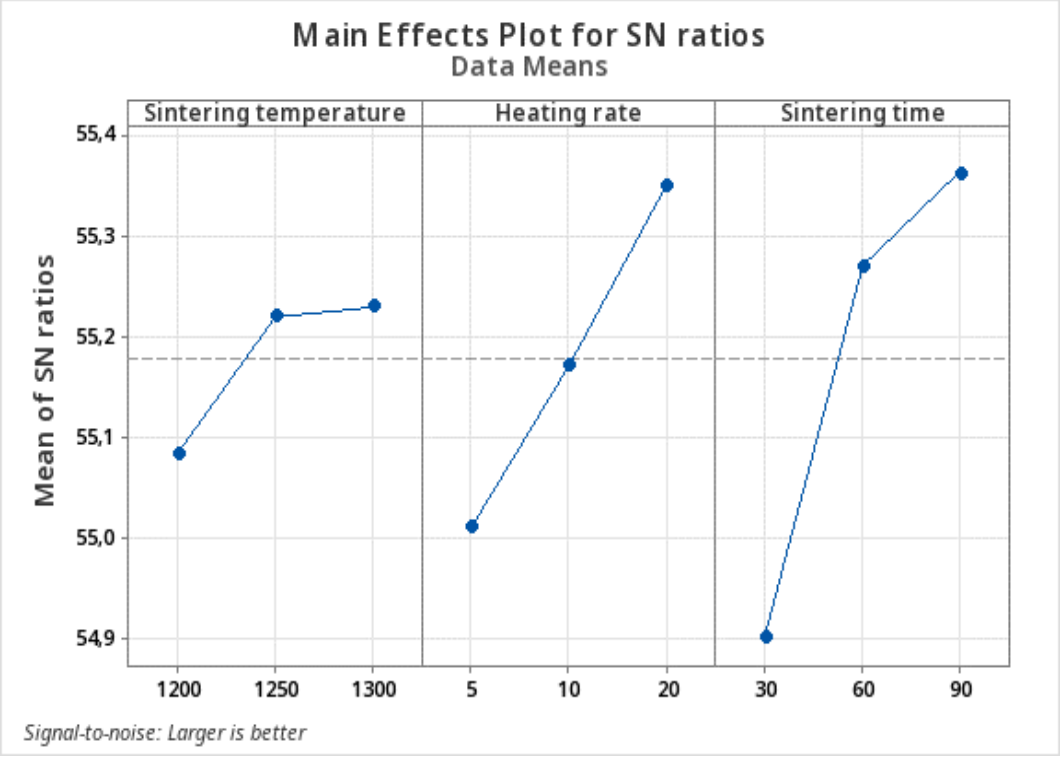

Figure 5.11: The optimal combination based on signal/noise ratio to maximize the final specific heat.

The ANOVA technique was applied to compute the effects of sintering factors to maximize the final specific heat (see Table 5.11). It was found that all three sintering factors significantly affect the specific heat at the 99% significance level. As observed in

other cases, the sintering time has the most significant influence on the final specific heat, as demonstrated by the much higher F ratio.

Table 5.11: ANOVA for specific heat.

Source	DF	Adj SS	Adj MS	F-value	P-value
Sintering Temperature	2	168,5	84,26	0,39	0,72
Heating rate	2	730,7	365,37	1,69	0,372
Sintering time	2	1523	761,48	3,52	0,221
Error	2	432,3	216,15		
Total	8	2854,5			

5.4.2.4/ Effects of sintering conditions on the specific heat

Among all the factors analyzed, the sintering temperature is the factor with less influence on the maximization of specific heat, as shown in Figure 5.12. However, its influence is very significant, as shown in Table 5.11. The results show that as the processing temperature increases, there is an improvement in the specific heat towards its maximization, see Figure 5.12, i.e. the specific heat is slightly greater at the sintering temperature of 1300°C than at the sintering temperature of 1250°C. This finding differs when comparing the effect of temperature on the maximization of relative density, where the temperature of 1250°C represents the optimum level for this factor. The proportionality between temperature and specific heat may be at the root of this behavior.

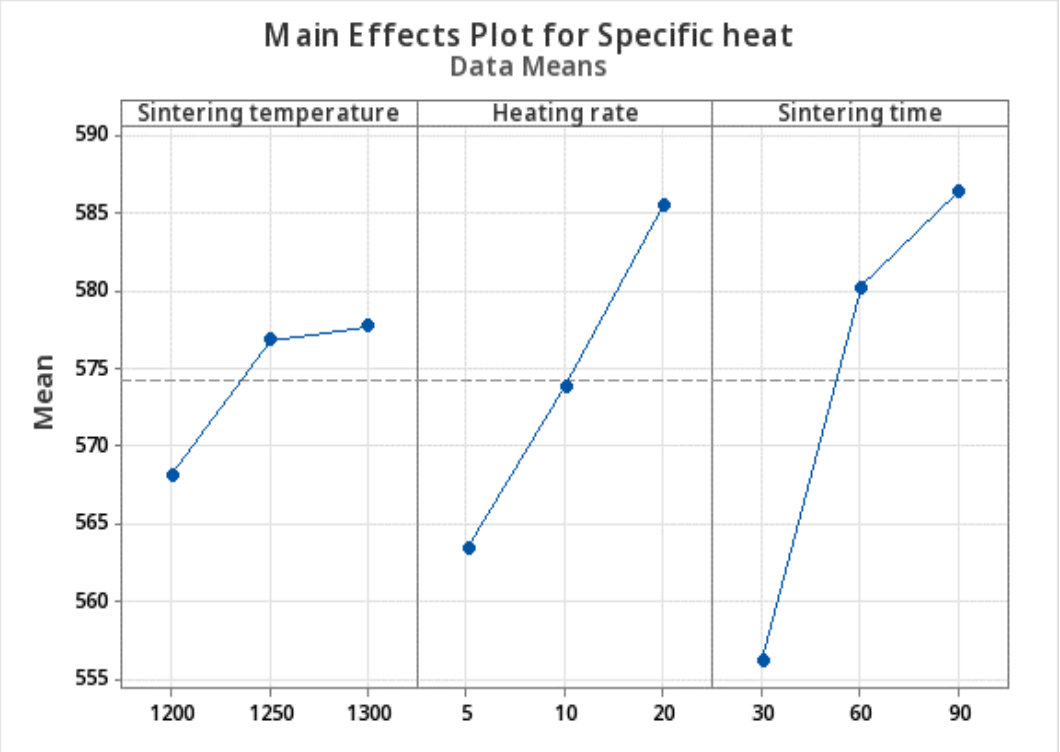

Figure 5.12: The main effects of each parameter on the final specific heat.

As demonstrated in Figure 5.12, the heating rate has a strong effect on the max-

imization of specific heat, being almost as important as the effect of the sintering time. While the sintering time represents the most influential and significant factor in the maximization of specific heat. (see Figure 5.12 and Table 5.11).

5.4.3/ Mechanical behavior

5.4.3.1/ Elastic modulus or Young modulus

Elastic modulus or Young modulus (E), is the ratio of stress to strain in the elastic deformation region of a material, indicates the resistance of the material of being deformed elastically when it is subjected to certain stress [116]. Basically, when you increase the modulus of elasticity, you increase the material's ability to resist in the elastic zone, preventing the appearance of permanent deformations. So, in order to determine the best combination of sintering parameters to maximize the elastic modulus, the Taguchi technique was applied. The layout and factors distribution of L_9 (3^3) (OA) for elastic modulus are represented in Table 5.12.

Table 5.12: Taguchi design (L9) for Young modulus at the end of each simulation.

Simulations n.	**Sint. temperature (°C)**	**Heating rate**	**Sint. time**	**E (Gpa)**
1	1200	5	30	172,560
2	1200	10	60	174,143
3	1200	20	90	174,375
4	1250	5	60	173,720
5	1250	10	90	174,466
6	1250	20	30	173,105
7	1300	5	90	174,321
8	1300	10	30	172,716
9	1300	20	60	174,609

Once the goal is to maximize the elastic modulus, the optimum condition **"larger is better"** was selected, and with the Taguchi approach was determined the levels of the factors that contribute to the highest values. Based on the response graphs of the Signal/Noise ratio, illustrated in Figure 5.13, the highest Young modulus is achieved with a combination of $A3$, $B3$, and $C3$, i.e. a sintering temperature of 1300°C, a heating rate of 20 and a sintering time of 90. From Table 5.12 is possible to observe that this simulation with these conditions was not tested. It should be noted that this combination maximizes the final value of the specific heat.

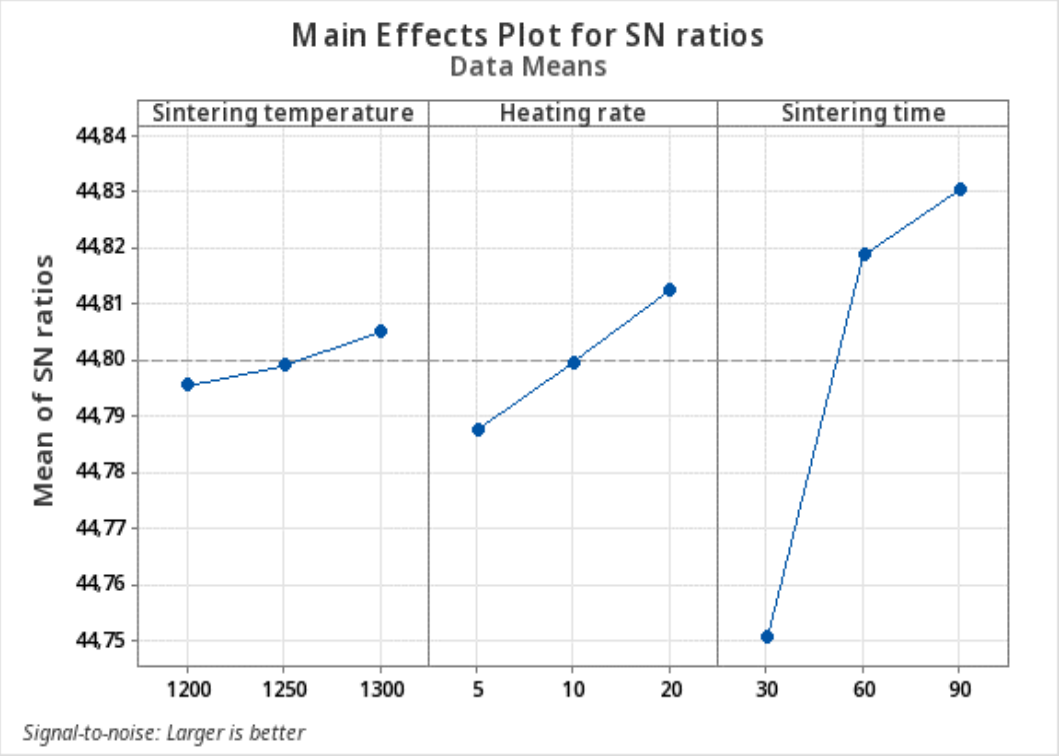

Figure 5.13: The optimal combination based on signal/noise ratio to maximize Young modulus.

Table 5.13, ANOVA table illustrates the effects of each sintering factor to maximize the Young modulus. All three sintering factors significantly affect the specific heat at the 99% significance level. In general, the sintering time has the most significant influence on the elastic modulus, as demonstrated by the much higher F ratio.

Table 5.13: ANOVA for Young modulus.

Source	**DF**	**Adj SS**	**Adj MS**	**F-value**	**P-value**
Sintering Temperature	2	0,0549	0,02745	0,39	0,718
Heating rate	2	0,36938	0,18469	2,65	0,274
Sintering time	2	4,45116	2,22558	31,9	0,03
Error	2	0,13955	0,06978		
Total	8	5,01499			

5.4.3.2/ Effects of sintering conditions on Young modulus

Although in quantitative terms, the values are different, in terms of behavior, it was found that the influence of the sintering conditions on the modulus of elasticity is similar when compared to the specific heat, which allows the same conclusions to be drawn. See Figure 5.14 for more details.

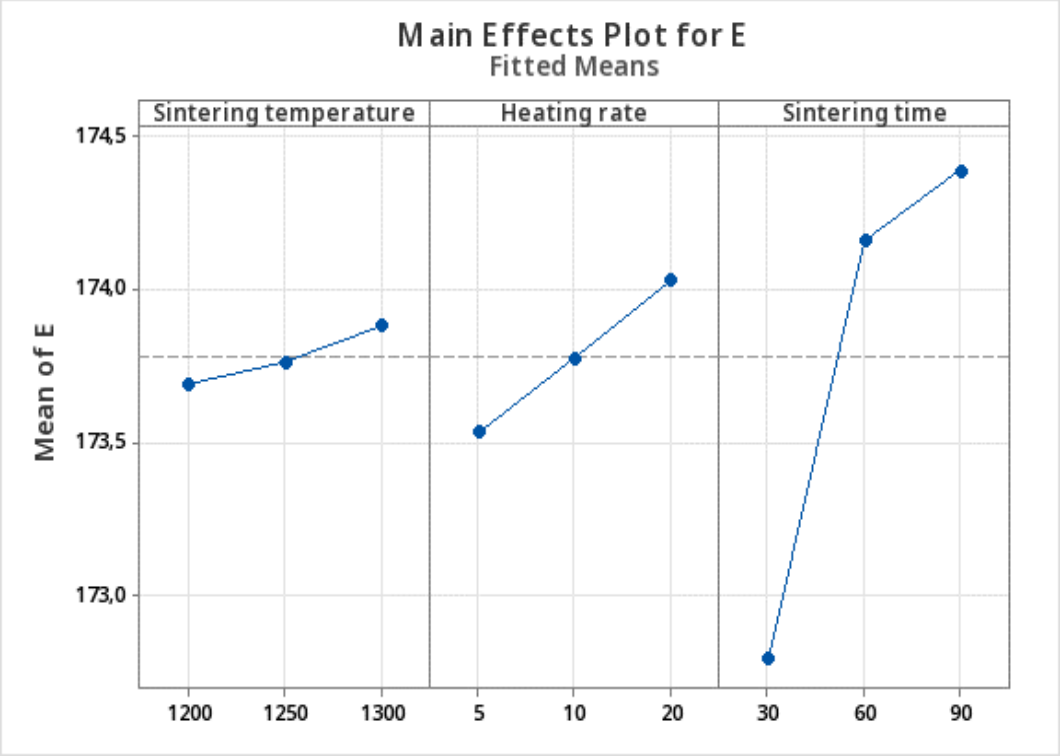

Figure 5.14: The main effects of each parameter on the Young modulus.

5.4.4/ Confirmation test

A confirmation test is an approach that allows you to check whether the prediction of the optimum parameters obtained using the Taguchi technique is similar when tested using an experiment (simulation). Confirmation tests of the control factors were made for the Taguchi method at optimum and random levels. Table 5.14 compares test results and the predicted values obtained using the Taguchi method. To predict and verify the improvement in the final material properties using the optimal level for processing under the sintering conditions. Combinations of processing parameters that optimize the material's properties were obtained using the Taguchi method, and these parameters were then fed into the model as input data, thus allowing the material's properties to be optimized by applying the computer model.

Table 5.14: Confirmation test results by simulations and Taguchi method.

Final properties	**Optim.**	**Levels**	**Simulation**	**Taguchi**	**Error (%)**
Relative density	Maxim.	A2B3C3	0.8421	0.8411	0.12
Thermal conductivity	Minim.	A1B1C1	23.6311	23.6061	0.11
Specific heat	Maxim.	A3B3C3	595.2425	601,088	-0.98
Elastic modulus	Maxim.	A3B3C3	174.5713	174,74	-0.09

The simulation and predicted values have been compared and found to be very close. This indicates that the optimization process has been successful, and the confirmation tests have provided positive results. The high level of correlation between the simulation and predicted values suggests that the model used for optimization is accurate and reliable.

These findings are significant as they provide confidence in the optimization process and demonstrate its effectiveness.

5.5/ Conclusion

In this chapter, we elaborate on the methodology used to apply the model developed in the previous chapter to simulate and predict the material's behavior for MExAM. We discuss the various steps and procedures involved in the process and explain how to use the model to optimize the processed material's thermomechanical properties. Firstly, we delve into the simulation aspect and explain how the model can simulate the material's behavior under different conditions. We discuss the various parameters that need to be considered. Next, we move on to the prediction aspect and how the model can predict the material's behavior under different conditions. We explain how the model can be used to make predictions about the thermomechanical properties of the processed material, such as its density, thermal conductivity, and elastic modulus. Finally, we explain how the model can be used to optimize the thermomechanical properties of the processed material. Optimization was achieved by coupling the simulation results with the Taguchi method. It should be noted that the results obtained from the relative density analysis are in line with the experimental work carried out by [21].

6

Conclusion

Contents

After a critical analysis of the literature review, it can be concluded that the Solid-State Sintering process still requires a comprehensive understanding in terms of computer models. Researchers face the challenge of identifying and mathematically formulating all the physical phenomena that govern the process. The complexity of the process makes it difficult to develop accurate computer models. Furthermore, developing holistic computational models remains challenging, as existing models at different scales require improvement and refinement. The models need adjustment to incorporate experimental observations. This allows researchers to undertake further studies to enhance their understanding of the Solid-State Sintering process and develop precise and efficient numerical models.

In this concluding chapter, I will summarize the significant contributions toward achieving the goal outlined in the introductory chapter. Additionally, I will address the outstanding work required to ensure the widespread utilization of numerical models across various fields, including the industry.

6.1/ Contributions

The pressureless solid-state sintering process is a type of heat treatment commonly used to adjust the properties of materials based on their intended applications. In the introductory chapter, a key research question was presented: Given a green part obtained by MExAM, how can we simulate the microstructure evolution starting from its initial microstructural arrangement, to control the changes in thermomechanical properties that occur during the solid-state sintering process? Several contributions have been made to answer this question. Firstly, a computational simulation model has been developed to accurately predict the green part's microstructure evolution during the solid-state sintering process. Second, the model has been used to identify the key factors influencing the sintered part's microstructure evolution and thermomechanical properties.

Given the context, providing an overview of the contributions is essential. These contributions can be summarized as follows:

- **Mathematical formulation (Chapter 3).** A comprehensive mathematical model has

been presented for investigating pressureless solid-state sintering at the mesoscopic scale. The model employs a multiphysics coupling approach that considers the heat conduction equation, Phase-Field equations, and mechanical equilibrium equation to simulate microstructure evolution during sintering accurately. The model presents several hypotheses for solving the problem, and the study includes detailed explanations of the assumptions made for solving the problem. This chapter describes the mathematical relationships that establish the links among the physical fields involved in the sintering process. The study provides useful insights into the complex physical phenomena occurring during the sintering process and can aid further research. To handle the complexity of the mathematical equations obtained, it was crucial to identify and carefully apply the most appropriate numerical techniques that best suited the problem.

- **Numerical framework (Chapter 4).** A contribution to modeling and simulating pressureless Solid-state Sintering (SSS) using numerical techniques was made. A finite element framework based on Phase-field equations coupled with thermal and mechanical fields has been developed, tested, and validated. The numerical techniques based on the Preconditioned Jacobian Free Newton-Krylov Method used to solve this multi-physics and non-linear problem have been explained. The model was theoretically validated using data from the literature, and the results were consistent with those reported by the authors. Furthermore, the model was simulated to evaluate its behavior, first considering the phase field with Rigid Body Motion incorporation and then considering the influence of thermal and mechanical fields, considering the elastic effect induced by gravity. The numerical techniques used to solve this complex problem have been described in detail, making it a valuable contribution to solid-state sintering. The simulation findings suggest that the developed model can predict the behavior of the sintering process concerning its microstructural, thermal, and mechanical properties. This means that the model can be utilized in MExAM, a similar process, for predicting and analyzing these properties.

- **Applying the numerical model to simulate the MExAM process (Chapter 5).** The presented strategy employs a model to simulate and predict the behavior of materials for MExAM and optimize their thermomechanical properties. Optimization was achieved by combining simulation results with the Taguchi method. The successful application of the model is reflected in the results obtained from the analysis of material properties, which demonstrate the model's ability to predict the microstructural and thermomechanical behavior of the material under specific sintering conditions, as well as its effectiveness in the optimization process.

6.2/ Perspectives and future works

The researchers' primary objective is to make the numerical model at the microscopic level robust and capable of accurately predicting the sintering process's behavior. Based on experimental observations, there is agreement that the sintering phenomenon is governed at the microstructural level. Thus, the maturation and improvement of the numerical model, both adjusted and validated by experimental observations, will continue to be the main lines of research in this area. Figure 6.1 illustrates the main directions guiding future work.

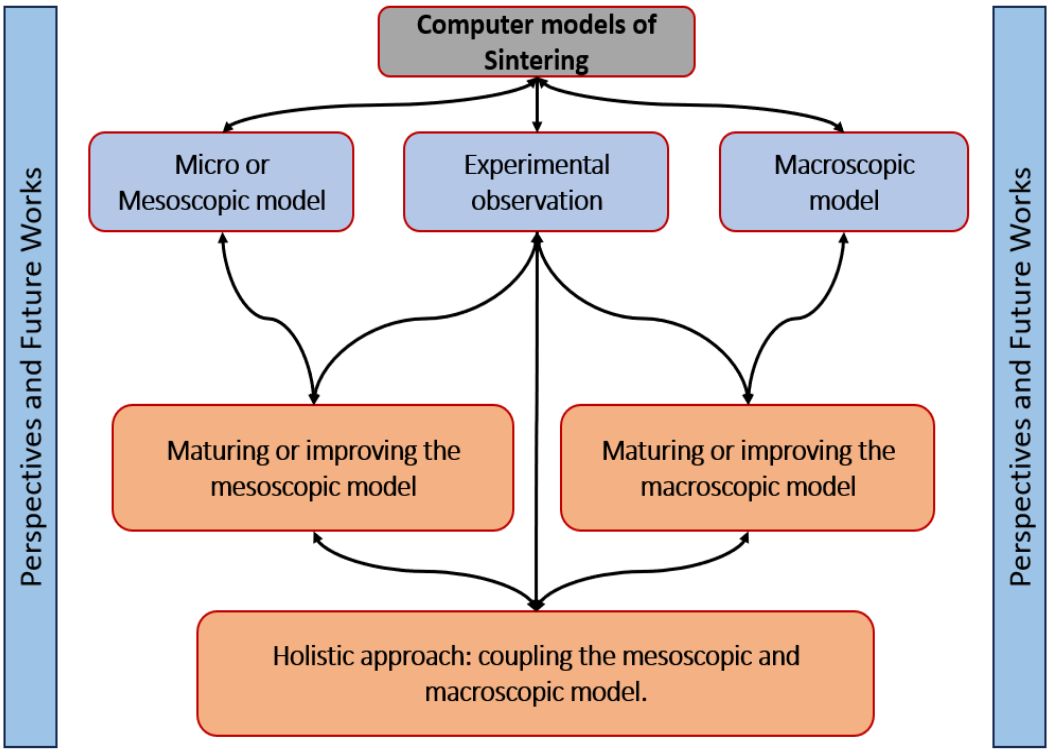

Figure 6.1: Perspectives and future works.

Considering the main challenges for modeling the Solid-state Sintering process and the contributions made in this field through this work, the outlook and future work will follow the following research direction:

- **Maturing and improving the current numerical model**. One of the short-term perspectives is to carry out an exhaustive experimental characterization to obtain data to understand the sintering process thoroughly. So, we will use the DOE approach (Taguchi method) to characterize it experimentally. The characterization will involve a detailed evaluation of how different sintering parameters impact the microstructure evolution. Specifically, we will be examining the changes in porosity, particle size, shape, and arrangement that arise due to variations in sintering parameters. In addition to evaluating the impact of sintering parameters on the microstructure, we will also examine how these parameters affect the thermomechanical behavior of the sintered material. This will involve measuring various properties such as density, thermal conductivity, specific heat, and modulus of elasticity under different sintering conditions. Overall, the experimental characterization process will provide us with a comprehensive understanding of how sintering parameters influence the microstructure and thermomechanical behavior of the material. This knowledge will be invaluable in helping us optimize the sintering process to achieve the desired material properties. All this information (data) will be used to i) Adjust the model to improve its ability to predict microstructure evolution and thermomechanical behavior. ii) Validate the model by comparing experimental and numerical results.

- **Maturing or improving the macroscopic model**. The equations that govern the behavior of sintering at the macroscopic level are obtained by approximation, making the model inaccurate in its prediction. Preparing the macroscopic model to couple

it, for example, with the mesoscopic model or with equations generated by artificial intelligence (physical guide machine learning - PGML), are some of the perspectives for medium-term work.

- **Holistic approach: coupling the mesoscopic and macroscopic model**. There is general agreement among researchers that coupling the mesoscopic model, which represents the microstructural scale, with the macroscopic model, which means the industrial scale, is a promising approach for holistic modeling of the sintering process. So, in the long term, we plan to take the first steps towards preparing the two models, focusing on coupling them. The main challenges are the coupling channel, scales, and numerical aspects.

7

Publications and Scientific Events

7.1/ Peer-reviewed papers

- Cumbunga, J., Abboudi, S., Chamoret, D. (2023). Numerical Modeling and Simulation of Microstructure Evolution during Solid-State Sintering: Multiphysics Approach. In Key Engineering Materials (Vol. 969, pp. 39–47). Trans Tech Publications, Ltd. https://doi.org/10.4028/p-idpi6f

- Cumbunga, J., Abboudi, S., Chamoret, D., Biswas, S., Gomes, S. (2024). Numerical Modeling of the Solid-State Sintering Process by Coupling the Thermal and Microstructural Fields. In: Ali-Toudert, F., Draoui, A., Halouani, K., Hasnaoui, M., Jemni, A., Tadrist, L. (eds) Advances in Thermal Science and Energy. JITH 2022. Lecture Notes in Mechanical Engineering. Springer, Cham. https://doi.org/10.1007/978-3-031-43934-6-5

- Judice Cumbunga, Said Abboudi, Dominique Chamoret, Samuel Gomes. Numerical modeling of the solid-state sintering at the microstructural level: Multiphysics approach and application to metal additive manufacturing. Colloque InterUT Systèmes sûrs et durables, Université de Technologie de Compiègne [UTC], Feb 2023, Paris, France. https://doi.org/ffhal-04011815f

7.2/ Conference attendance

- International Days on Thermal Science and Energy, JITH 2022, November 15-17, 2022, Tangier, Morocco. **Communication title:** Numerical Modeling of the Solid-State Sintering Process by Coupling the Thermal and Microstructural Fields.

- 8th International Conference on Civil Engineering and Materials Science (ICCEMS 2023), Singapore, June 14 – 16, 2023. **Communication title:** Numerical Modeling and Simulation of Microstructure Evolution during Solid-State Sintering: Multiphysics Approach (Best presentation).

- Colloque InterUT Systèmes sures et durables, Université de Technologie de Compiègne [UTC], Feb 2023, Paris, France. **Communication title:** Numerical modeling of the solid-state sintering at the microstructural level: Multiphysics approach and application to metal additive manufacturing.

- International Conference on Sintering, 27 - 31 Aug 2023, Nagaragawa Convention Center, Gifu, Japan. **Communication title:** Microstructural Evolution In Solid-State Sintering Processes: Multiphysics Approach And Numerical Modeling.

Bibliography

[1] Haidar Ramazani and Abdolvahed Kami. Metal FDM, a new extrusion-based additive manufacturing technology for manufacturing of metallic parts: a review. *Prog Addit Manuf*, 7(4):609–626, August 2022.

[2] Aghnia Ilmiah Nurhudan, Sugeng Supriadi, Yudan Whulanza, and Agung Shamsuddin Saragih. Additive manufacturing of metallic based on extrusion process: A review. *Journal of Manufacturing Processes*, 66:228–237, June 2021.

[3] W. Niu and J. Pan. 4 - Computer modelling of sintering: theory and examples. In Zhigang Zak Fang, editor, *Sintering of Advanced Materials*, Woodhead Publishing Series in Metals and Surface Engineering, pages 86–109. Woodhead Publishing, January 2010.

[4] Friedrich Raether, Gerhard Seifert, and Heiko Ziebold. Simulation of Sintering across Scales. *Advanced Theory and Simulations*, 2(7):1900048, 2019. _eprint: https://onlinelibrary.wiley.com/doi/pdf/10.1002/adts.201900048.

[5] Lifeng Ding, Ruslan L. Davidchack, and Jingzhe Pan. A molecular dynamics study of sintering between nanoparticles. *Computational Materials Science*, 45(2):247–256, April 2009.

[6] Jingzhe Pan. Modelling sintering at different length scales. *International Materials Reviews*, 48(2):69–85, April 2003. Publisher: Taylor & Francis _eprint: https://doi.org/10.1179/095066002225010209.

[7] P. Bross and H. E. Exner. Computer simulation of sintering processes. *Acta Metallurgica*, 27(6):1013–1020, June 1979.

[8] Yu U. Wang. Computer modeling and simulation of solid-state sintering: A phase field approach. *Acta Materialia*, 54(4):953–961, February 2006.

[9] Nele Moelans, Bart Blanpain, and Patrick Wollants. An introduction to phase-field modeling of microstructure evolution. *Calphad*, 32(2):268–294, June 2008.

[10] Randall M. German. Chapter Fourteen - Computer Models. In Randall M. German, editor, *Sintering: from Empirical Observations to Scientific Principles*, pages 433–469. Butterworth-Heinemann, Boston, January 2014.

[11] R. German. Computer modeling of sintering processes. *International Journal of Powder Metallurgy*, 2002.

[12] Randall M. German. Chapter Two - History of Sintering. In Randall M. German, editor, *Sintering: from Empirical Observations to Scientific Principles*, pages 13–40. Butterworth-Heinemann, Boston, January 2014.

[13] Randall M. German. Chapter One - Introduction. In Randall M. German, editor, *Sintering: from Empirical Observations to Scientific Principles*, pages 1–12. Butterworth-Heinemann, Boston, January 2014.

[14] H.E Exner. Solid-State Sintering: Critical Assessment of Theoretical Concepts and Experimental Methods. In Shigeyuki Sōmiya and Yusuke Moriyoshi, editors, *Sintering Key Papers*, pages 87–100. Springer Netherlands, Dordrecht, 1990.

[15] Eryk Ryzko. Sintering Densification Grain Growth and Microstructure S Kang.

[16] F. Thümmler and W. Thomma. The sintering process. *Metallurgical Reviews*, 12(1):69–108, January 1967. Publisher: Taylor & Francis _eprint: https://doi.org/10.1179/mtlr.1967.12.1.69.

[17] H. E. Exner and E. Arzt. CHAPTER 31 - SINTERING PROCESSES. In Robert W. Cahn and Peter Haasen†, editors, *Physical Metallurgy (Fourth Edition)*, pages 2627–2662. North-Holland, Oxford, January 1996.

[18] R. J. Brook. Sintering: An Overview. In RJ Brook, editor, *Concise Encyclopedia of Advanced Ceramic Materials*, pages 438–440. Pergamon, Oxford, January 1991.

[19] Randall M. German. Chapter Nine - Sintering With a Liquid Phase. In Randall M. German, editor, *Sintering: from Empirical Observations to Scientific Principles*, pages 247–303. Butterworth-Heinemann, Boston, January 2014.

[20] John E. Blendell and Wolfgang Rheinheimer. Solid-State Sintering. In Michael Pomeroy, editor, *Encyclopedia of Materials: Technical Ceramics and Glasses*, pages 249–257. Elsevier, Oxford, January 2021.

[21] C. H. Ji, N. H. Loh, K. A. Khor, and S. B. Tor. Sintering study of 316L stainless steel metal injection molding parts using Taguchi method: final density. *Materials Science and Engineering: A*, 311(1):74–82, July 2001.

[22] JR Merhar. Overview of metal injection moulding. *Metal Powder Report*, 45(5):339–342, May 1990.

[23] Donald F. Heaney. *Handbook of Metal Injection Molding*. Woodhead Publishing, November 2018. Google-Books-ID: dA6ZDwAAQBAJ.

[24] Hideshi Miura, Toshiko Osada, and Yoshinori Itoh. Metal Injection Molding (MIM) Processing. In Mitsuo Niinomi, Takayuki Narushima, and Masaaki Nakai, editors, *Advances in Metallic Biomaterials: Processing and Applications*, Springer Series in Biomaterials Science and Engineering, pages 27–56. Springer, Berlin, Heidelberg, 2015.

[25] T. Ebel. 19 - Metal injection molding (MIM) of titanium and titanium alloys. In Donald F. Heaney, editor, *Handbook of Metal Injection Molding (Second Edition)*, Woodhead Publishing Series in Metals and Surface Engineering, pages 431–460. Woodhead Publishing, January 2019.

[26] Nihan Tuncer and Animesh Bose. Solid-State Metal Additive Manufacturing: A Review. *JOM*, 72(9):3090–3111, September 2020.

[**27**] Chanun Suwanpreecha and Anchalee Manonukul. A Review on Material Extrusion Additive Manufacturing of Metal and How It Compares with Metal Injection Moulding. *Metals*, 12(3):429, March 2022. Number: 3 Publisher: Multidisciplinary Digital Publishing Institute.

[**28**] Alberto Molinari. Fundamentals of Sintering: Solid State Sintering. In Francisca G. Caballero, editor, *Encyclopedia of Materials: Metals and Allloys*, pages 471–480. Elsevier, Oxford, January 2022.

[**29**] Narottam P. Bansal and Aldo R. Boccaccini. *Ceramics and Composites Processing Methods*. John Wiley & Sons, April 2012.

[**30**] R. T. Dehoff. 3 - Path and kinetics of microstructural change in simple sintering. In Zhigang Zak Fang, editor, *Sintering of Advanced Materials*, Woodhead Publishing Series in Metals and Surface Engineering, pages 65–85. Woodhead Publishing, January 2010.

[**31**] D. Pino-Muñoz, J. Bruchon, S. Drapier, and F. Valdivieso. Sintering at Particle Scale: An Eulerian Computing Framework to Deal with Strong Topological and Material Discontinuities. *Arch Computat Methods Eng*, 21(2):141–187, June 2014.

[**32**] J. L. Shi. Solid state sintering of ceramics: pore microstructure models, densification equations and applications. *Journal of Materials Science*, 34(15):3801–3812, August 1999.

[**33**] Randall German. Sintering: From Empirical Observations to Scientific Principles. *Sintering: From Empirical Observations to Scientific Principles*, pages 1–536, 2014.

[**34**] Randall M. German. Chapter Six - Geometric Trajectories during Sintering. In Randall M. German, editor, *Sintering: from Empirical Observations to Scientific Principles*, pages 141–181. Butterworth-Heinemann, Boston, January 2014.

[**35**] Johannes Hötzer, Marco Seiz, Michael Kellner, Wolfgang Rheinheimer, and Britta Nestler. Phase-field simulation of solid state sintering. *Acta Materialia*, 164:184–195, February 2019.

[**36**] R. M. German. 1 - Thermodynamics of sintering. In Zhigang Zak Fang, editor, *Sintering of Advanced Materials*, Woodhead Publishing Series in Metals and Surface Engineering, pages 3–32. Woodhead Publishing, January 2010.

[**37**] Rajendra Bordia, Suk-Joong Kang, and Eugene Olevsky. Current understanding and future research directions at the onset of the next century of sintering science and technology. *Journal of the American Ceramic Society*, 100, April 2017.

[**38**] Shaun Cooke, Keivan Ahmadi, Stephanie Willerth, and Rodney Herring. Metal additive manufacturing: Technology, metallurgy and modelling. *Journal of Manufacturing Processes*, 57:978–1003, September 2020.

[**39**] William E. Frazier. Metal Additive Manufacturing: A Review. *J. of Materi Eng and Perform*, 23(6):1917–1928, June 2014.

[**40**] Mark Armstrong, Hamid Mehrabi, and Nida Naveed. An overview of modern metal additive manufacturing technology. *Journal of Manufacturing Processes*, 84:1001–1029, December 2022.

[41] Joamin Gonzalez-Gutierrez, Santiago Cano, Stephan Schuschnigg, Christian Kukla, Janak Sapkota, and Clemens Holzer. Additive Manufacturing of Metallic and Ceramic Components by the Material Extrusion of Highly-Filled Polymers: A Review and Future Perspectives. *Materials*, 11(5):840, May 2018. Number: 5 Publisher: Multidisciplinary Digital Publishing Institute.

[42] Yvonne Thompson, Joamin Gonzalez-Gutierrez, Christian Kukla, and Peter Felfer. Fused filament fabrication, debinding and sintering as a low cost additive manufacturing method of 316L stainless steel. *Additive Manufacturing*, 30:100861, December 2019.

[43] Randall M. German. Chapter Sixteen - Future Prospects for Sintering. In Randall M. German, editor, *Sintering: from Empirical Observations to Scientific Principles*, pages 513–526. Butterworth-Heinemann, Boston, January 2014.

[44] Jesse M. Sestito, Fadi Abdeljawad, Tequila A. L. Harris, Yan Wang, and Allen Roach. An atomistic simulation study of nanoscale sintering: The role of grain boundary misorientation. *Computational Materials Science*, 165:180–189, July 2019.

[45] Hideaki Matsubara and Richard J. Brook. Computational Modeling of Sintering Process in Ceramics. *Key Engineering Materials*, 132-136:710–713, 1997. Conference Name: Euro Ceramics V ISBN: 9780878497614 Publisher: Trans Tech Publications Ltd.

[46] H. N. Ch'ng and J. Pan. Modelling microstructural evolution of porous polycrystalline materials and a numerical study of anisotropic sintering. *J. Comput. Phys.*, 204(2):430–461, April 2005.

[47] Michael Gasik and Baosheng Zhang. A constitutive model and FE simulation for the sintering process of powder compacts. *Computational Materials Science*, 18(1):93–101, July 2000.

[48] Torsten Kraft and Hermann Riedel. Numerical simulation of solid state sintering; model and application. *Journal of the European Ceramic Society*, 24(2):345–361, January 2004.

[49] J. Song, J. C. Gelin, T. Barrière, and B. Liu. Experiments and numerical modelling of solid state sintering for 316L stainless steel components. *Journal of Materials Processing Technology*, 177(1):352–355, July 2006.

[50] Krzysztof Wawrzyk, Piotr Kowalczyk, Szymon Nosewicz, and Jerzy Rojek. A constitutive model and numerical simulation of sintering processes at macroscopic level. *AIP Conference Proceedings*, 1922(1):030011, January 2018. Publisher: American Institute of Physics.

[51] Tesfaye Tadesse Molla, Rasmus Bjørk, Eugene Olevsky, Nini Pryds, and Henrik Lund Frandsen. Multi-scale modeling of shape distortions during sintering of bi-layers. *Computational Materials Science*, 88:28–36, June 2014.

[52] Jerzy Rojek, Szymon Nosewicz, and Marcin Chmielewski. MICRO-MACRO RELATIONSHIPS FROM DISCRETE ELEMENT SIMULATIONS OF SINTERING. *JMC*, 15(4), 2017. Publisher: Begel House Inc.

[**53**] Lvyan Yang, Xianglai Gan, Chao Xu, Lin Lang, Zhiyong Jian, Shifang Xiao, Huiqiu Deng, Xiaofan Li, Zean Tian, and Wangyu Hu. Molecular dynamics simulation of alloying during sintering of Li and Pb metallic nanoparticles. *Computational Materials Science*, 156:47–55, January 2019.

[**54**] Yi Zhang, Linmin Wu, Hazim El-Mounayri, Kim Brand, and Jing Zhang. Molecular Dynamics Study of the Strength of Laser Sintered Iron Nanoparticles. *Procedia Manufacturing*, 1:296–307, January 2015.

[**55**] Michael Braginsky, Veena Tikare, and Eugene Olevsky. Numerical simulation of solid state sintering. *International Journal of Solids and Structures*, 42(2):621–636, January 2005.

[**56**] Veena Tikare, Michael Braginsky, Didier Bouvard, and Alexander Vagnon. Numerical simulation of microstructural evolution during sintering at the mesoscale in a 3D powder compact. *Computational Materials Science*, 48(2):317–325, April 2010.

[**57**] Yi Zhang, Xianghui Xiao, and Jing Zhang. Kinetic Monte Carlo simulation of sintering behavior of additively manufactured stainless steel powder particles using reconstructed microstructures from synchrotron X-ray microtomography. *Results in Physics*, 13:102336, June 2019.

[**58**] Sudipta Biswas, Daniel Schwen, and Vikas Tomar. Implementation of a phase field model for simulating evolution of two powder particles representing microstructural changes during sintering. *J Mater Sci*, 53(8):5799–5825, April 2018.

[**59**] S. Martin, M. Guessasma, J. Léchelle, J. Fortin, K. Saleh, and F. Adenot. Simulation of sintering using a Non Smooth Discrete Element Method. Application to the study of rearrangement. *Computational Materials Science*, 84:31–39, March 2014.

[**60**] B. Henrich, A. Wonisch, T. Kraft, M. Moseler, and H. Riedel. Simulations of the influence of rearrangement during sintering. *Acta Materialia*, 55(2):753–762, January 2007.

[**61**] Tobias Rasp, Christine Jamin, Andreas Wonisch, Torsten Kraft, and Olivier Guillon. Shape Distortion and Delamination During Constrained Sintering of Ceramic Stripes: Discrete Element Simulations and Experiments. *Journal of the American Ceramic Society*, 95(2):586–592, 2012. _eprint: https://onlinelibrary.wiley.com/doi/pdf/10.1111/j.1551-2916.2011.04939.x.

[**62**] Christophe L. Martin, Héctor Camacho-Montes, Luis Olmos, Didier Bouvard, and Rajendra K. Bordia. Evolution of Defects During Sintering: Discrete Element Simulations. *Journal of the American Ceramic Society*, 92(7):1435–1441, 2009. _eprint: https://onlinelibrary.wiley.com/doi/pdf/10.1111/j.1551-2916.2009.03014.x.

[**63**] C. L. Martin and R. K. Bordia. The effect of a substrate on the sintering of constrained films. *Acta Materialia*, 57(2):549–558, January 2009.

[**64**] Kazunari Shinagawa. Simulation of grain growth and sintering process by combined phase-field/discrete-element method. *Acta Materialia*, 66:360–369, March 2014.

[**65**] D. Fan and L. Q. Chen. Computer simulation of grain growth using a continuum field model. *Acta Materialia*, 45(2):611–622, February 1997.

[66] Long-Qing Chen. Phase-Field Models for Microstructure Evolution. *Annual Review of Materials Research*, 32(1):113–140, 2002. _eprint: https://doi.org/10.1146/annurev.matsci.32.112001.132041.

[67] X. H. Guo, San-Qiang Shi, and X. Q. Ma. Elastoplastic phase field model for microstructure evolution. *Appl. Phys. Lett.*, 87(22):221910, November 2005. Publisher: American Institute of Physics.

[68] C. E. Krill III and L. Q. Chen. Computer simulation of 3-D grain growth using a phase-field model. *Acta Materialia*, 50(12):3059–3075, July 2002.

[69] Rongpei Shi, Marissa Wood, Tae Wook Heo, Brandon C. Wood, and Jianchao Ye. Towards understanding particle rigid-body motion during solid-state sintering. *Journal of the European Ceramic Society*, September 2021.

[70] Sudipta Biswas, Daniel Schwen, Jogender Singh, and Vikas Tomar. A study of the evolution of microstructure and consolidation kinetics during sintering using a phase field modeling based approach. *Extreme Mechanics Letters*, 7:78–89, June 2016.

[71] Vladimir Ivannikov, Fritz Thomsen, Thomas Ebel, and Regine Willumeit-Römer. Capturing shrinkage and neck growth with phase field simulations of the solid state sintering. *Modelling Simul. Mater. Sci. Eng.*, 29(7):075008, September 2021. Publisher: IOP Publishing.

[72] Robert Termuhlen, Xanthippi Chatzistavrou, Jason D. Nicholas, and Hui-Chia Yu. Three-dimensional phase field sintering simulations accounting for the rigid-body motion of individual grains. *Computational Materials Science*, 186:109963, January 2021.

[73] K. Chockalingam, V. G. Kouznetsova, O. van der Sluis, and M. G. D. Geers. 2D Phase field modeling of sintering of silver nanoparticles. *Computer Methods in Applied Mechanics and Engineering*, 312:492–508, December 2016.

[74] Belgacem Mamen, Jiupeng Song, Thierry Barriere, and Jean-Claude Gelin. Experimental and numerical analysis of the particle size effect on the densification behaviour of metal injection moulded tungsten parts during sintering. *Powder Technology*, 270:230–243, January 2015.

[75] M. Sahli, H. Djoudi, J.-C. Gelin, T. Barriere, and M. Assoul. Numerical simulation and experimental analysis of the sintered micro-parts using the powder injection molding process. *Microsyst Technol*, 24(3):1495–1508, March 2018.

[76] Eugene A. Olevsky, Veena Tikare, and Terry Garino. Multi-Scale Study of Sintering: A Review. *Journal of the American Ceramic Society*, 89(6):1914–1922, 2006. _eprint: https://ceramics.onlinelibrary.wiley.com/doi/pdf/10.1111/j.1551-2916.2006.01054.x.

[77] Caner Şimşir and Cemil Hakan Gür. A FEM based framework for simulation of thermal treatments: Application to steel quenching. *Computational Materials Science*, 44(2):588–600, December 2008.

[78] H. S. Carslaw, J. C. Jaeger, and Herman Feshbach. Conduction of Heat in Solids. *Physics Today*, 15(11):74–76, November 1962. Publisher: American Institute of Physics.

[**79**] P. S. Liu and G. F. Chen. Chapter Two - Making Porous Metals. In P. S. Liu and G. F. Chen, editors, *Porous Materials*, pages 21–112. Butterworth-Heinemann, Boston, January 2014.

[**80**] K. Ahmed, C. A. Yablinsky, A. Schulte, T. Allen, and A. El-Azab. Phase field modeling of the effect of porosity on grain growth kinetics in polycrystalline ceramics. *Modelling Simul. Mater. Sci. Eng.*, 21(6):065005, July 2013. Publisher: IOP Publishing.

[**81**] Armen G. Khachaturyan. *Theory of Structural Transformations in Solids*. Courier Corporation, December 2013. Google-Books-ID: xyQkAwAAQBAJ.

[**82**] S. Y. Hu and L. Q. Chen. A phase-field model for evolving microstructures with strong elastic inhomogeneity. *Acta Materialia*, 49(11):1879–1890, June 2001.

[**83**] Michael Tonks, Paul Millett, Wei Cai, and Dieter Wolf. Analysis of the elastic strain energy driving force for grain boundary migration using phase field simulation. *Scripta Materialia*, 63(11):1049–1052, November 2010.

[**84**] Ingo Steinbach. Phase-field models in materials science. *Modelling Simul. Mater. Sci. Eng.*, 17(7):073001, July 2009. Publisher: IOP Publishing.

[**85**] Allan F. Bower. *Applied Mechanics of Solids*. CRC Press, Boca Raton, October 2009.

[**86**] Jaemin Shin, Darae Jeong, and Junseok Kim. A conservative numerical method for the Cahn–Hilliard equation in complex domains. *Journal of Computational Physics*, 230(19):7441–7455, August 2011.

[**87**] Liangzhe Zhang, Michael R. Tonks, Paul C. Millett, Yongfeng Zhang, Karthikeyan Chockalingam, and Bulent Biner. Phase-field modeling of temperature gradient driven pore migration coupling with thermal conduction. *Computational Materials Science*, 56:161–165, April 2012.

[**88**] D. Schwen, L. K. Aagesen, J. W. Peterson, and M. R. Tonks. Rapid multiphase-field model development using a modular free energy based approach with automatic differentiation in MOOSE/MARMOT. *Computational Materials Science*, 132:36–45, May 2017.

[**89**] Dongsun Lee, Joo-Youl Huh, Darae Jeong, Jaemin Shin, Ana Yun, and Junseok Kim. Physical, mathematical, and numerical derivations of the Cahn–Hilliard equation. *Computational Materials Science*, 81:216–225, January 2014.

[**90**] HyeongKae Park, Robert R. Nourgaliev, Richard C. Martineau, and Dana A. Knoll. On physics-based preconditioning of the Navier–Stokes equations. *Journal of Computational Physics*, 228(24):9131–9146, December 2009.

[**91**] G. E. Hammond, A. J. Valocchi, and P. C. Lichtner. Application of Jacobian-free Newton–Krylov with physics-based preconditioning to biogeochemical transport. *Advances in Water Resources*, 28(4):359–376, April 2005.

[**92**] D. A. Knoll and D. E. Keyes. Jacobian-free Newton–Krylov methods: a survey of approaches and applications. *Journal of Computational Physics*, 193(2):357–397, January 2004.

[93] D. Gaston, G. Hansen, S. Kadioglu, D. A. Knoll, C. Newman, H. Park, C. Permann, and W. Taitano. Parallel multiphysics algorithms and software for computational nuclear engineering. *J. Phys.: Conf. Ser.*, 180(1):012012, July 2009.

[94] Niteen Kumar and Suneet Singh. A novel physics-based preconditioner for nodal integral method using JFNK for 2D Burgers equation. *Progress in Nuclear Energy*, 134:103668, April 2021.

[95] H. Park, D. A. Knoll, D. R. Gaston, and R. C. Martineau. Tightly Coupled Multiphysics Algorithms for Pebble Bed Reactors. *Nuclear Science and Engineering*, 166(2):118–133, October 2010. Publisher: Taylor & Francis _eprint: https://doi.org/10.13182/NSE09-104.

[96] Michele Benzi. Preconditioning Techniques for Large Linear Systems: A Survey. *Journal of Computational Physics*, 182(2):418–477, November 2002.

[97] V. Dolean, M. J. Gander, W. Kheriji, F. Kwok, and R. Masson. Nonlinear Preconditioning: How to Use a Nonlinear Schwarz Method to Precondition Newton's Method. *SIAM J. Sci. Comput.*, 38(6):A3357–A3380, January 2016. Publisher: Society for Industrial and Applied Mathematics.

[98] Alfredo Duarte Gomez, Nicholas Deak, and Fabrizio Bisetti. Jacobian-free Newton–Krylov method for the simulation of non-thermal plasma discharges with high-order time integration and physics-based preconditioning. *Journal of Computational Physics*, 480:112007, May 2023.

[99] Cody J. Permann, Derek R. Gaston, David Andrš, Robert W. Carlsen, Fande Kong, Alexander D. Lindsay, Jason M. Miller, John W. Peterson, Andrew E. Slaughter, Roy H. Stogner, and Richard C. Martineau. MOOSE: Enabling massively parallel multiphysics simulation. *SoftwareX*, 11:100430, January 2020.

[100] Michael R. Tonks, Derek Gaston, Paul C. Millett, David Andrs, and Paul Talbot. An object-oriented finite element framework for multiphysics phase field simulations. *Computational Materials Science*, 51(1):20–29, January 2012.

[101] Derek Gaston, Chris Newman, Glen Hansen, and Damien Lebrun-Grandié. MOOSE: A parallel computational framework for coupled systems of nonlinear equations. *Nuclear Engineering and Design*, 239(10):1768–1778, October 2009.

[102] C. S. Kim. Thermophysical properties of stainless steels. Technical Report ANL-75-55, Argonne National Lab., Ill. (USA), September 1975.

[103] J. L. Straalsund and J. F. Bates. Partial molar volumes and size factor data for alloy constituents of stainless steel. *Metall Mater Trans B*, 5(2):493–498, February 1974.

[104] Xing Zhang and Yiliang Liao. A phase-field model for solid-state selective laser sintering of metallic materials. *Powder Technology*, 339:677–685, November 2018.

[105] John R. Wagner, Eldridge M. Mount, and Harold F. Giles. 25 - Design of Experiments. In John R. Wagner, Eldridge M. Mount, and Harold F. Giles, editors, *Extrusion (Second Edition)*, Plastics Design Library, pages 291–308. William Andrew Publishing, Oxford, January 2014.

[**106**] C. Yuangyai and H. B. Nembhard. Chapter 8 - Design of Experiments: A Key to Innovation in Nanotechnology. In Waqar Ahmed and Mark J. Jackson, editors, *Emerging Nanotechnologies for Manufacturing*, Micro and Nano Technologies, pages 207–234. William Andrew Publishing, Boston, January 2010.

[**107**] Anup K. Das and Saikat Dewanjee. Chapter 3 - Optimization of Extraction Using Mathematical Models and Computation. In Satyajit D. Sarker and Lutfun Nahar, editors, *Computational Phytochemistry*, pages 75–106. Elsevier, January 2018.

[**108**] Yuanjiang Pei, Anqi Zhang, Pinaki Pal, Le Zhao, Yu Zhang, and Sibendu Som. Chapter 5 - Computational fluid dynamics–guided engine combustion system design optimization using design of experiments. In Jihad Badra, Pinaki Pal, Yuanjiang Pei, and Sibendu Som, editors, *Artificial Intelligence and Data Driven Optimization of Internal Combustion Engines*, pages 103–123. Elsevier, January 2022.

[**109**] S. Dingal, T. R. Pradhan, J. K. Sarin Sundar, A. Roy Choudhury, and S. K. Roy. The application of Taguchi's method in the experimental investigation of the laser sintering process. *Int J Adv Manuf Technol*, 38(9):904–914, September 2008.

[**110**] Yujia Wang and Yaoyao Fiona Zhao. Investigation of Sintering Shrinkage in Binder Jetting Additive Manufacturing Process. *Procedia Manufacturing*, 10:779–790, January 2017.

[**111**] Yiwei Mao, Chao Cai, Jinkai Zhang, Yuhua Heng, Kunhao Feng, Daosheng Cai, and Qingsong Wei. Effect of sintering temperature on binder jetting additively manufactured stainless steel 316L: densification, microstructure evolution and mechanical properties. *Journal of Materials Research and Technology*, 22:2720–2735, January 2023.

[**112**] Muhammad Rafi Raza Malik, Faiz Ahmad, Othman Mamat, Mohd Afian Omar, R. M. German, and Ali S. Muhsan. Effects of Sintering Temperature and Cooling Rate on Mechanical Properties of Powder Injection Molded 316L Stainless Steel. *Solid State Phenomena*, 185:102–105, 2012. Publisher: Trans Tech Publications Ltd.

[**113**] Marius A. Wagner, Jona Engel, Amir Hadian, Frank Clemens, Mikel Rodriguez-Arbaizar, Efrain Carreño-Morelli, Jeffrey M. Wheeler, and Ralph Spolenak. Filament extrusion-based additive manufacturing of 316L stainless steel: Effects of sintering conditions on the microstructure and mechanical properties. *Additive Manufacturing*, 59:103147, November 2022.

[**114**] D. Ratna. 3 - Thermal properties of thermosets. In Qipeng Guo, editor, *Thermosets*, pages 62–91. Woodhead Publishing, January 2012.

[**115**] Muhammad Awais, Arafat A. Bhuiyan, Sayedus Salehin, Mohammad Monjurul Ehsan, Basit Khan, and Md. Hamidur Rahman. Synthesis, heat transport mechanisms and thermophysical properties of nanofluids: A critical overview. *International Journal of Thermofluids*, 10:100086, May 2021.

[**116**] Haoshan Ren, Zhenjun Ma, Jingjing Liu, Xuemei Gong, and Weihua Li. A review of heat and mass transfer improvement techniques for dehumidifiers and regenerators of liquid desiccant cooling systems. *Applied Thermal Engineering*, 162:114271, November 2019.

Document generated with LaTeX and:
the LaTeX style for PhD Thesis created by S. Galland — http://www.multiagent.fr/ThesisStyle
the tex-upmethodology package suite — http://www.arakhne.org/tex-upmethodology/